Technische Universität München

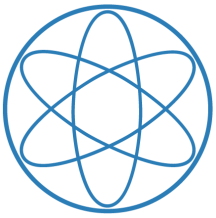

Physik-Department
Lehrstuhl für Experimentelle Astroteilchenphysik

Development of an Organic Plastic Scintillator based Muon Veto Operating at Sub-Kelvin Temperatures for the NUCLEUS Experiment

Abschlussarbeit im Masterstudiengang
Kern-, Teilchen- und Astrophysik

Andreas Erhart

April 2021

Technische Universität München
Physik-Department
Lehrstuhl für experimentelle Astroteilchenphysik

Université Paris Saclay
Centre CEA de Saclay
Institut de recherche sur les lois fondamentales de l'Univers

---

Development of an Organic Plastic Scintillator based Muon Veto Operating at Sub-Kelvin Temperatures for the NUCLEUS Experiment

Andreas Erhart

April 2021

Erstgutachter: Dr. rer. nat. Raimund Strauß

Zweitgutachterin: Prof. Dr. rer. nat. Laura Fabbietti

Supervisors: Dr. rer. nat. Victoria Wagner & Dr. rer. nat. David Lhuillier

Eingereicht von: B.Sc. Andreas Erhart
andreas.erhart@tum.de

Eingereicht am: 16. April 2021

Abstract

The exploration of coherent elastic neutrino-nucleus scattering (CEνNS) opens a new window to study the fundamental properties of neutrinos and to probe physics within and beyond the Standard Model of Particle Physics. The NUCLEUS experiment aims to employ gram-scale ultra-low threshold cryogenic detectors to measure antineutrinos scattering coherently off the target nuclei. The new experimental site designated for the installation of the NUCLEUS experiment is located in between the two $4.25\,GW_{th}$ reactor cores of the Chooz nuclear power plant and features an expected antineutrino flux as high as $10^{12}\,\bar{\nu}_e/(\mathrm{s{\cdot}cm^2})$. An accurate measurement of the CEνNS cross-section requires a low residual background rate in the target detectors. Operating at an overburden of only $\sim 3\,$m.w.e., muon-induced events are expected to be the dominant source of background. For this reason, a highly efficient muon veto with a muon detection efficiency of more than $99\,\%$ is indispensable and shall be achieved in NUCLEUS with a compact cube assembly of plastic scintillator panels. In order to prevent a large unshielded area where the cryostat enters the shielding arrangement without unnecessarily increasing the induced detector dead time, a novel and innovative concept has been investigated. It consists of a plastic scintillator based disc-shape active muon veto operating inside the NUCLEUS cryostat at sub-Kelvin temperatures. The development of this so called NUCLEUS *Cryogenic Muon Veto* is the main subject of the presented thesis.

The important role of the *Cryogenic Muon Veto* for the overall muon veto performance was clearly confirmed by an efficiency study conducted within the context of this work. The study was based on a Monte Carlo simulation framework developed collaboratively in the context of the overall NUCLEUS muon veto. The *Cryogenic Muon Veto* turned out to be a key component towards achieving the targeted muon detection efficiency of $>99\,\%$ and was found to suppress the number of non-vetoed muons stopping inside the experimental arrangement by a factor of ~ 2.1. The required verification of the key physical aspects of the intended *Cryogenic Muon Veto* detector concept, provided by investigating its low temperature behavior, led to the first reported measurements of organic plastic scintillators at sub-Kelvin temperatures. The functionality of the principal scintillation process of organic plastic scintillators at sub-Kelvin temperatures has been confirmed and the feasibility of cooling a polystyrene based plastic scintillator to sub-Kelvin temperatures on a time scale of $\sim 52\,$h - and thus compatible with the parameters of the NUCLEUS cryogenic infrastructure - has been demonstrated. For these measurements, a setup to study the phenomenology of organic plastic scintillators at sub-Kelvin temperatures has been established, which can be used in the future for an accurate characterization of the temperature dependence of the plastics' scintillation light yield in a range from $50\,$K to $0.8\,$K. First observations of an enhancement of the light signal of a plastic scintillator detector by $\sim 46\%$ at sub-Kelvin temperature compared to that at room temperature hint towards an indirect proportional temperature dependence of the scintillation light yield. On the basis of these findings, a disc-shape plastic scintillator based muon veto equipped with wavelength shifting fibers and a silicon photomultiplier to guide and detect the scintillation light has been designed and assembled. Initial commissioning of the plastic scintillator disc at room temperature confirmed the overall detector concept and allowed unambiguous identification of muon events, which are clearly distinct from low-energy background events. With the presented thesis, the groundwork for the *Cryogenic Muon Veto* has been laid. The NUCLEUS *Cryogenic Muon Veto* will be the first of its kind to be operated inside a cryostat at sub-Kelvin temperatures.

Contents

List of Figures

List of Tables

1. Search for Coherent Elastic Scattering of Reactor-Antineutrinos off Nuclei

Contents

1.1. Introductory Perspectives on Reactor Neutrino Physics

"I have done a terrible thing, I have postulated a particle that cannot be detected." Wolfgang Pauli stated in December 1930 [1], after he proposed the existence of a neutral elementary particle in an open letter to the "Radioactive Group" (a group of physicists who had gathered in Tübingen, Germany to discuss the latest developments in nuclear physics), motivating it as a "desperate remedy" for the inexplicable observation of the continuous beta spectrum. This wide spread of energy of the beta particles from nuclear decay only became understandable - without violating the conservation of energy - with the assumption of a third particle involved in the decay process in addition to the electron and the nucleus from which it originated. The name that was historically assigned to this neutral particle, whose mass was at the time already determined to be considerably less than that of the proton, is *neutrino*. Pauli's idea, how unfavorable it may have seemed to him, nevertheless had an early impact.

First Detection of Neutrinos at a Nuclear Fission Reactor

In the years following the meeting in Tübingen, Enrico Fermi worked out a theory of beta-decay [2], which turned out to be an important precursor to the theory for the weak interaction, representing its low-energy approximation. In addition, large efforts have been made towards an experimental confirmation of the particle. Hans Bethe and Rudolf Peierls [3] contributed to these attempts in 1934 with the recognition of the theoretical possibility of an inverse beta decay, by which the neutrino ought to be measurable.

However, due to its elusive nature, it took 22 more years until the first experimental detection of the neutrino by Clyde L. Cowan and Frederick Reines in 1956 [4]. The choice of experimental site was fundamentally shaped by the requirement to ensure a sufficiently high flux of neutrinos. Initial considerations to make use of the neutrino bursts from atomic weapon tests were eventually discarded in favor of the installation of the experiment at a site

close to a nuclear fission reactor. Cowan and Reines thus recognized early on the potential of nuclear reactors as an intense and clean source of neutrinos, opening up a long-lasting and successful branch of research, which will be further discussed in Section 1.2. The award of the Nobel Prize in physics 1995 to Frederick Reines "for the detection of the neutrino" [5] reflects how much the field of neutrino physics has flourished in the wake of the predictions by Pauli, Fermi et al. and the experimental confirmation by Cowan and Reines.

Thriving Neutrino Physics

The thriving of the field can certainly be attributed to the unique position that the neutrino - a solely weakly and gravitationally interacting fermion, that interacts in the three different leptonic flavors - takes within the Standard Model of Particle Physics (SM), making it arguably the main door into physics beyond the Standard Model. This becomes particularly evident in the Nobel Prize in physics 2015, awarded to Takaaki Kajita and Arthur B. McDonald "for the discovery of neutrino oscillations, which shows that neutrinos have mass" [6]. Neutrino oscillations, which were initially suggested by Bruno Pontecorvo in 1957 [7, 8], are a phenomenon arising from the mixing between the individual flavor and mass eigenstates of neutrinos, and are as such governed by quantum mechanics. The observation [9] of these neutrino oscillations requires (contrary to the current formulation of the SM) that neutrinos exhibit mass, and therefore that the SM features so far unexplored mass-generating mechanisms [10].

Of particular note here, not only because of the context of this thesis, is a type of neutrino coupling that has been cleanly predicted by the Standard Model since the 1970s. Only recently (and hence characteristic of the delayed, because technologically very challenging progress in neutrino physics) it came into the focus of dedicated experimental investigation. This is the coherent elastic neutrino-nucleus scattering, discussed in more detail in Section 1.3, which is expected to yield precision tests of the Standard Model [11] and thus potentially represents an interesting tool to probe physics beyond the Standard Model. An explanation on why nuclear fission reactors constitute one of the main experimental sites in the search for this type of interaction is provided below. An overview of different experimental approaches for detecting coherent elastic neutrino-nucleus scattering at nuclear fission reactors will be given in Section 1.4.

1.2. Reactor Neutrino Experiments

Starting from the discovery of the neutrino by Clyde L. Cowan and Frederick Reines [4], reactor neutrino experiments have played a key role in the history of neutrino physics. Nuclear fission reactors (in particular light water reactors) release energy mainly via the fission of the four isotopes ^{235}U, ^{238}U, ^{239}Pu and ^{241}Pu and the subsequent chain of beta-decays of their neutron-rich daughter nuclides [12]. These four isotopes account for $> 99\,\%$ of the total fission yield [13]. Each fission produces about $\sim 200\,\mathrm{MeV}$ and releases on average six electron antineutrinos $\bar{\nu}_e$. This makes nuclear reactors one of the strongest artificial continuous neutrino sources and explains the importance of reactor neutrino experiments for both the discovery and the performance of precision measurements throughout the history

of neutrino studies. The mean energy of the emitted neutrinos from fission processes has a value of around 1.5 MeV and can reach up to 10 MeV [13]. This allows for measurements of neutrinos involved in low energy nuclear processes such as inverse beta-decay (IBD), and in addition, makes nuclear power plants promising sources for the detection of even lower-energetic, threshold-less processes such as coherent scattering [14]. The standard detection method for reactor electron antineutrinos is given by the IBD process

$$\bar{\nu_e} + p \rightarrow n + e^+ \tag{1.1}$$

in which an antineutrino $\bar{\nu_e}$, scattering off a proton p, creates a positron e^+ and a neutron n. The IBD offers a very clear experimental signature due to the prompt annihilation of the positron with a surrounding electron and the delayed nuclear capture of the neutron. The released gammas in this process - two with energies of 0.511 MeV each from the positron annihilation and several more with energies between 2.2 MeV (for capture on hydrogen) and 8 MeV (for capture on gadolinium) following the delayed nuclear capture - can be detected by scintillator detectors [15].

Historically, this process has been exploited for measurements of reactor neutrino oscillations [16]. The low energy of reactor antineutrinos implies a short oscillation length. Furthermore it has to be taken into account that IBD as standard detection method is a charged-current interaction. In consequence, reactor neutrino experiments are restricted to searches for electron antineutrino disappearance, as the energy of the emitted antineutrinos is not sufficient to produce muons or taus [12]. These premises make reactors a predestined tool for measurements of the smallest of the mixing angles, θ_{13} [17], which is phenomenologically accessible in measurements of $\bar{\nu_e}$-disappearance over $\sim$km distances. The CHOOZ experiment [18] - located near the Chooz nuclear power plant operated by *Électricité de France* in the Ardennes region - did not observe any disappearance of $\bar{\nu_e}$, although it introduced modern particle physics technology, such as detector Monte Carlo (MC) simulations and a complex veto design [19] into reactor neutrino experiments. Nevertheless, a long standing and fruitful tradition of neutrino experiments at the Chooz nuclear power plant was established. The baseline of 1.05 km of the 5 m^3 gadolinium-doped liquid scintillator target to the two N4-type Pressurized Water Reactors with a nominal power of 4.25 GW_{th} each, was not sufficient by itself to resolve the mixing angle θ_{13} [20]. However, new limits on the neutrino oscillation parameters were set. Consecutively, a new concept of reactor experiments based on a relative measurement between two identical detectors to cancel out most of the systematic uncertainties was realized in the Double Chooz experiment [21], leading to unprecedentedly precise measurements of reactor neutrino oscillations. The value of θ_{13} was measured to be $sin^2 2\theta_{13} = 0.090^{+0.032}_{-0.029}$. A variety of additional experiments like the Daya Bay experiment [22], the KamLAND experiment [23] or the RENO experiment [24], covering several experimental techniques and baselines, opened the door to a new era of precision measurements of reactor neutrino oscillation parameters [19]. The capability of reactor neutrino experiments to determine the neutrino mass ordering - phenomenologically enabled by the large value of θ_{13} - has become of great interest in modern neutrino physics and is subject of recent experimental efforts [25].

New generation experiments, for which latest technological detector developments opened the gateway, are reaching unprecedentedly low energy thresholds and commonly feature a sophisticated shielding design which allows for operation under above-ground conditions. This, for the first time, allows neutrino detection via coherent scattering, based on the

neutral-current interaction

$$\bar{\nu_e} + A_N^Z \rightarrow \bar{\nu_e} + A^{*Z}_N \tag{1.2}$$

in which an antineutrino scatters off a nucleus elastically. Taking into account both the low energy of reactor antineutrinos - as indispensable requirement for the scattering to be in the coherent regime - and their large flux - as promoting factor to assure a sufficient signal to background ratio - nuclear fission reactors seem to be a promising source for the measurement of coherent elastic neutrino-nucleus scattering [26].

1.3. Coherent Elastic Neutrino-Nucleus Scattering

The occurrence of neutral-current neutrino interactions within the Standard Model of Particle Physics implies the coupling of neutrinos to quarks through the exchange of neutral Z bosons [27]. In 1974, Daniel Z. Freedman suggested furthermore the existence of elastic neutrino-nucleus scattering. This mechanism predicts strong coherent effects at very low neutrino energies of $\mathcal{O}(10\,\mathrm{MeV})$ and should therefore cause neutrinos to interact coherently with protons and neutrons in a nucleus [28]. For a nucleus at rest with Z protons and N neutrons its cross-section [29] is approximately given by:

$$\frac{d\sigma}{dE_R} = \frac{G_F^2}{4\pi} Q_W^2 F^2(q^2) \cdot m_N \left(1 - \frac{E_R}{E_R^{max}}\right) \tag{1.3}$$

where G_F denotes the Fermi constant, Q_W the nuclear weak charge, m_N the total mass of the nucleus, E_R the nuclear-recoil energy and $F(q^2)$ the nuclear form factor as a function of the momentum transfer q. The weak charge Q_W is given by $Q_W = N - Z \cdot (1 - 4 \cdot \sin^2\theta_W)$ where θ_W is the Weinberg angle. The maximum nuclear recoil energy E_R is given by $E_R^{max} = 2E_\nu^2/(m_N + 2E_\nu)$, with E_ν designating the initial neutrino energy. For neutrinos with $E_\nu \leq 50\,\mathrm{MeV}$[1] (corresponding to length scales of $\gtrsim 10^{-14}\,\mathrm{m}$ and low momentum transfer q), the nuclear form factor $F(q^2)$ is close to unity and the scattering therefore becomes coherent [29].

The large cross-section of those neutral-current neutrino interactions is due to their coherent character boosted by a factor of N^2. Thus, compared to standard neutrino detection methods such as inverse beta-decay, the coherent cross-section is enhanced by more than two orders of magnitude [30]. On the contrary, the energy of the nuclear recoil E_R, which represents the only measurable effect of coherent neutrino scattering, is suppressed by the nucleus mass m_N. Moreover, while the kinetic energy of antineutrinos scattering off a proton in an IBD needs to be higher than 1.8 MeV [31], the coherent scattering of neutrinos does not imply any energy threshold. Coherent elastic neutrino-nucleus scattering (CEνNS) therefore offers the unique possibility to probe the Standard Model at very low energies and seems to be a predestined tool to expand our knowledge about fundamental neutrino properties. Consequently, the detection of CEνNS not only yields the completion of the picture of the fundamental neutrino couplings predicted by the SM [30], but can also be used for measurements of the Weinberg angle θ_W at low momentum transfer [32], the examination of the existence of a neutrino magnetic dipole moment [33] or to put new constraints on the existence of sterile neutrinos [34]. Apart from that, an accurate measurement of CEνNS is

[1] The energy, for which the elastic scattering of neutrinos becomes coherent, depends on the size of the nucleus the neutrino is scattering off.

of phenomenological importance for future searches of dark matter, given the fact that solar and atmospheric neutrinos represent an ultimate background to dark matter direct detection experiments [35]. Any deviation from SM predictions would furthermore yield the potential discovery of new physics beyond the SM, such as modified V-A quark-neutrino couplings [29] or new exotic neutral currents [36].

Due to the elusiveness of its experimental signature, CEνNS has not been detected for more than four decades. Latest technological developments in dark matter direct detection experiments were a key factor towards the first measurement of CEνNS [36], which has been reported by the COHERENT collaboration in September 2017 [30]. The process has been observed at a $6.7\,\sigma$ confidence level using a low-background, 14.6 kg scintillating CsI[Na] target crystal and a $4.3{\cdot}10^7\,\nu/(\mathrm{s}{\cdot}\mathrm{cm}^2)$ neutrino beam produced by the Spallation Neutron Source at Oak Ridge National Laboratory. The neutrino energy spectrum produced by this source is reaching up to 50 MeV - the resulting CEνNS is therefore located partially above the coherent regime. In 2020, the COHERENT collaboration has additionally reported the first detection of coherent elastic neutrino-nucleus scattering on argon, using a 22 kg, single-phase liquid argon detector, equally operated at Oak Ridge National Laboratory [37]. With this measurement - on the lightest nucleus for which CEνNS has ever been observed - the expected neutron-number dependence of the cross-section was verified.

1.4. Searching for CEνNS at Nuclear Fission Reactors

Due to the growing attention to CEνNS within the particle physics community, a multitude of collaborations have induced a wave of progress in the development of novel ultra-low threshold detectors [38, 39]. Particular emphasis is currently being placed on measuring CEνNS of reactor antineutrinos, which to date is still pending. The search for CEνNS in the immediate vicinity of nuclear fission reactors as an intense and suitable source of electron antineutrinos is therefore being addressed by a variety of collaborations, which collectively offer a broad range of detector technologies. A non-exhaustive overview of the experimental approaches is given below.

While the CONUS collaboration [40] is instrumenting commercial kg-sized point contact germanium detectors with an energy threshold for nuclear recoils of $\mathcal{O}(1\,\mathrm{keV})$ at a distance of 17 m to the $3.9\,GW_{th}$ nuclear reactor core in Brokdorf, Germany, the TEXONO collaboration [41] is instrumenting a similar detector technology with a baseline of 28 m to the $2.7\,GW_{th}$ nuclear reactor core in Kuosheng, Taiwan. Both experiments have been successfully commissioned. The CONNIE collaboration [42] operates low-noise fully depleted charge-coupled devices (CCDs), aiming for a measurement of CEνNS of reactor antineutrinos off Silicon nuclei. The experiment, which is already running, is installed in the vicinity of a nuclear fission reactor with a nominal power of $3.8\,GW_{th}$ in Angra, Brazil. An alternative detector technology, which promises an unprecedentedly low energy threshold for nuclear recoils, is based on cryogenic detectors. The MINER collaboration [43] is envisaging several 600 g cryogenic (Ge/Si) detectors, which were developed within the frame of the direct dark matter search with CDMS-II. The variable baseline between 2 m and 10 m to a $1\,GW_{th}$ nuclear reactor core in Texas, USA makes MINER especially interesting for the search for sterile neutrinos. The RICOCHET collaboration [39], investigating both Ge-based and metallic Zn-based cryogenic calorimeters, is constructing an experiment at a $58\,MW_{th}$ reactor in Grenoble, France.

The technology envisaged by the NUCLEUS collaboration (in whose framework the submitted work was conducted) [44], which has to date demonstrated the lowest energy threshold for nuclear recoils of $E_{th} = (19.7 \pm 0.8)\,\mathrm{eV}$ [45], will be installed near the Chooz nuclear power plant in France. The site, the sources of background and the experimental setup are presented in detail in the following chapter.

2. The NUCLEUS Experiment

Contents

The NUCLEUS collaboration is developing a new-generation experiment to probe CEνNS, exploiting ultra-low threshold cryogenic calorimeters [44]. The foundations of the cryogenic detector technology envisioned by NUCLEUS were set within the CRESST (Cryogenic Rare Event Search with Superconducting Thermometers) experiment, achieving leading sensitivity in low-mass dark matter search [46]. The installation of the NUCLEUS experiment at an experimental site close to the Chooz nuclear power plant represents a continuation of the tradition of reactor neutrino experiments at this particular site and allows a large-statistics experiment with reactor antineutrinos sufficiently low in energy for the elastic neutrino-nucleus scattering to be in the fully coherent regime [44].

2.1. The NUCLEUS Experimental Site

The experimental site that has been chosen for the NUCLEUS experiment is a compact 24 m^2 room situated in the basement of a five-story office building on the area of the Chooz nuclear power plant (shown in Figure 2.1) featuring an overburden of only $\sim$3 m.w.e.. The *Centrale nucléaire de Chooz* lies in the municipality of Chooz in the Ardennes department and is operated by the French electric utility company *Electricité de France* (EDF). Two N4-type pressurized water reactors, each running with a nominal thermal power of 4.25 GW$_{th}$, are separated by 160 m. Assuming an average emission of six electron-antineutrinos $\bar{\nu}_e$ per fission, a 4.25 GW$_{th}$ power reactor is expected to release a total of $8{\cdot}10^{20}$ $\bar{\nu}_e$/s [47].

Both the CHOOZ experiment [18], and its successor Double Chooz [21] have been previously installed in dedicated experimental sites in the vicinity of the Chooz nuclear power plant. In the attempt to implement the idea of relative measurements between two identical detectors outlined in Section 1.2, two separate sites (denoted as 'Double Chooz far site' and 'Double Chooz near site') were established for Double Chooz. In continuation of this

naming convention, the site for the NUCLEUS experiment, which is considerably closer to the reactor cores than the existing sites, will be referred to as 'Very Near Site' (VNS). The baseline of the experimental site to the two reactor cores is 72 m and 102 m. The expected neutrino flux inside the VNS can be calculated to $10^{12}\,\bar{\nu}_e/(\mathrm{s}{\cdot}\mathrm{cm}^2)$.

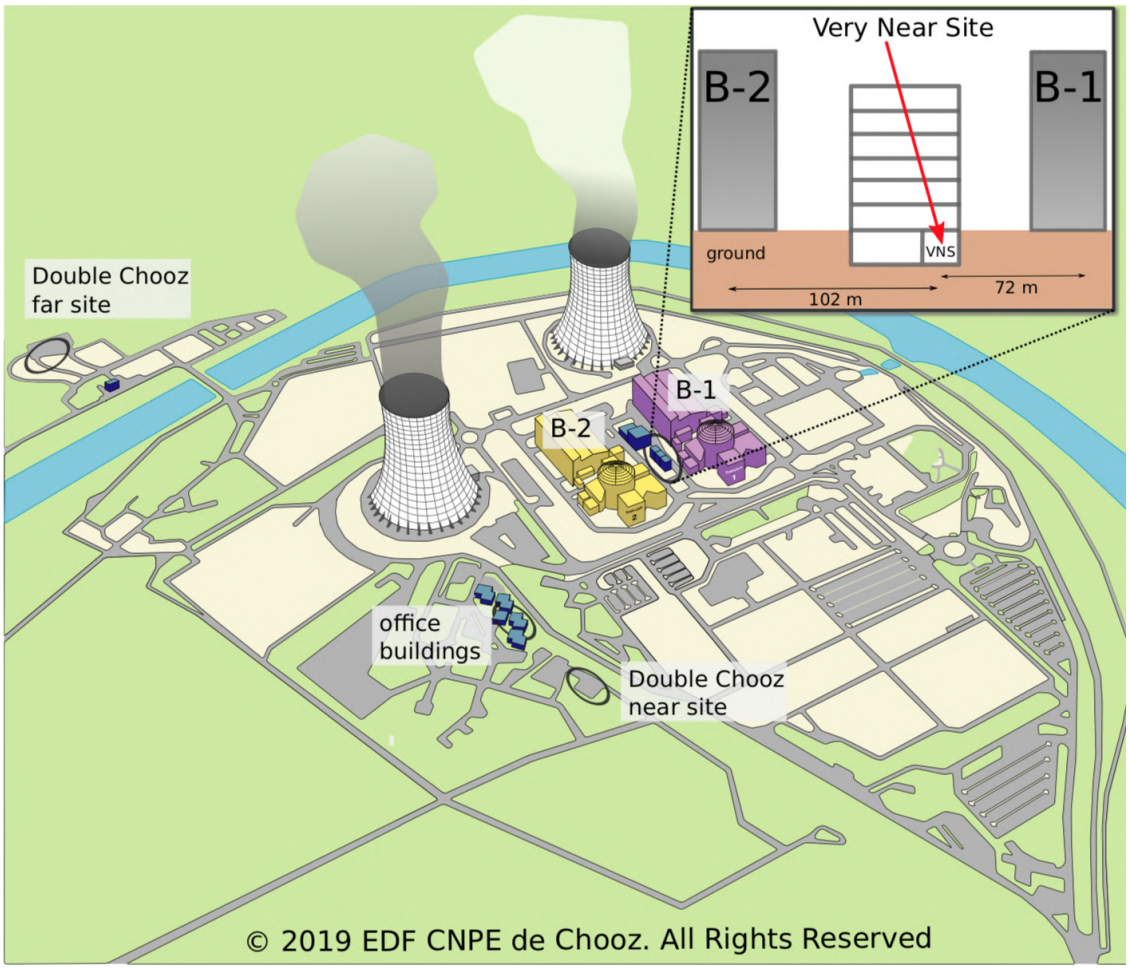

Figure 2.1.: *Schematic drawing of the Chooz nuclear power plant. The experimental site of NUCLEUS (denoted as 'Very Near Site') is located inside an office building in between the two reactor cores and is shown in the inset on the top right of the scheme. The baselines to the two reactors B1 and B2 are 72 m and 102 m, respectively. The two sites of the Double Chooz experiment, that have as well been installed at the Chooz nuclear power plant, are also marked. Figure taken from [44].*

2.2. Sources of Background

The choice of an experimental site at shallow depth close to a nuclear reactor makes it possible to reach considerably high neutrino fluxes, but is due to the above-ground conditions accompanied by the necessity to take special care of several sources of background. In the following, the various sources are categorized into *external and internal background*, as well as *cosmic-ray induced background* [44]. The *reactor-correlated background* - namely the fission-induced neutrons produced inside the two reactor cores of the Chooz nuclear power plant -

is assumed to be negligible for the NUCLEUS experiment [48].

External and internal background The external background mainly consists of gamma-rays originating from α- and β-decaying nuclides in the ^{232}Th, ^{238}U and ^{235}U as well as the ^{40}K decay chains present in the material surrounding the experiment, together with the ambient neutrons present in the VNS originating from nuclear (α,n) reactions of the ^{232}Th and ^{238}U decay chains or spontaneous ^{238}U fission [49]. If unstable nuclides are decaying inside the target detector itself, the resulting radiation is classified as internal background. Those events can be avoided by using highly pure materials for the target crystal growth and by assuring their purity by special measures during their production [50].

Cosmic-ray induced background At shallow overburden muons and neutrons account for the main contribution to the cosmic-ray induced background [51]. Other components of cosmic-ray induced air showers (for instance electrons, gammas, protons and pions) are efficiently filtered out by the building structure. In particular, neutrons are an especially harmful background, as due to their neutral character they lead to the same experimental signature (i.e. a nuclear recoil) as the sought-for coherent elastic neutrino-nucleus scattering. Neutrons can be produced via muon-induced spallation reactions. To this end, a measurement campaign to characterize the neutron- and muon-background was performed at the experimental site in 2018 [44]. This campaign served to determine the flux reduction at the experimental site compared to the surface. It was shown that the muon-flux is attenuated by a factor of 1.41 ± 0.02, whereas the neutron-flux is attenuated by a factor of 8.1 ± 0.4. Besides the atmospheric and the muon-induced neutrons, non-vetoed muons constitute a dangerous background themselves, since they can either decay in the direct vicinity of the target detector and give rise to an electron or a positron[1] or be absorbed by a ^{12}C nucleus and create an excited ^{12}B that decays subsequently[2] with a mean lifetime of about 20 ms [52].

2.3. The NUCLEUS Detector Concept

The NUCLEUS detector concept is based on a gram-scale fiducial-volume cryogenic detector consisting of three individual calorimetric systems operating at milli-Kelvin temperatures. The base temperature of $\mathcal{O}(10\,\mathrm{mK})$ is provided by a dry dilution refrigerator. The background conditions specified above pose special demands on the shielding technique and make a multi-stage background rejection inevitable [44]. The two-fold fiducialization of the NUCLEUS detector into a cryogenic inner and outer veto operating as anticoincidence detectors is the first step towards sufficient background rejection. Additionally, external passive and active shielding is indispensable, which will be discussed in more detail in Section 2.4. The NUCLEUS technology promises an ultra-low target detector threshold of $E_{th} \sim 20\,\mathrm{eV}$ and low systematics. The main components of the NUCLEUS experimental setup, namely the cryostat, the experimental volume with the fiducialized cryogenic detector, the external passive shielding as well as the muon veto can be seen schematically in Figure 2.2.

[1] $\mu^{\pm} \rightarrow e^{\pm} + \nu_e + \nu_\mu$
[2] $\mu^- + ^{12}C \rightarrow ^{12}B* \rightarrow ^{12}C + e^- + \bar{\nu}_e$

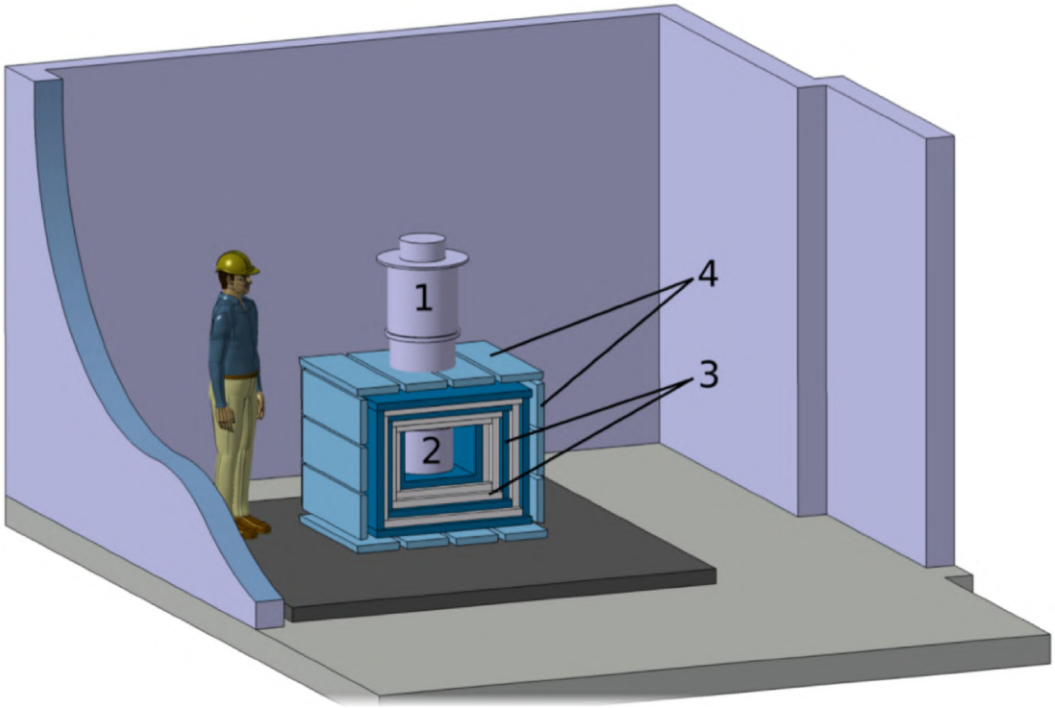

Figure 2.2.: *Schematic drawing of the NUCLEUS experimental setup at its experimental site at the Chooz nuclear power plant. The experiment consists of a dry dilution refrigerator (1) containing the experimental volume (2) with the target detector and the cryogenic inner and outer veto. It is shielded by layers of external passive shielding (3) consisting of polyethylene and lead. The outermost layer is an active muon veto (4). The external shielding will be discussed in more detail in Section 2.4. Figure taken from [44].*

2.3.1. Dry Dilution Refrigerator

A dry dilution refrigerator is used to cool the NUCLEUS detector module to its transition temperature of $\mathcal{O}(10\,\mathrm{mK})$. The NUCLEUS experiment deploys a commercial LD 400 ^{3}He/^{4}He dilution refrigerator provided by Bluefors [53], which can be seen in Figure 2.3. Compared to conventional wet dilution refrigerators, dry dilution refrigerators feature the advantage of not requiring any external supply of cryogenic liquids in the cooling process except for the dilution mixture. Pre-cooling of the refrigerator is achieved using a cryogen-free pulse tube refrigerator. In order to mitigate the vibrations induced by the pulse tube refrigerator dedicated works on vibration decoupling are ongoing.

The principle of dry ^{3}He/^{4}He dilution refrigerators is the mixing of the two helium isotopes ^{3}He/^{4}He at low-temperatures. This mixture undergoes a spontaneous phase separation forming a ^{3}He-rich phase (concentrated phase) and a ^{3}He-poor phase (diluted phase) when being cooled below $\sim 870\,\mathrm{mK}$. While the concentrated phase is essentially pure ^{3}He, the diluted phase is composed of about 6.6 % ^{3}He and 93.4 % ^{4}He. Inside the mixing chamber of the cryostat, which is where the phase separation between ^{3}He and ^{4}He takes place, external pressure removes ^{3}He from the diluted phase. In order to maintain the thermodynamic equilibrium of the diluted phase, which is at a ^{3}He concentration of 6.6 %, ^{3}He is driven to evaporate from the concentrated phase through the phase boundary into the dilute phase. The heat necessary for the dilution is extracted from the environment and corresponds to the cooling power of the cryostat [54].

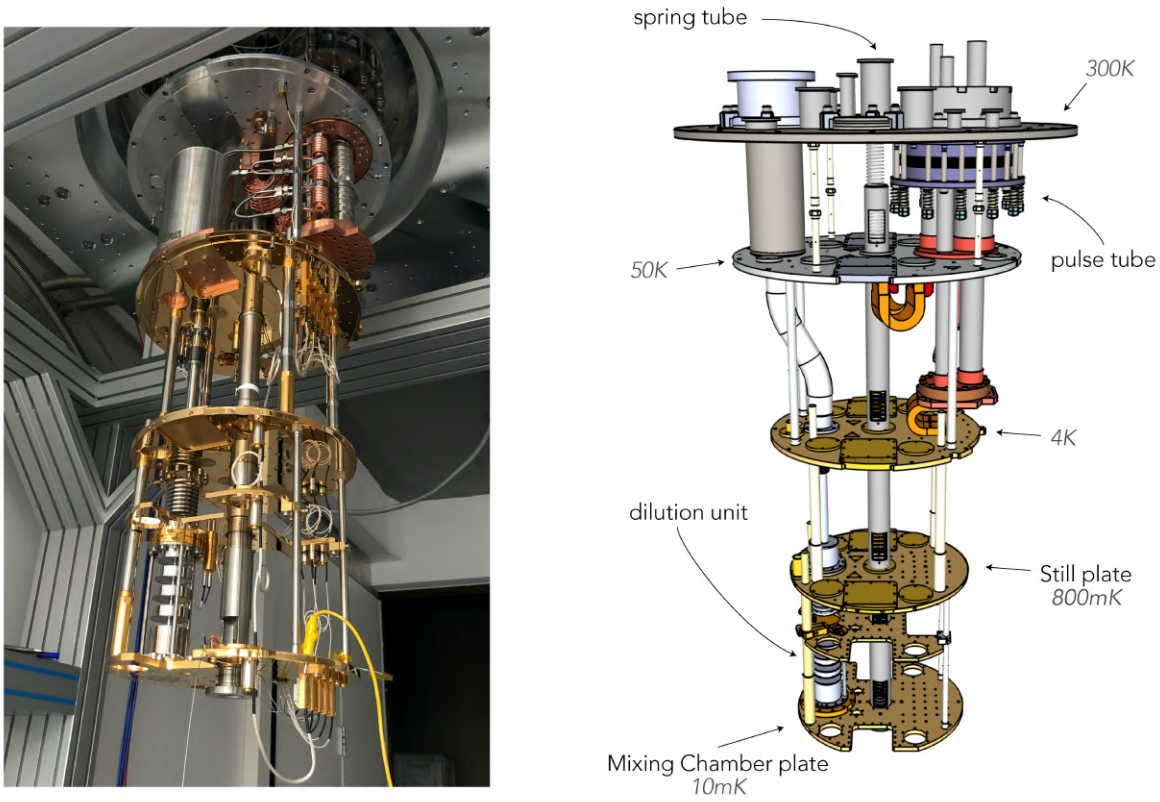

Figure 2.3.: *Picture (left) and schematic drawing (right) of the inner part of the Bluefors LD 400 cryostat. The device is a dry dilution refrigerator, exploited to cool the experimental volume of the NUCLEUS experiment down to temperatures of $\mathcal{O}(10\,\mathrm{mK})$. The individual temperature stages are indicated in the schematic drawing. The base temperature is only reached in the bottom plate of the cryostat (the so called mixing chamber plate) to which the dilution unit containing the $^3He/^4He$ mixture is thermally coupled. The pulse tube, responsible for the pre-cooling of the cryostat to 4 K is installed in the upper part of the cryostat. A spring tube - encapsulating a spring which is used for vibration-mitigation on the target detector - is guided through the center of the cryostat.*

2.3.2. Target Detector

The target detector is an array of gram-scale cryogenic calorimeters made of the crystalline materials $CaWO_4$ and Al_2O_3, schematically shown in Figure 2.4 together with the cryogenic inner and outer veto. The operation of these crystals at temperatures of $\mathcal{O}(\mathrm{mK})$ at their transition point between the normal- and the super-conducting phase leads to a measurable temperature rise $\Delta T = \Delta E/C$ induced by the small energy deposition ΔE inside the target when an external particle undergoes scattering within the detector. At the transition point of the crystal, the heat capacity C is small enough to yield a temperature rise that can be read by thin-film tungsten transition edge sensors. The multi-target approach allows an in-situ background characterization, exploiting the enhanced coherent scattering cross-section on the heavy nuclei of the tungsten isotopes in $CaWO_4$ for the observation of the CEνNS process (see equation 1.3), while additionally operating Al_2O_3 yields complementary information on the rate of background events (mainly due to the scattering of fast neutrons off the oxygen nuclei equally present in both target materials).

The feasibility of this technology for the usage in neutrino detection has been successfully demonstrated in 2017 using a $(5 \times 5 \times 5)\,\mathrm{mm}^3$ Al_2O_3 prototype cube with a mass of 0.5 g [45]. The decisive finding of this cited study by R. Strauss et al. is the possibility of lowering the energy threshold of an absorber by reducing its size. Given that the rise time of cryogenic calorimeters is governed by the thermalization of the signal phonons at the surface of the absorber crystal and is thus expected to scale roughly with the linear dimension of the target detector, the pulse rise time of the NUCLEUS gram-scale crystals is only in the order of $\mathcal{O}(100\,\mu\mathrm{s})$ [44, 55] and is therefore significantly faster than previous larger-scale CRESST-detectors [46]. Furthermore, the scalability of this cryogenic technology, enabled by the operation of a multiplicity of single crystals, allows the target mass to be upgraded from NUCLEUS-10g, as envisaged for the first phase, to NUCLEUS-1kg for the second phase.

2.3.3. Cryogenic Inner and Outer Veto

To achieve a sufficient background rejection and to ensure the operation of the NUCLEUS experiment at shallow overburden, the target detector will be held and encapsulated by a low threshold inner veto and a surrounding kg-scale cryogenic detector used as outer veto. Both can be schematically seen in Figure 2.4 together with the target detector.

- The cryogenic inner veto is essentially an instrumented holder, operating as low threshold cryogenic detector against α and β surface contamination and is implemented using elastic silicon wafers equipped with thin-film tungsten transition edge sensors. In this way, a nearly $4\,\pi$ coverage of the target detectors with sub-keV threshold can be achieved, compensating for residual internal contaminations of the target detector.
- The cryogenic outer veto is a kg-scale cryogenic timing detector operating in anti-coincidence with the target detectors and is essential for suppressing penetrating ambient γ and neutron backgrounds. The usage of high-Z materials such as germanium allows scalable detector masses up to $\mathcal{O}(\mathrm{kg})$ and energy thresholds of $\mathcal{O}(\mathrm{keV})$. The cryogenic outer veto offers excellent gamma rejection and additional capacity for further rejection of hitherto undetected muons.

The innovative design and the customized interconnections between the individual components of the NUCLEUS cryogenic veto systems, together with the external passive shielding and the active muon veto promises excellent suppression $\mathcal{O}(10^3)$ of the background.

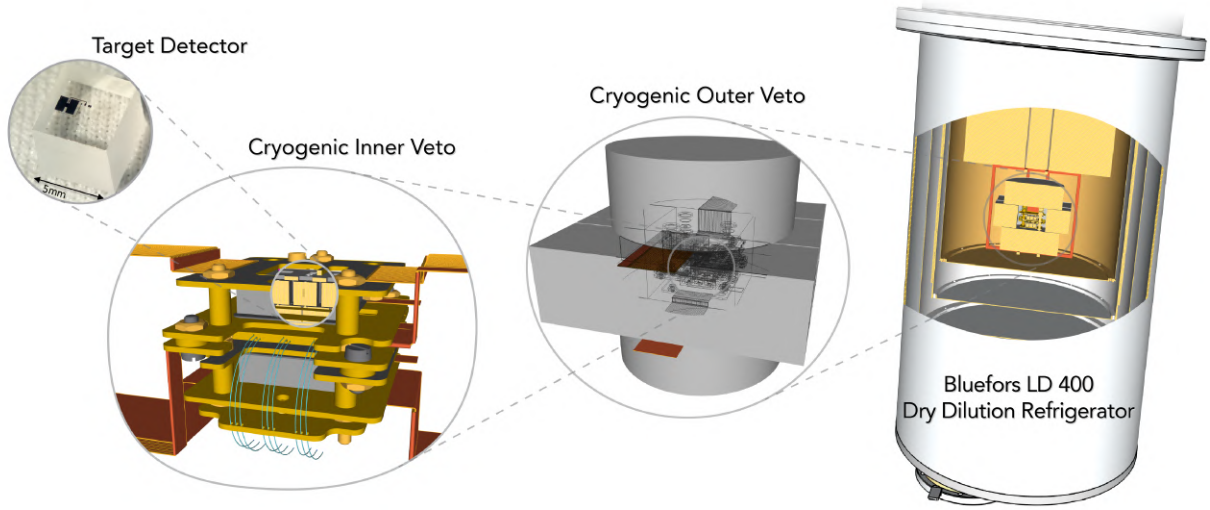

Figure 2.4.: *Schematic drawing of the experimental volume of the NUCLEUS experiment installed inside the cryostat (first picture from the right), with detailed zoom-in on its several sub-components. The active outer veto (second picture from the right) is a kg-scale cryogenic timing detector mainly suppressing ambient γ and neutron backgrounds and encapsulating the active inner veto (second picture from the left). This is essentially an instrumented holder with almost 4π coverage of the target detector, operating as low threshold cryogenic detector against α and β surface contaminations. The target detector is an array of gram-scale cryogenic calorimeters made of the crystalline materials $CaWO_4$ and Al_2O_3 (one of which is shown in the first picture from the left).*

2.4. The NUCLEUS External Shielding

2.4.1. External Passive Shielding

NUCLEUS aims to achieve a background count rate of 10^2 counts / (keV kg day) in the sub-keV region [44]. Gamma-rays and ambient neutrons, originating from environmental radioactivity in the concrete of the laboratory building (which are categorized above as external background) can be efficiently shielded by a passive shielding structure consisting of graded layers of lead and borated polyethylene. The passive shielding furthermore suppresses a possible remaining nucleonic component of cosmic-rays. Due to the interconnection with the cryogenic outer veto, which offers excellent gamma rejection, the passive shielding focuses on minimizing the muon-induced backgrounds, especially the secondary neutrons reaching the experimental volume. For this purpose, the inner layer of the passive shielding is made out of borated polyethylene and is moderating and absorbing neutrons. The outer layer is made out of lead and is attenuating gammas. The neutron background caused by muon-induced spallation is enhanced in high-Z materials such as lead. By keeping the thickness of the lead layer relatively low, this source of background can be restricted to a minimum. Currently, a thickness of 5 cm for the lead layer is envisaged [56].

2.4.2. The NUCLEUS Muon Veto

Due to the fact that cosmic muons cannot be sufficiently attenuated by a passive shielding, muon-induced backgrounds have to be actively rejected. In the case of NUCLEUS - in which the necessity of an efficient muon veto system due the experiment's operation at a shallow experimental site with above-ground background conditions is particularly evident - this shall be achieved by operating an active, plastic scintillator based muon veto, customized to the particular constraints and requirements of the NUCLEUS experiment [44].

Constraints

The cosmic muon count rate at the earth's surface is $\sim 100\,\mathrm{Hz}\,/\,\mathrm{m}^2$ [57]. The expected count rate of cosmic muons adjusted to the NUCLEUS muon veto geometry is determined to be $\sim 700\,\mathrm{Hz}$ (see Section 4.2.3). By making the muon veto as compact as possible and the timing of the muon events sufficiently fast, the resulting detector dead time can nevertheless be kept low. Although the overall detector dead time is governed by the timing of the cryogenic pulses, the exceptionally fast rise-time of the NUCLEUS cryogenic detectors (see Section 2.3) - compared to conventional cryogenic detectors - promises detector dead times of only $\sim 1\,\%$ [44]. In addition to that, the compactness of the NUCLEUS muon veto is an important criterion to avoid possible conflicts with the spatial constraints dictated by the dimensions of the VNS (see Section 2.1). In this context, the external dimensions of the muon veto must not significantly exceed a length of $\sim 1.2\,\mathrm{m}$.

Requirements

In order to reach the required background count rate of $10^2\,\mathrm{counts}\,/\,(\mathrm{keV\ kg\ day})$ in the sub-keV region [44] - and despite the constraints mentioned above - a very high muon detection efficiency of more than $99\,\%$ is envisaged. An important condition for making this target achievable is not only the achievement of a nearly complete coverage of all the $4\,\pi$ steradians of solid angle around the NUCLEUS target detector and of high-Z materials present in its vicinity, but also the assurance of a sufficient discrimination capability between muons and gammas. This discrimination is crucial to minimize false veto signals induced by gammas and thereby not unnecessarily increase the overall dead time. As the amplitude of a muon signal produced by the plastic scintillator is proportional to the energy deposition therein, the discrimination power of a plastic scintillator muon veto scales with the thickness of the instrumented plastic scintillator. Apart from that, a high uniformity of light yield over the whole muon veto arrangement and a negligible spatial dependence are important requirements that need to be fulfilled by the NUCLEUS muon veto.

The challenging constraints together with the specific requirements of NUCLEUS explain the necessity of the dedicated R&D process, that was undertaken for the NUCLEUS muon veto. A detailed review of the development of the NUCLEUS muon veto can be found in [58]. Moreover, a devoted technical paper is being in preparation [59].

General Design Considerations

For the NUCLEUS experiment, an active muon veto, consisting of a casing of 24 single organic plastic scintillator panels with a thickness of 5 cm, each encapsulated in a light-tight aluminium box, has been designed (see Figure 2.2) and developed. In the following, this arrangement will be denoted as the *Outer Muon Veto*. The instrumented panels, that are based on the synthetic polymer polyvinyltoluene (PVT), were recovered from the CAMERA detector of the COMPASS-II experiment at CERN[3], and were demounted in 2018 [62]. The initial panels have a trapezoidal cross-section (shown in Figure 2.5) and a length of 360 cm. For the NUCLEUS muon veto, their dimensions will be changed and adapted.

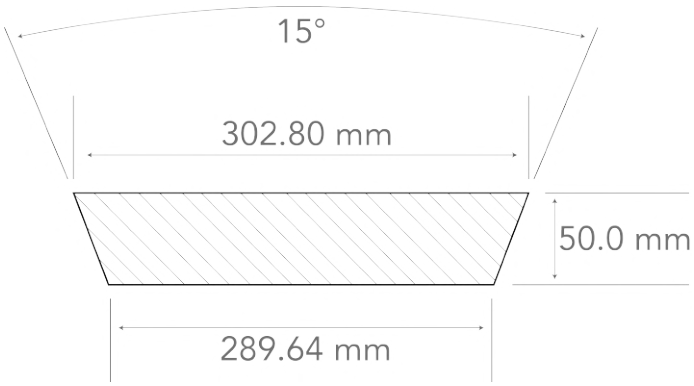

Figure 2.5.: *Cross-section of the plastic scintillator panels, recovered from the CAMERA detector of the COMPASS-II experiment. The panels have a trapezoidal shape. The thickness of 5 cm assures sufficient discrimination capability between muons and gammas. Figure adapted from [61].*

With an average energy loss of $\sim 2\,\mathrm{MeV}\,/\,\mathrm{cm}$ and an average muon energy of 4 GeV, it is expected that a through-going muon deposits about 10 MeV in a veto panel [57]. The most energetic gamma-ray from natural radioactivity is at 2.6 MeV and can therefore be efficiently discriminated from muons by a simple energy cut. If an event registered by the muon veto exceeds the energy threshold, a trigger signal is generated. These muon events can later be removed offline from the data and disregarded in the analysis.

For the above mentioned requirement of compactness, it was decided to instrument a wavelength shifting (WLS) fiber based light-guide system together with a Silicon-Photomultiplier (SiPM) based read-out system.

[3]The COMPASS-II experiment aims to address QCD-related studies of the nucleon structure. The main physics goals are the investigation of the nucleon spin structure and hadron spectroscopy. The CAMERA detector was used as recoil proton detector, essential for the measurement of deeply virtual Compton scattering [60, 61].

3. The NUCLEUS Cryogenic Muon Veto

Contents

3.1. Scope of this Thesis

The design of the active and passive shielding of the NUCLEUS experiment features a hole with a diameter of 45 cm in the upper side of the experiment, where the cryostat containing the NUCLEUS detector and its support structure will be inserted. Due to the spatial constraints of the VNS and in order to not further increase the detector dead time it is not preferable to build an additional, umbrella-like active muon veto that covers this hole together with the cryostat from above. It was therefore decided to investigate a novel and innovative concept, which consists of a disc-shaped active muon veto operated inside the cryostat underneath the mixing chamber plate at sub-Kelvin temperatures. The position of the disc with respect to the NUCLEUS experiment can be seen in Figure 3.1, which schematically shows the experiment's cross-section. **The development of this *Cryogenic Muon Veto* for NUCLEUS is the main subject of this thesis.**

This work was developed in equal parts jointly at the *Centre CEA de Saclay* and the *Technical University of Munich (TUM)*. The author of this thesis conducted his research at both institutes for six months at a time. This, on the one hand, made it possible to make efficient use of the synergies with the development of the *Outer Muon Veto* at the CEA. On the other hand, the cryogenic expertise and infrastructure available at TUM were essential for the feasibility of the research. In the following, the development of the NUCLEUS *Cryogenic Muon Veto* will be presented comprehensively, covering these various aspects:

- In order to anticipate and quantify the impact of the NUCLEUS *Cryogenic Muon Veto* on the overall NUCLEUS muon veto performance, an efficiency study was conducted within the frame of this thesis. The study was based on a Monte Carlo simulation framework developed in a collaborative effort by the responsible working group of the *Outer Muon Veto* at *Centre CEA de Saclay*. The contribution of the author of this thesis to the simulation framework consisted primarily in the implementation of the

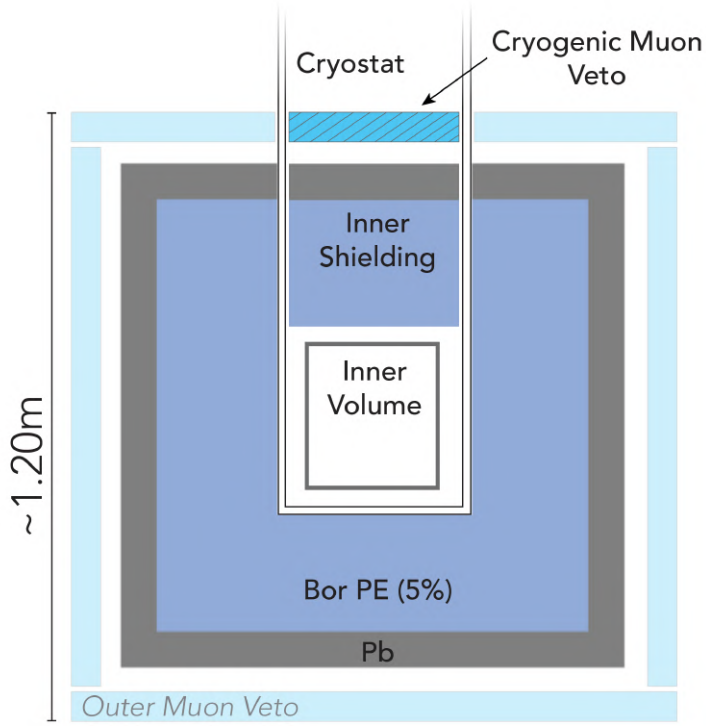

Figure 3.1.: *Schematic, cross-sectional view of the NUCLEUS experiment, showing the position of the Cryogenic Muon Veto (hatched pattern). The design of the NUCLEUS experiment foresees that the cryostat, assuring the refrigeration of the inner volume, enters the Outer Muon Veto and the passive shielding from above, inducing a large and unshielded area. In order to also tag muons impinging from above, the concept of an Cryogenic Muon Veto, operated inside the cryostat at cryogenic temperatures, has been investigated. For the same considerations, the passive shielding, which is composed of graded layers of lead and borated polyethylene, will be as well installed continuously in the inside of the cryostat.*

geometry. Moreover, the results presented in Chapter 4 were obtained explicitly in the context of this thesis.

- As a fundamental proof-of-principle of the NUCLEUS *Cryogenic Muon Veto*, an investigation of the properties and characteristics of organic plastic scintillators at low-temperatures was essential. This resulted in the first reported measurements of organic plastic scintillators at sub-Kelvin temperatures, which clearly verify the key physical aspects of the intended NUCLEUS *Cryogenic Muon Veto* detector concept. The investigation will be presented in Chapter 5.

- The decision to realize a similar detector concept as envisaged in the *Outer Muon Veto*, i.e. a plastic scintillator based detector instrumented with WLS fiber-based light-guide system together with a SiPM-based read-out system, was due to its successful commissioning at room temperature (which will be briefly addressed in the following Section 3.2) and for the sake of comparability and simplicity. The R&D of the NUCLEUS *Cryogenic Muon Veto* was mainly driven by considerations regarding the integration of the whole system with the cryogenic infrastructure of NUCLEUS. Chapter 6 focuses on the design and the production of the NUCLEUS *Cryogenic Muon Veto*. First

measurements with the assembled plastic scintillator disc at room temperature are presented. An outlook on the final installation of the *Cryogenic Muon Veto* inside the NUCLEUS cryostat, which is the next step yet to come, is given.

3.2. Groundwork for the Development of the NUCLEUS Cryogenic Muon Veto

Plastic scintillation detectors are well suited for the detection of muons [49]. An established concept for the read-out of these detectors relies on the instrumentation of light guides and photomultiplier tubes. In case of the NUCLEUS *Outer Muon Veto*, in which compactness is an essential requirement, it was decided to replace the bulky read-out system with space-saving WLS fibers and SiPMs.

The main focus of the R&D process of the NUCLEUS *Outer Muon Veto* was therefore the establishment of a muon veto design, consisting of 24 single organic plastic scintillator panels, that meets the requirements described in Section 2.4.2. For this purpose, a dedicated prototype-test setup has been developed. This setup is suitable for easy and fast handling of different muon veto prototypes, and by that allows the systematic performance of an investigation of different detector arrangements and parameters in an iterative manner. After an evaluation of the performance of the different muon veto prototypes, based on criteria dictated by the specific NUCLEUS requirements, a final geometry could be defined. The prototype-test setup has been developed and operated in an above-ground laboratory of the *Département de Physique Nucléaire* of the *Centre CEA de Saclay* in Paris-Saclay.

During this phase, important groundwork for the NUCLEUS *Cryogenic Muon Veto* was carried out. With the launch of its R&D, the detector concept was already established. Moreover, the expertise of the members of the responsible working group of the *Outer Muon Veto*, namely V. Wagner, D. Lhuillier, R. Rogly, V. Savu and M. Vivier was vital for the progress of the *Cryogenic Muon Veto*.

3.3. Theoretical Foundations for the Development of the NUCLEUS Cryogenic Muon Veto

3.3.1. Organic Plastic Scintillation Detectors

Scintillation detectors make use of the fact that certain materials emit light when traversed by charged radiation, i.e. they scintillate. The most widely applied scintillators include *inorganic crystals*, among them alkali halide crystals such as caesium iodide, as well as *gaseous scintillators*, such as the noble gases helium, argon, krypton and xenon, and *organic-based liquids* and *plastics*. Organic scintillators, which are based on organic molecules with certain symmetry properties, are in general faster than inorganic scintillators, but on the contrary yield less light.

Scintillation Mechanism in Organics

Organic scintillators are made out of aromatic hydrocarbons, featuring benzene-ring structures. The cyclic arrangement of the atoms within these molecules is - due to the formation of a so called delocalised π-electron system, in which electrons are not associated with any particular atom in the molecule - energetically more favourable than the chained arrangement in non-aromatic mesomers. Depending on the arrangement of the electron spins of the π-electrons (parallel or antiparallel), such systems can appear in two different states: singlet states S_i and triplet states T_i. The scintillation mechanism described below is illustrated in Figure 3.2, showing a so called *Jablonski* diagram [63]. When charged particles pass through the scintillating medium, electromagnetic interaction takes place between the molecules of the scintillator and the traversing charged particles. By that, the molecules of the scintillator are either ionised or excited to emit photons in the visible or ultraviolet range. In general, the excitation process, and the subsequent emission of a photon, can proceed in different ways. In the *fluorescence* (blue arrows), the charged particles excite an electron of a singlet state S_i. This excited electron immediately falls back into the ground state S_0. During this prompt decay (decay time of the fluorescence $\sim 10^{-9}$ - 10^{-5} s [64]) a photon is emitted. The *phosphorescence* (green arrows), on the other hand, is delayed (decay time of the phosphorescence $\sim 10^{-5}$ - 10^{-3} s [64]). Through the recombination of ionised molecules, excited triplet states can be formed. However, due to the selection rules for electronic transitions between two states of bound systems, the transition of an excited triplet state T_i to the ground state S_0 is not allowed. By 'intersystem crossing' (the radiationless transition from an electronic excited state to another excited state with changed multiplicity), the transition $T_i \rightarrow S_i \rightarrow S_0$ occurs nevertheless, but with a longer decay time than in the case of prompt fluorescence. In addition, the combination of two excited triplet states leads to the occupation of two (equally excited) singlet states, which emit delayed photons when de-exciting to the ground state. The energy spacing between the ground state S_0 and the first excited singlet state S_1 is ~ 3 - $4\,\mathrm{eV}$, whereas the spacing usually decreases for higher-lying states. Each of these electronic configurations is further divided into a finestucture, originating from vibrational excitations of the molecule. Typical energy spacing of these levels is around $\sim 0.15\,\mathrm{eV}$.

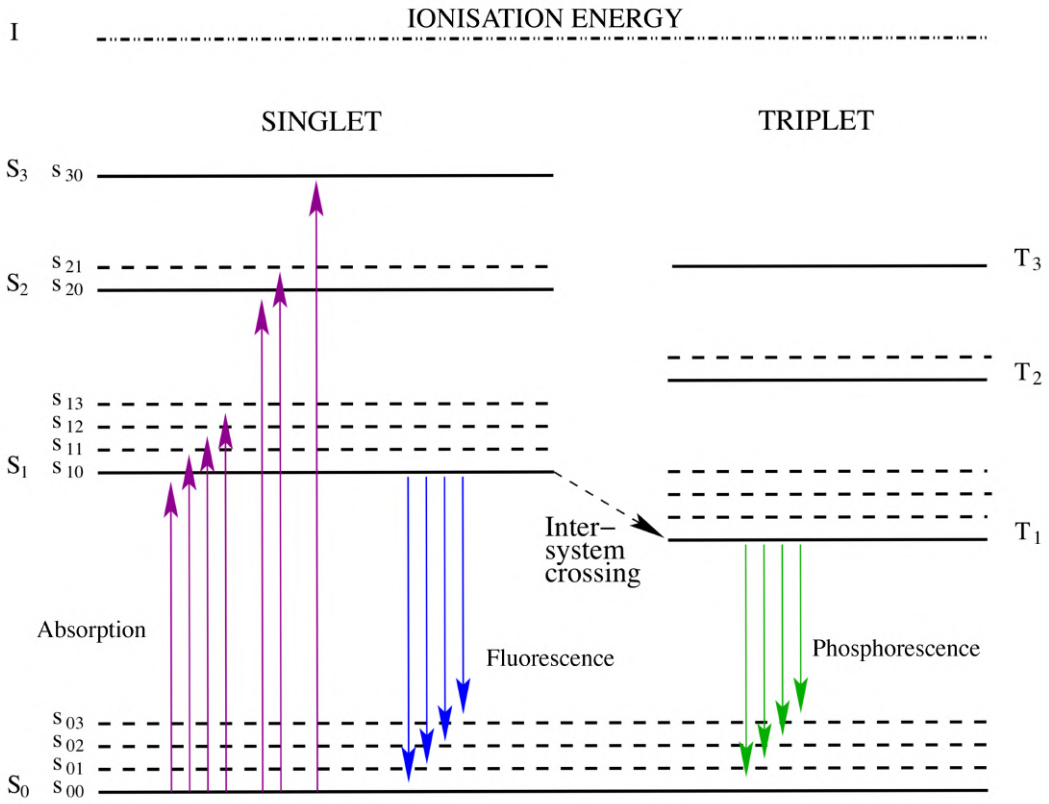

Figure 3.2.: *Energy levels of a typical π-orbital with singlet (S_0, S_1...) and triplet (T_1, T_2...) states. Induced by the electromagnetic interaction of the hydrocarbon with a charged particle, energy absorption leads to an excitation and subsequently to prompt fluorescence. The excitation of the triplet states leads to delayed phosphorescence either by means of intersystem crossing or by the combination of two triplet states. The fine-structure (S_{00}, S_{01}...) is due to vibrational excitations. Figure adapted from [49].*

Organic Plastic Scintillators

Scintillating materials, in which the primary fluorescent emitter, the so called fluor, is suspended in a solid polymer matrix, the so called base, are referred to as plastic scintillators. Common bases of organic plastic scintillators are aromatic plastics, which are polymers with out-branching aromatic rings. Due to its aromatic component, already the base polymer itself does fluoresce in the presence of ionizing radiation. However, the addition of fluors is necessary in the construction of practical scintillators, because the base polymer has a low yield and a negligible transparency to its own emission wavelength. [65]. Among the variety of different bases, polystyrene and polyvinyltoluene are the most widely used ones. Their chemical structure can be seen in Figure 3.3. In addition, common wavelength shifters such as POPOP, PPO or PTP[1], are soluted with typical concentrations of a few grams per liter of solvent and emit light at a specific wavelength. These are, on top of the primary fluorescent emitter, indispensable for the functioning of the plastic scintillator because they allow the adjustment and customization of the emission spectrum such that it can be optimized with respect to the absorption spectrum of the plastic. As the fluorescence process in organic

[1]The accurate names of POPOP, PPO and PTP are 1,4-Bis-(5-phenyloxazol-2-yl)-benzol), (2,5-diphenyloxazol) and 1,4-diphenylbenzol, respectively.

materials arises from transitions in the energy level structure of a specific molecular species, it can be observed independently of the physical state of the medium. A solvent, consisting of a monomer with a suitable organic scintillator dissolved, can therefore be polymerized to form a solid plastic, without degrading the initial scintillating properties of the solution. Because of the available fabrication methods of plastics, which allow to easily shape and customize them, plastic scintillators became an extremely useful and widely used form of organic scintillator.

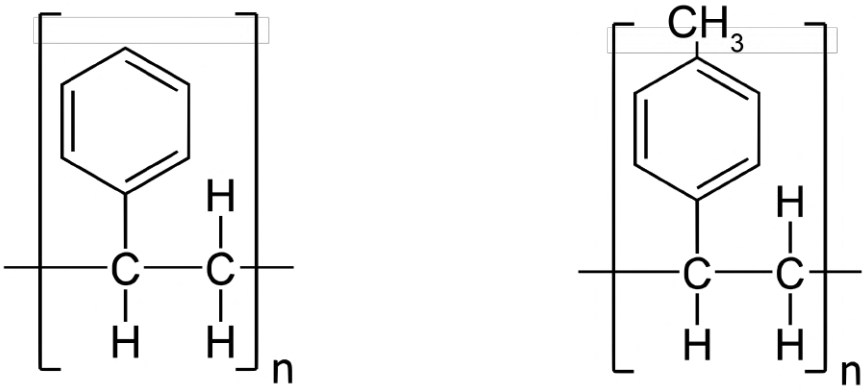

Polystyrene *Polyvinyltoluene*

Figure 3.3.: *Structural formula of the two polymers polystyrene and polyvinyltoluene, which are (among others) commonly used as base materials for organic plastic scintillators. The polymers shown here were chosen due to their importance within the frame of this work. Both materials are synthetic polymers of (alkyl-)benzenes, and are therefore fluorescing in the presence of ionizing radiation. However, fluors need to be added for the construction of practical scintillators. An important difference in the chemical structure between polystyrene and polyvinyltoluene is the functional methyl group, branching out the benzene-ring of polyvinyltoluene, altering the electronic and vibrational states.*

Wavelength Shifting Fibers

For instance, there exists a large offer of plastic scintillators in the shape of small-diameter fibers, both with squared and round cross-sections. These fibers are composed of a scintillating core, which is doped with a fluor, and a thin, surrounding cladding layer, consisting of a material with a lower index of refraction compared to the core. This configuration, which can be seen in Figure 3.4, causes total reflection of all the light rays arriving at the core-cladding interface with an angle of incidence greater than the critical angle for total internal reflection. The addition of so called wavelength shifters, i.e. fluors whose emission peak is shifted with respect to their absorption peak, can be a suitable option for applications in which the spectrum of initially emitted light needs to be adjusted. Due to the high flexibility and adaptability of those wavelength shifting fibers, they are commonly instrumented in systems where the scintillation light of a larger-scale plastic scintillator needs to be collected and guided to a detector [66].

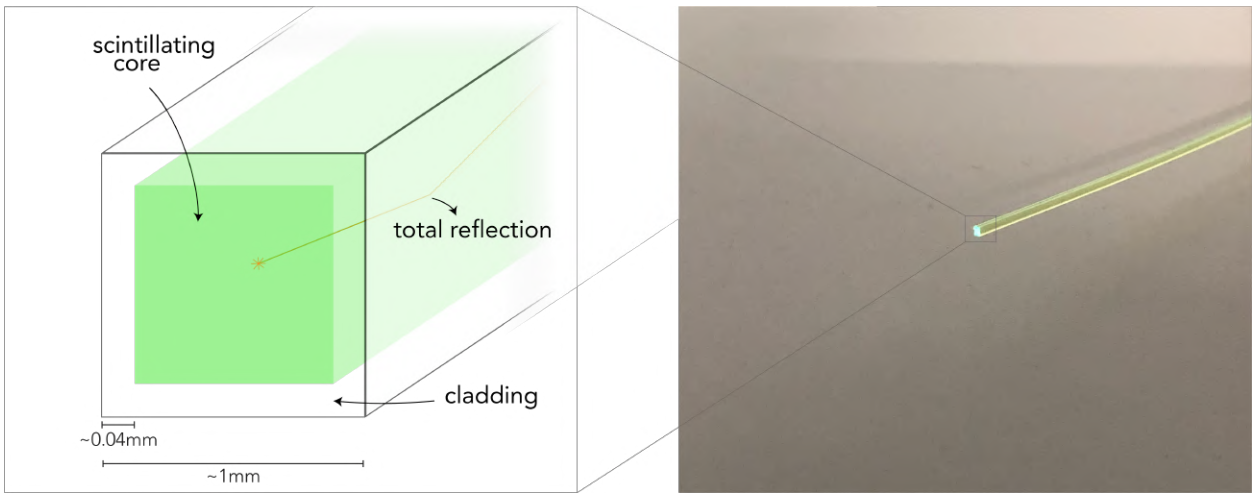

Figure 3.4.: *Cross-section of a typical wavelength shifting fiber. The fiber consists of a scintillating core, surrounded by a thin layer of cladding material. In order to increase the light yield, multiple layers of cladding can be attached. Due to the difference in refractive index between the core and the cladding, total reflection appears at the interface for all light rays arriving with an angle of incidence greater than the critical angle for total internal reflection. The fibers shown exemplary in the picture on the right are the BCF-91A, manufactured by Saint Gobain [67]. They have a squared cross-section, with a total width of 1 mm and a cladding layer thickness of ∼ 0.04 mm. The core, in this case, is based on polystyrene (with an index of refraction of n = 1.6), whereas the cladding is made out of acrylic (with an index of refraction of n = 1.49).*

3.3.2. Working Mechanism of Semiconductor Detectors

Silicon Photomultipliers (SiPMs) are solid-state single-photon-sensitive devices, based on Single-Photon Avalanche Diodes (SPAD) implemented on semiconducting silicon substrate. SiPMs provide the ability to detect single photons with a high gain of the order of 10^5 - 10^6.

Semiconductor Physics

Band gap Silicon is a semiconducting, mono-crystalline material with a diamond lattice structure, which can be seen in Figure 3.5. Semiconducting materials distinguish themselves by their crystalline structure and provide, compared to amorphous materials, a long-range high ordered symmetry. Their electrical conductivity ranges between that of conductors and that of insulators.[2] The so called band model is used to describe energy levels that electrons of a solid may occupy, together with the ranges of energy where no electronic states can exist. In graphs of the electronic band structure of semiconductors (such as shown in Figure 3.5 for silicon) the highest fully occupied band is called the valence band and the first empty band above is called the conduction band. The Fermi level E_F denotes the highest energy level an electron can attain at the temperature of absolute zero. All lower levels are then fully occupied. The band gap generally refers to the energy difference between the top of the valence band (denoted by E_V) and the bottom of the conduction band

[2] Typical metals have a specific electrical resistance of $10^{-7}\,\Omega m$ to $10^{-8}\,\Omega m$, whereas typical insulators range from $10^{-4}\,\Omega m$ to $10^{7}\,\Omega m$. [68]

(denoted by E_C), and the width of this gap $E_g = E_C - E_V$ refers to the energy required to promote a bound valence electron to become a free-moving conduction electron. This energy is dependent on several external and intrinsic parameters such as the temperature or the lattice constant, and it determines many properties of semiconductors such as their electrical conductivity and their optical absorption. For instance, semiconducting materials feature an intermediate-sized but non-zero band gap that behaves as an insulator at absolute zero, but allows thermal excitation of electrons into the conduction band at higher temperatures. The theory describing electronic energy band structures is based on the assumption that electrons, occupying a given quantum state, can be represented by a quantum mechanical wave function, which is characteristic of this state. The energy levels corresponding to the various quantum states (and by that the energies of the bands and the band gaps) can be derived by solving the Schrödinger equation for a periodic solid state lattice potential, which is given rise to by the atomic structure of mono-crystalline materials [69].

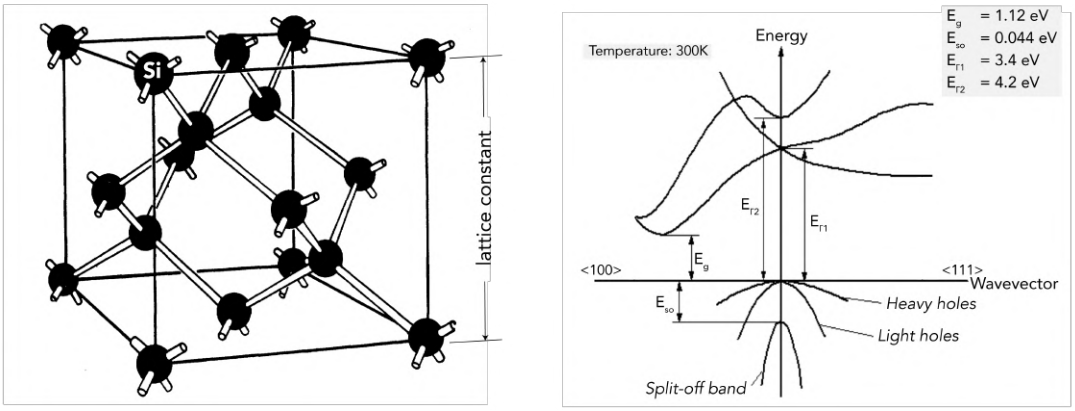

Lattice Structure of Silicon *Electronic Band Structure of Silicon*

Figure 3.5.: *Lattice structure (left) and electronic band structure (right) of silicon. Silicon features a face-centred-cubic lattice with a basis of two identical atoms and a lattice constant of 5.431 Å. The electronic band structure is shown as a function of the wavevector. Special high-symmetry points of the primitive cell in the reciprocal space are denoted by Γ_i. It can be observed that the maximum of the valence band and the minimum of the conduction band are positioned at different values of the wavevector - the resulting band gap is called "indirect". Therefore, it is not possible for an electron to shift from the highest-energy state in the valence band to the lowest-energy state in the conduction band without changing its momentum - the involvement of a phonon is required. The energy of the band gap E_g is 1.12 eV. Figures taken from [70] [71].*

Doping The generation of defects, induced by doping, can drastically change the electrical, optical and structural properties of the starting material and by that adapt it to technical requirements [68]. The intentional insertion of impurities introduces new allowed energy states within the band gap. The energy difference between these introduced energy states and the nearest previous energy band, however, is so small that already at room temperature practically all of the dopant atoms can be thermally ionized and release free charge carriers in the conduction or valence bands. Two different types of doped semiconductors can be produced, depending on the impurities with which the semiconductor is doped. Silicon atoms, for instance, feature four valence electrons. In *n-type* semiconductors, the substitution of silicon atoms with a pentavalent element (donor), such as phosphor, leads to the creation of free negative charge carriers, which are available for the conduction band. In

p-type semiconductors, the substitution of silicon atoms with a trivalent element (acceptor), such as boron, leads to the creation of free positive charge carriers (so called holes), which are available for the valence band.

p-n Junction At the interface between the two above mentioned types of semiconducting materials, p-type and n-type, a so called p-n junction is formed. Figure 3.6 shows the energy levels of semiconductors before and after the formation of such a p-n junction. The abrupt change in impurity concentration at the interface triggers a mechanism to compensate for the imbalance in charge concentration across the junction. In fact it can be observed that the Fermi levels of the two respective sides of the interface are automatically equalized. This happens through the diffusion of charged carriers from the area of high to low charge concentration, i.e. that the electrons diffuse from the n- to the p-semiconductor, whereas the holes diffuse in reverse direction. Positive and negative charge carriers, moving in opposite directions, recombine and neutralize each other. By that, a central region, devoid of any mobile electrical charges, which is generally referred to as depletion region, is formed. The ionized donors and acceptors however, which are immobile, are counteracting the diffusion process by the formation of an electric field. The potential difference between the two sides of the interface, however, is only around 0.7 V. An electrical field high enough for electrons to overcome the potential barrier and traverse the junction, and by that constitute a measurable current, can be established by applying a reverse bias[3]. The p-n junction becomes conductive and can be instrumented as a useful tool in radiation detection, e.g. in high purity germanium (HPGe) detectors.

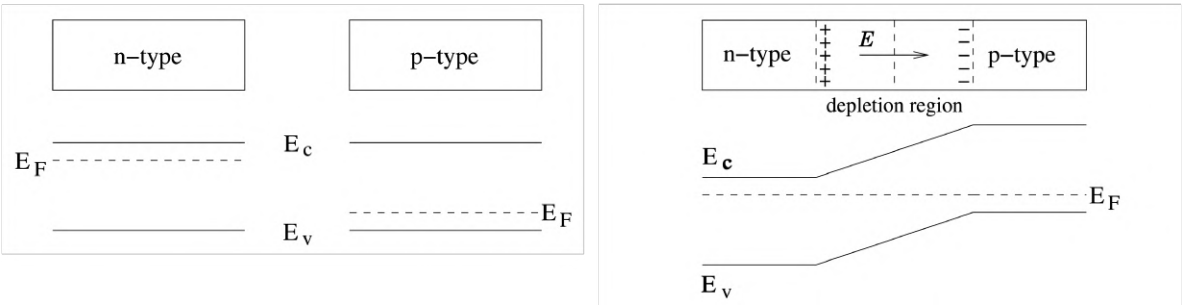

Separate p- and n-type semiconductors *Formation of p-n junction*

Figure 3.6.: *Semiconductors and their energy levels, before (left) and after (right) the formation of a p-n junction in thermal equilibrium with zero-bias voltage applied. When p- and n-type semiconductors are brought into contact, diffusion of charge carriers takes place until the Fermi levels of the two respective sides are equalized. A central depletion region, devoid of mobile electrical charges, is formed. Immobile ionized donors and acceptors are building up an electric field E across the depletion region, opposing the diffusion process. Figures taken from [72].*

Structure of Silicon Photomultipliers

Avalanche Photo-Diode A photo-diode is essentially a p-n junction operated in reverse bias mode. Consequently, the depletion layer is enlarged and the potential barrier is

[3]The device is referred to as reverse biased if a negative voltage is applied to the p-type region relative to the n-type region.

increased, thus acting essentially as an insulator. The absorption of incident radiation by the depletion layer creates electron-hole pairs via the photoelectric effect. Under the influence of the effective junction electric field the created charge pairs move in opposite directions, and by that constitute a measurable electric current. In an Avalanche Photo-Diode (APD) the external bias voltage is high enough to establish an electric field sufficiently strong to trigger an avalanche of charge carriers by impact ionization. The bias point, at which the avalanche process gets triggered, is denoted as the breakdown voltage. The output signal of an APD and its dynamic range depend upon several intrinsic parameters such as the effective electric field strength, the capacitance or the width of the depletion layer. For instance, thin depletion layers lead to fast signals, whereas thick depletion layers increase the efficiency of the diode.

Working principle of Silicon Photomultipliers The internal structure of typical SiPMs, which can be seen in Figure 3.7, is usually composed of an array of several hundred up to several tens of thousands square-shaped avalanche photo-diodes, with widths of the order of $10\,\mu m$. The total number of photo-diodes and their respective size determines the total active area of the SiPM, which is usually of the order of $1\,\mathrm{mm}^2$. The single photo-diodes are connected in parallel to one common cathode input and one common anode output. The resulting SiPM signal is therefore a superposition of the multiple signals of the single photo-diodes. The APDs are operated well above their reverse-bias breakdown voltage, in the so called *Geiger-Mode*. In this operating state, both electrons and holes are involved in the ionization process, which leads to the fact that the process of avalanche ionization is self-sustainable and can already be triggered by single photons. That furthermore implies that the APDs do not turn off by themselves and the gain is in theory infinite, wherefore a quenching mechanism is necessary to stop the avalanche. Practically, this quenching is achieved by a polysilicon resistor supported by the photo-diodes' capacitance. The operation of SiPM's in the Geiger regime offers a very high signal-to-noise ratio.

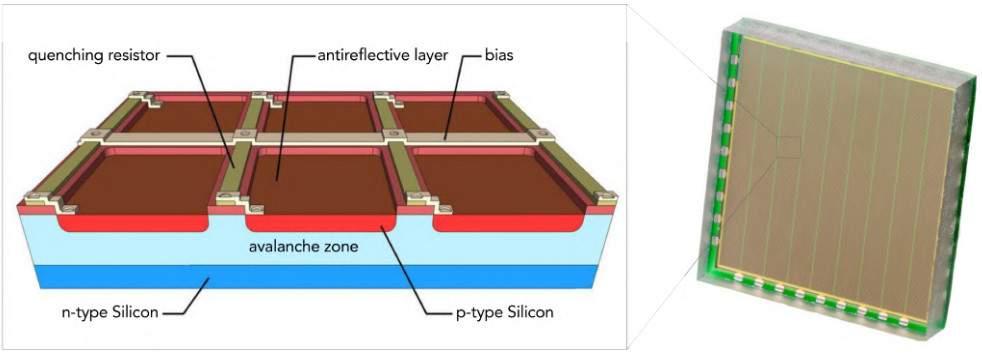

Figure 3.7.: *Schematic, cross-sectional view of a SiPM with 6 single avalanche photo-diodes. The SiPM consists of separated shallow, highly p-doped regions (red) on top of a shared, low n-doped common silicon body (dark blue). The p-type silicon is coated with a thin antireflective layer (brown), which avoids any reflection light losses and therefore leads to a very high sensitivity on the single-photon level. Electrons, which are created via the photoelectric effect, are accelerated across the avalanche zone (light blue), which essentially denotes the depletion zone of the p-n junction. A quenching resistor (olive), which consists of a doped polysilicon strip line embedded in an insulating matrix, is used to limit and control the gain. The single photo-diodes are operated in parallel to the bias (beige). The active SiPM shown exemplary in the picture on the right is the PM3325-WB, manufactured by KETEK [73].*

Characteristics of Silicon Photomultipliers

Gain The gain G of a SiPM is defined as the amount of charge created for each detected photon and depends as such on the overvoltage and the size of the photo-diode. Every time an ionization avalanche is triggered upon the absorption of a photon in the active volume a highly uniform and quantized amount of charge is generated. The gain is defined as the ratio of the output charge of an activated photo-diode to the unit charge and can thus be calculated from the overvoltage V_{OV}, the photo-diodes' capacitance C and the electron charge q:

$$G = \frac{C \cdot V_{OV}}{q} \tag{3.1}$$

Pulse shape The single photon signal of a photo-diode is asymmetric with a very fast rise time below 1 ns and a recovery time limited by the quenching resistor and the intrinsic capacitance of the photo-diode to a value around ~ 45 ns. The first component of the signal, the signal rise component, corresponds to the discharge of the photo-diode, which is determined by the rise time of the triggered avalanche formation and by the variation in the transit times of signals arriving from different points on the sensors' active area. The cell recovery takes place in two steps. The fast signal recovery component provides a fast spike due to the rapid charge supply of the quenching resistor, which serves as parasitic capacitance. The slow signal recovery component corresponds to the recharge of the photo-diode through the quenching resistor. Figure 3.8 shows the typical single-photon pulse shape of a KETEK PM3325-WB SiPM when illuminating it with a short laser pulse (< 1 ns) [73].

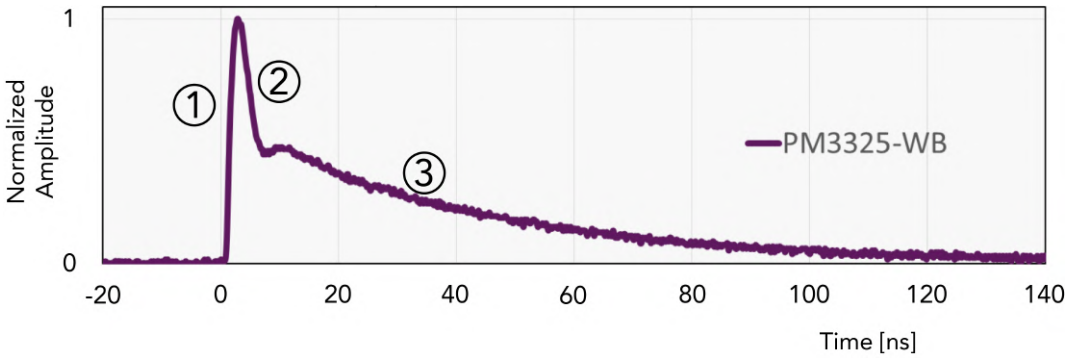

Figure 3.8.: *Typical single-photon pulse shape of a KETEK PM3325-WB SiPM at room temperature when illuminating it with a short laser pulse (< 1 ns). The signal rise component (1) corresponds to the discharge of the photo-diode and is very rapid. The fast signal recovery component (2) features an exponential decay time of $\tau_{decay,fast} = 5.2$ ns and corresponds to the rapid charge supply of the quenching resistor. The slow signal recovery component (3) features an exponential decay time of $\tau_{decay,slow} = 40$ ns and corresponds to the recharge of the photo-diode. Figure adapted from [73].*

Breakdown voltage The breakdown voltage V_{BR} is the bias voltage point at which the electric field strength generated in the depletion region of the SiPM is strong enough to sustain an avalanche ionization. The former electrical insulating material is subjected to a high enough voltage and suddenly becomes an electrical conductor. Accordingly, this breakdown is expressed in a sudden increase in the current flow. Another relevant quantity is the so called operation voltage V_{Bias}, which refers to the actual voltage at which the SiPM is being operated. Due to the definition of the breakdown-voltage, at which both

the detection efficiency and the gain are still zero, it is necessary to operate the SiPM at a voltage that is 10 % to 25 % higher than the breakdown voltage itself [74]. The difference between breakdown voltage and operation voltage is referred to as overvoltage V_{OV}.

Dark counts The breakdown of the p-n junction of a photo-diode can also occur when the SiPM is operated under dark conditions. The resulting signals, which are called dark counts, are due to thermally generated electrons that trigger an avalanche in the depletion region. The signals resulting from the breakdown of the photo-diode are identical, no matter if they are due to photon-generated or thermally-generated electrons. For this reason, dark counts represent the primary source of noise in a SiPM. The high rate of dark counts can be used for a simple and fast calibration and for monitoring the stability of the SiPM during operation.

After-pulse rate Afterpulses are pulse signals that can be observed after the initial photon-generated pulse signal with a delay time τ_{AP} that can range from a few ns to several μs. Lattice defects in the silicon can cause additional energy states, which can be occupied by charge carriers for a certain amount of time during the breakdown. As soon as the trapped charge carriers are released again, they can potentially initiate a delayed avalanche in the same photo-diode. Afterpulses that occur during the recovery time of the photo-diode with only a short delay tend to have a negligible impact as the photo-diode is not fully charged. However, afterpulses with a longer delay can strongly impact the measurements if the rate is high [74].

Optical crosstalk During the avalanche ionization process, accelerated charge carriers in the high field region can emit photons. Typically, $2.9 \cdot 10^{-5}$ photons are emitted per electron crossing the junction and can be reabsorbed by silicon [75]. Those photons can initiate a secondary avalanche in a neighboring photo-diode, leading to an additional component of SiPM noise. This phenomenon is denoted as optical crosstalk. As these secondary photons are usually located in the near infra-red range, they can travel considerable distances through the silicon. Although the individual photo-diodes are separated from each other, secondary photons can travel to adjacent photo-diodes via reflection from the window material on the top of the sensor or from the bottom of the silicon substrate. Optical crosstalk is a function of the overvoltage V_{OV}, because the number of the emitted photons is linearly proportional to V_{OV}. It furthermore depends on the exact geometry of the photo-diode.

4. Efficiency Study of the NUCLEUS Cryogenic Muon Veto

Contents

4.1. Methodology of the Geometrical Simulations

4.1.1. Scope of the Study

The geometric simulation framework presented hereafter has been developed mainly in the framework of the work on the *Outer Muon Veto*, conducted at the *Centre CEA de Saclay*. The efforts were initiated by V. Wagner; responsible for the implementation of the simulation algorithm was V. Savu, in collaboration with the author of this thesis. The focus in this thesis is on the impact of the *Cryogenic Muon Veto* on the overall NUCLEUS muon veto performance. A comprehensive description of the simulations and the entirety of their results can be found in [58].

The main goal of the geometrical simulation framework is the evaluation of the muon-tagging capability of the NUCLEUS muon veto and the exploration of the impact of different geometrical configurations on its overall performance. To this end, purely geometrical studies were performed, in the sense that the generated muons travel in straight lines throughout the complete simulation process. The key parameter, which can be retrieved from this simulation concept is the efficiency of the NUCLEUS muon veto. As no experimental information of this value is accessible during the R&D process, track simulations provide a suitable tool for an approximative estimation. They also draw attention to gaps in the overall arrangement that lead to a loss of efficiency. The distribution of tagged muons over the experimental arrangement obtained from the simulations can be used via a normalization, to get information on the expected count rate of cosmic muons. A subsequent consideration of the initial muon

energy spectrum and the computation of the resulting energy loss in the NUCLEUS muon veto materials, which can be applied on the simulated muon vertices, yields the number of stopping muons within the experimental setup.

The geometrical study was based on Monte Carlo simulations implemented in ROOT [76], without taking physical interactions into account. The TGeometry package [77] was used for building, navigating and visualizing the detector geometries. The package runs standalone with respect to any tracking Monte Carlo engine and is therefore not restricted to physics.

4.1.2. Geometry Implementation

The geometry was modeled according to up-to-date[1] technical drawings of the individual NUCLEUS components. A list, summarizing information regarding the shape and the exact dimensions of the NUCLEUS shielding components and their composing volumes, which were considered for the muon tracking simulations, can be found in Table A.1 in the Appendix. Depending on the information addressed in each simulation, different geometrical arrangements and settings were compiled. The default arrangement, which can be seen in Figure 4.1, is composed of 6 different sides arranged as a cube, with each individual side in turn consisting of 4 individual panels. The total of 16 panels, which are attached to the front, rear, left and right side of the experiment, feature a cuboidal shape, whereas the eight panels on the top and the bottom side have a trapezoidal shape. The position of the *Cryogenic Muon Veto* in the default arrangement is indicated as continuation of the top side of the outer veto, and as such positioned at the same level. In addition, the passive shielding consisting of lead and polyethylene was implemented. Both the outer component, which encapsulates the cryostat, and the inner component, which sits inside the cryostat, were considered. The passive shielding is especially relevant for the computation of the muon energy deposition, which will be discussed later on.

[1] The results presented here are based on the current dimensions at the time of the simulations in October 2020.

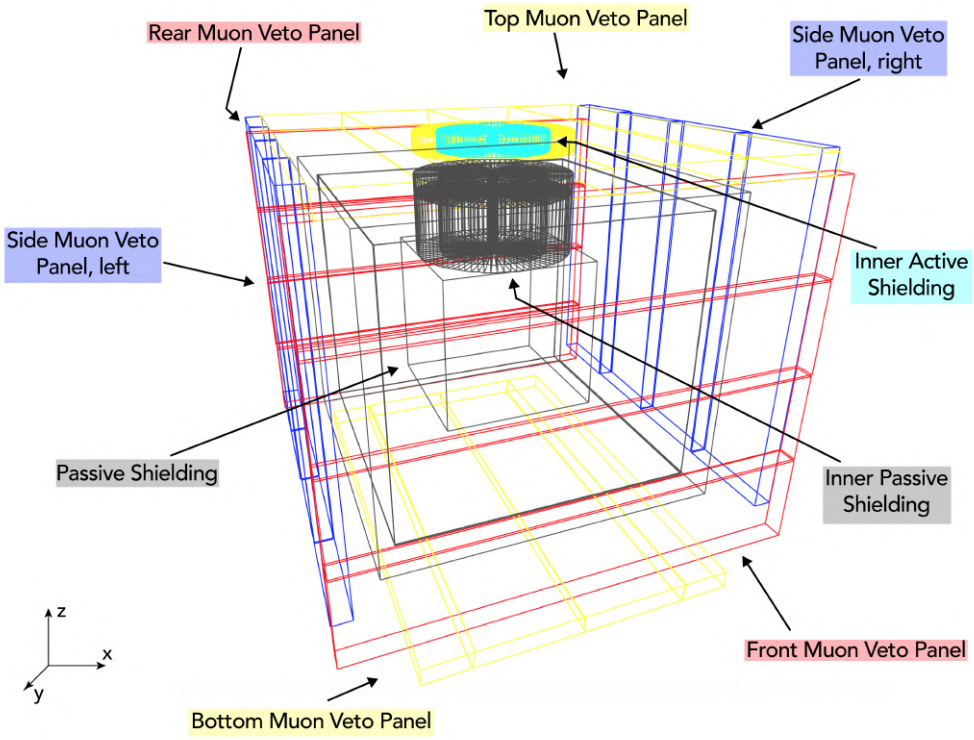

Figure 4.1.: *NUCLEUS default geometry, implemented using TGeometry for the muon track simulations. The scheme labels the individual NUCLEUS shielding components, which were considered for the simulations. The implemented geometrical arrangement consists of 6 individual sides composed of 4 panels each, overall arranged in a cuboidal manner. The respective sides are coloured in blue (left and right side), in red (front and rear side) and in yellow (top and bottom side). The inner active shielding (i.e. the Cryogenic Muon Veto), shown in turquoise, is positioned on the same level as the top panel. The outer and inner components of the passive shielding are shown in grey. The implementation of the passive shielding is a simplified version of the real design, since any subdivisions have not been taken into account. The coordinate system shown in this scheme indicates the norm, according to which the dimensions listed in the Appendix are specified.*

4.1.3. Simulation Algorithm

Muon Tracking Simulations

The underlying idea of the muon track generator used in this work is based on the framework *Choozerent* previously implemented by the NUCLEUS collaboration using Geant4 libraries [44]. It consists of an energy-independent particle generator that shoots particles from random positions on a plane tangent to a demi-sphere of specified radius. This demi-sphere, as shown in Figure 4.2, is centred with respect to the implemented geometry. The particles are shot in the direction perpendicular to the plane on which they are generated, such that the whole volume of the muon veto is populated by muons of a given directionality defined by the (θ,φ) angles[2]. The position of this plane with respect to the demi-sphere follows in

[2] A spherical coordinate system, in which θ denotes the polar angle and φ denotes the azimuthal angle is used.

the θ-plane the characteristic angular $\cos^2\theta$ distribution of atmospheric muons, with θ corresponding to the angle of incidence of the muons and in the φ-plane a uniform distribution. The resulting directionality of muons can be seen in Figure 4.3. The implemented procedure allows to mimic a realistic directionality of the impinging muons.

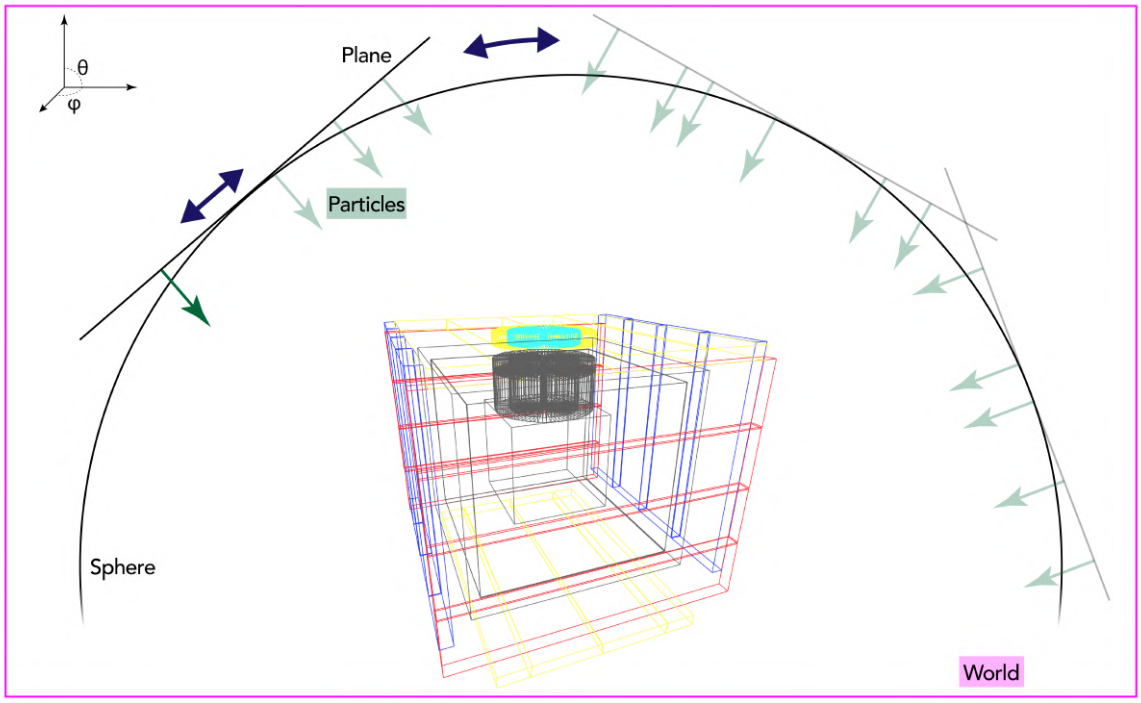

Figure 4.2.: *Working principle of the muon track generator, implemented for the muon track simulations shown here in a simplified 2D scheme. Particles (green) are generated on random positions of a plane, which is attached tangentially to a sphere. The position of the plane with respect to the sphere follows a characteristic angular $\cos^2\theta$ distribution. The resulting directionality of the impinging particles mimics a realistic distribution of atmospheric muons. The blue arrows indicate the shift of the particle generation point, both randomly with respect to the plane and $\cos^2\theta$-distributed with respect to the sphere.*

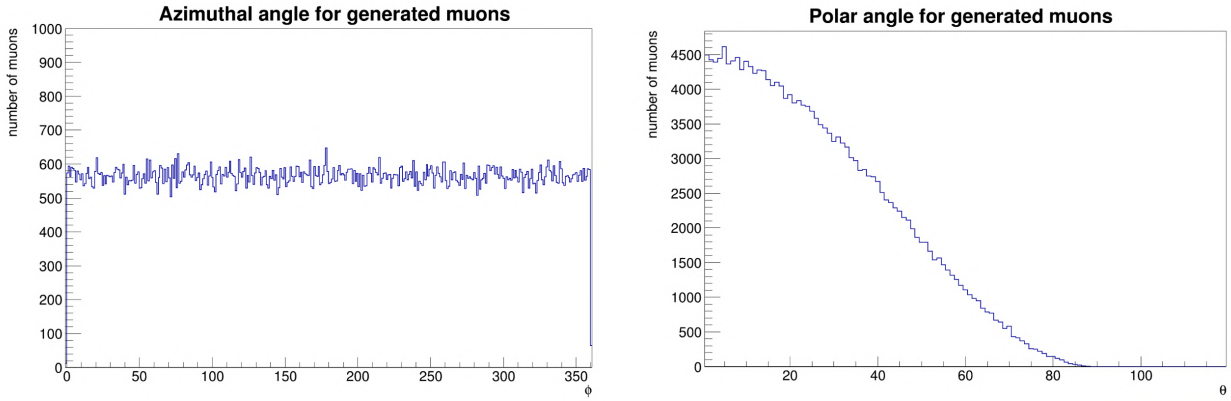

Figure 4.3.: *Azimuthal (φ) and polar (θ) angle distributions of the generated muons. The generated muons are $\cos^2\theta$ distributed in the θ-plane and uniformely distributed in the φ-plane.*

The idea of the muon tracking simulations consists in generating particles and propagating them through the implemented geometry. For the muon tracking simulation this procedure is technically implemented as follows:

- In a first step, the geometry is constructed using the TGeometry package. This leads to a geometrical setup of individual positioned volumes with assigned properties.
- Afterwards, a certain number of events is initialized according to the distribution provided by the track generator. The different results presented in the following are each based on runs with $2 \cdot 10^6$ simulated events.
- Subsequently, each single particle (i.e. each single event) is propagated through the world via steps. As a separate ID is provided for each generated particle, it remains distinguishable from other events. The state of each event (i.e. the material it is currently in and the distance between the current position of the muon and the boundary of the next volume) is examined and stored after every step.

The accumulated information of the propagating particle is stored event by event as so called *tracks*. In addition, information about the media traversed by the muon tracks is recorded. The multiplicity, i.e. the number of times a certain medium was traversed, thus allows to get information about particles detected several times by different plastic scintillator volumes. The track length, i.e. the distance a particle travels in a given medium, is relevant for subsequent considerations regarding the computation of the energy deposition.

Energy Loss Computation

In order to calculate the muons' kinetic energy deposition, a realistic energy spectrum needs to be assigned to the muon distribution, attributing a specific energy to each event. This assignment was based on two different sources: an experimental determination of the absolute flux of atmospheric muons in the momentum range 0.6 – 400 GeV/c performed by the BESS-TeV Spectrometer [78] and a theoretically modeled energy distribution of atmospheric muons at the Earth [79]. The fit function specified therein for the energy distribution of atmospheric muons follows a power law E^{-n}, which is modified in the low and high energy region:

$$\phi(E) = \phi_0 N (E_0 + E)^{-n} (1 + \frac{E}{\epsilon})^{-1} \tag{4.1}$$

In this equation, ϕ_0 denotes the vertical muon flux integrated over energy, N denotes a normalization factor, E_0 denotes a parameter accounting for an energy loss due to both the hadronic as well as the electromagnetic interactions with air molecules of the atmosphere and ϵ denotes another parameter correcting for effects such as the finite life time of pions and kaons.

With the known information about the kinetic energy and the individual track lengths of each event, it is now possible to compute the deposited energy in every volume. The computation is done via the Bethe-Bloch formula for relativistic charged particles, which is implemented as follows [80]:

$$-\langle \frac{dE}{dx} \rangle = K z^2 \frac{Z}{A} \frac{1}{\beta^2} [\frac{1}{2} ln \frac{2 m_e c^2 \beta^2 \gamma^2 T_{max}}{I^2} - \beta^2] \tag{4.2}$$

In this equation (which describes the mean rate of energy loss in the region $0.1 < \sim \beta\gamma < \sim 1000$ for intermediate-Z materials) z is the charge of the incident particle, β is the velocity of the incident particle, Z is the charge number of the medium, A is the atomic mass of the medium and I is the mean excitation energy of the medium. T_{max} denotes the maximum energy transfer in a single collision and $K = 4\pi N_A r_e^2 m_e c^2$ corresponds to a normalization factor, aggregating constant parameters such as the Avogadro's number, the classical electron radius and the mass of the electron. In order to obtain the linear stopping power in units of $MeV\,cm^{-1}$ one has to multiply equation 4.2 by the density of the medium in which the energy of the particle is deposited. The material properties of the three implemented materials (lead and polyethylene for the passive shielding and polyvinyltoluene for the plastic scintillator panels), which have been included in the simulations presented here, are summarized in Table 4.1.

Table 4.1.: *Relevant material properties [81, 82], which are required as input for the Bethe-Bloch formula to compute the mean rate of energy loss of muons traversing the respective materials. The passive shielding is composed of lead and polyethylene, whereas the plastic scintillator panels are composed of polyvinyltoluene.*

Atomic Composition	**Z / A**	**Density** $[\frac{g}{cm^3}]$	**Refractive Index**	**Excitation Energy** $[eV]$
Absorber-Type Lead				
Pb	82 / 207.2	11.35	1.0	818.82
Absorber-Type Polyethylene				
$[C_2H_4]_n$	5.28 / 10.43	0.92	1.5	62.10
Absorber-Type Polyvinyltoluene				
$[CH_CH(C_6H_4CH_3)]_n$	5.58 / 11.08	1.023	1.58	70.94

4.1.4. Accessible Observables from the Geometrical Simulations

Geometric Efficiency Estimation

After all propagated events of the muon tracking simulations have been tracked and stored, the efficiency computation of the NUCLEUS muon veto can be conducted. An efficiency ε, which refers exclusively to physical components of the experimental setup, was defined. As such, the chosen efficiency definition provides a measure of the number of muons that pass through the lead and are not detected by plastic scintillator volumes:

$$\varepsilon = \frac{\text{particles hitting plastic scintillator volumes AND lead}}{\text{particles hitting lead}} \tag{4.3}$$

This efficiency definition takes into account that the relevant and potentially harmful muons for the NUCLEUS data acquisition are especially those that pass through the lead components of the passive shielding.

Realistic Efficiency Estimation and Discrimination Threshold

On the basis of the computation of the energy deposition it is furthermore possible to specify the efficiency in a realistic manner, taking into account the energy deposition of the muons inside the plastic scintillator volumes - it is in this sense denoted as $\varepsilon_{realistic}$. Alternatively, the efficiency can be defined in a solely geometrical manner via the muon vertices - it is in this sense denoted as $\varepsilon_{geometric}$. The efficiency $\varepsilon_{realistic}$ is expected to slightly decrease upon consideration of the deposited energy, since muons stopping before being detected by the muon veto are eluding detection. This effect is neglected in the efficiency $\varepsilon_{geometric}$, based purely on the muon veto tracks.

Apart from muons, also gammas originating from environmental natural radioactivity are registered by the plastic scintillator panels. It was previously pointed out that a simple energy cut allows a discrimination between gammas and muons, thus minimizing the rate of tagged background events. Given the approximate energy deposition of muons of $\sim 2\,\mathrm{MeV}\,/\,\mathrm{cm}$ in the plastic scintillator, imposing a threshold on the muons' track length in at least one of the traversed plastic scintillator volumes allows to mimic the discrimination threshold. In this way it can be assured that the deposited energies of the considered muons are well above the energies of gammas originating from natural radioactivity. In the context of this thesis, a conservative threshold of 2.5 cm was chosen, corresponding to a non-consideration of muons depositing less than 5 MeV. A more detailed justification for this choice of threshold can be found in [58].

Uncertainty on the Efficiency Estimation

In order to get an estimate of the statistical uncertainty on the computed efficiency value, 20 iterations with $2 \cdot 10^6$ simulated events were performed for the NUCLEUS default geometry [58]. From the resulting distributions of $\varepsilon_{geometric}$ and $\varepsilon_{realistic}$ the mean value as well as the standard deviation were determined. Under the assumption, that the efficiency estimators obtained by each execution of the muon track simulations follow a Gaussian distribution centred around the true efficiency value, it was found that there is a 95 % probability that the efficiency estimator, obtained by a single simulation run, is within two standard deviations from the true value. This rough estimate of the uncertainty on the efficiency estimation is merely intended to sufficiently justify the quantitative comparison of different simulations with different geometric arrangements.

Number of Stopping Muons

Muons, which according to the computation via the Bethe-Bloch formula deposit all their kinetic energy within the traversed volumes are considered as *stopping muons*. The stopping muons, especially those which are not tagged by the muon veto upon entering the geometrical arrangement, are of particular relevance, since these muons can potentially induce secondary particles, representing background events originating in the direct vicinity of the NUCLEUS target detector. The various potential decay processes were previously described in Section 2.2. The presence of lead, a high-Z material, in the inside of the muon veto layer as passive shielding component increases the average muon energy loss per traversed distance (see equation 4.2) and thus the probability for muons to stop.

Muon Rate

In order to obtain the muon rate from the purely geometric approach of the muon track simulations, the real time equivalent to the arbitrary time units inherit to the muon track simulations needs to be determined. This normalization is performed using a known reference, namely the expected realistic value for the rate of cosmic muons at the earths' surface (which is assumed to be $\sim 100\,\mathrm{Hz/m^2}$ [80]), and then extrapolated to the translated conditions for the NUCLEUS muon veto using the known attenuation factor of 1.41 (see Section 2.2) of the NUCLEUS experimental site.

The information about the traversed media of the single muon tracks, which is accessible in the muon tracking simulations, allows to retrieve the muon rates in the different implemented components of the shielding. Of particular interest is the overall muon count rate, (denoted as ϕ_{veto}). With additional consideration of the energy deposition, the rate of stopping muons (denoted as ϕ_{stop_μ}) and the rate of non-detected stopping muons (denoted as $\phi_{stop\_\mu\_PS}$) in the respective components can be determined.

4.2. Results of the Geometrical Simulations

4.2.1. MC Simulation of the NUCLEUS Cryogenic Muon Veto

The impact of the hole in the upper side of the muon veto through which the NUCLEUS cryostat will be inserted, and which is to be minimized by the operation of the *Cryogenic Muon Veto*, is subject to the first set of Monte Carlo simulations. In a first step it was investigated how the efficiency and the number of stopping muons are affected when the *Cryogenic Muon Veto* is not installed at all and the inner part of the NUCLEUS experiment is unshielded from vertically impinging cosmic muons. In a second step a possible misalignment of the *Cryogenic Muon Veto* was examined. Between the mixing chamber plate of the NUCLEUS cryostat and the upper edge of the passive shielding there is a gap of 11 cm, within which the plastic scintillator disc could theoretically be shifted. The misalignment of the plastic scintillator disc is schematically shown in Figure 4.4. In this work, the default position is the position in which the disc is positioned directly underneath the mixing chamber, and thus on the same level as the *Outer Muon Veto*. The misalignment determines the possible angle of incidence of the undetected muons, and can thus potentially influence the efficiency and the number of stopping muons. Simulations were carried out in four individual steps, with misalignment values of $z = 0\,\mathrm{cm}$, $z = -2\,\mathrm{cm}$, $z = -4\,\mathrm{cm}$ and $z = -6\,\mathrm{cm}$.

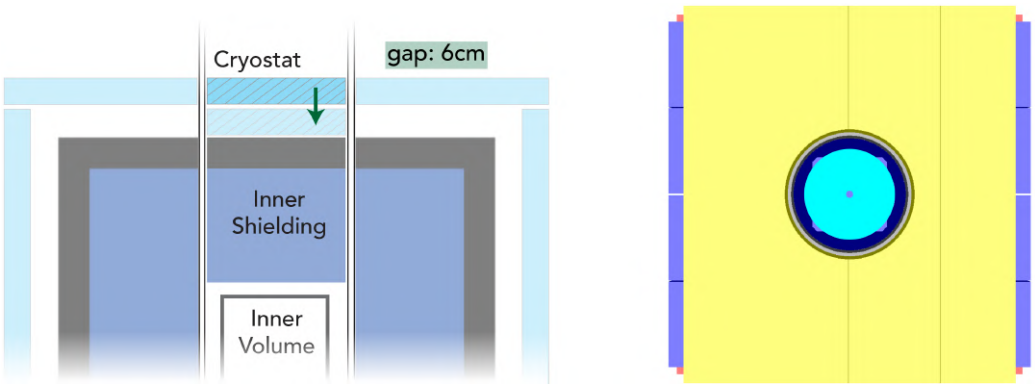

Figure 4.4.: *Schematic, cross-sectional view of the NUCLEUS shielding structure, illustrating the misalignment of the Cryogenic Muon Veto. The envisaged positioning of the plastic scintillator disc inbetween the mixing chamber of the NUCLEUS cryostat and the upper edge of the passive shielding allows a vertical displacement of the disc within a range of 6 cm. In the simulations, the misalignment was carried out in four individual steps, namely z = 0 cm, z = -2 cm, z = -4 cm and z = -6 cm. The top view of the NUCLEUS muon veto geometry, implemented using TGeometry is shown on the right.*

Efficiency Results

The results of the efficiency analysis, taking into account a misalignment of the *Cryogenic Muon Veto* are summarized in Table 4.2. The realistic efficiency $\varepsilon_{realistic}$ with applied track-length threshold of 2.5 cm of the NUCLEUS muon veto can be estimated to 98.34 %, when no *Cryogenic Muon Veto* is installed. The installation of the *Cryogenic Muon Veto* increases the overall efficiency by ∼0.86 % to a value of 99.20 %. The *Cryogenic Muon Veto* thus turns out to be a key component in achieving the targeted muon detection efficiency of >99% of the NUCLEUS muon veto. The misalignment of the plastic scintillator disc, however, does not significantly (<0.05 %) affect the overall efficiency, which allows flexibility in its positioning.

Number of Stopping Muons

The rate of stopping muons is $\phi_{stop\_\mu} = 45.9$ Hz, independent of the *Cryogenic Muon Veto* installation. The corresponding percentage of stopping muons within the implemented geometrical arrangement can be estimated to ∼6.8 % with respect to all impinging muons. Dependencies, however, on the installation of the *Cryogenic Muon Veto* are given for the rate of non-detected stopping muons $\phi_{ND\_stop\_\mu}$, which decreases from 2.68 Hz without the plastic scintillator disc installed to 1.25 Hz after its installation (without misalignment). In other words without the *Cryogenic Muon Veto* installed, around 5.8 % of the total stopping muons are not detected. From these muons ∼55 % are being stopped in lead, whereas ∼42 % are being stopped in polyethylene. After the installation of the *Cryogenic Muon Veto* only ∼2.7 % of the total stopping muons are not detected by plastic scintillator volumes. Of these ∼60% are stopped in lead and ∼37% are stopped in polyethylene. The detailed results of the analysis of stopping muons, based on the energy deposition of the muons inside the plastic scintillator volume with applied track-length threshold of 2.5 cm, together with the respective muon fluxes through the individual NUCLEUS shielding components, are summarized in Table A.2 in Appendix A.

Table 4.2.: *Results of the efficiency estimation for the geometrical arrangements in which no Cryogenic Muon Veto is installed, and in which it is installed and misaligned in four individual steps, namely z = 0 cm, z = -2 cm, z = -4 cm and z = -6 cm. The efficiency ε provides a measure of the number of muons that pass through the lead and are not detected by plastic scintillator volumes. The index "geometric" indicates that the efficiency calculation was based solely on the muon tracks, whereas the index "realistic" indicates that the efficiency calculation takes into account the energy deposition of the muons using the Bethe-Bloch formula. Applying a threshold on the track length allows to mimic a discrimination threshold. The installation of the Cryogenic Muon Veto increases the overall realistic efficiency by roughly 0.86 %.*

	$\varepsilon_{geometric}$	$\varepsilon_{realistic}$ (*no threshold*)	$\varepsilon_{realistic}$ (*2.5 cm*)
No Cryogenic Muon Veto			
	99.07 %	98.58 %	98.34 %
Cryogenic Muon Veto			
z = 0 cm	99.60 %	99.44 %	99.20 %
z = -2 cm	99.61 %	99.44 %	99.21 %
z = -4 cm	99.63 %	99.47 %	99.23 %
z = -6 cm	99.60 %	99.43 %	99.21 %

4.2.2. MC Simulation of an Optional Hollow Cylindrical Muon Veto

The mitigation of the impact of the unavoidable gap, where the vessels of the NUCLEUS cryostat enter the shielding is subject of the second set of Monte Carlo simulations. This circular gap has in reality a width of 6.5 cm and is marked in Figure 4.5 with red ellipses. Muons striking at low angles of incidence can pass undetected through this gap into the interior of the experiment, where large amounts of lead and polyethylene are situated as part of the passive shielding. If those shielding components cause the muons to stop, they can induce secondary particles representing a potentially harmful background for NUCLEUS (see Section 2.2). To minimize the impact of this gap by restricting the range of the angle of incidence at which muons remain undetected, an additional *Hollow Cylindrical Muon Veto* is proposed and studied within the frame of this thesis. The position and the dimensions of this optional component are shown in Figure 4.5. It is supposed to be positioned on top of the *Top Muon Veto Panel* (see Figure 4.1), and encloses the cryostat vessel tightly. It has a proposed thickness of 5 cm. For the height, three different values were examined in the simulations, namely $h = 10$ cm, $h = 20$ cm and $h = 30$ cm. For the default height, $h = 10$ cm, the four misalignment steps of the disc of the *Cryogenic Muon Veto* were included again.

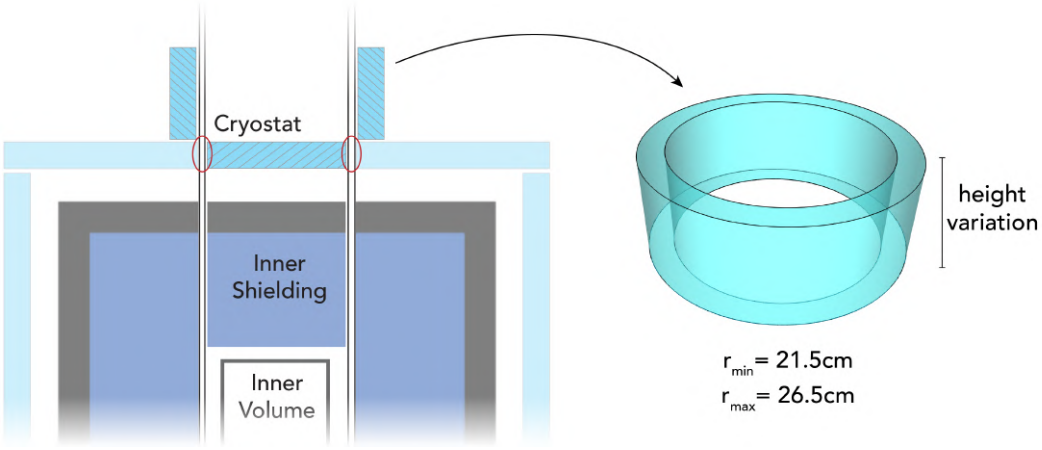

Figure 4.5.: *Schematic, cross-sectional view of the NUCLEUS shielding structure, illustrating the proposed additional Hollow Cylindrical Muon Veto. This optional component sits on top of the Outer Muon Veto and encloses the NUCLEUS cryostat vessel. That configuration allows to minimize the impact of the gap, where the vessels enter the experiment. In the simulation the height was varied from $h = 10\,cm$ to $h = 20\,cm$ and to $h = 30\,cm$.*

Efficiency Results

The results of the efficiency analysis, taking into account the additional operation of a *Hollow Cylindrical Muon Veto*, are summarized in Table 4.3. The realistic efficiency $\varepsilon_{realistic}$ with applied track-length threshold of 2.5 cm of the NUCLEUS muon veto can be estimated to 99.43 %, when an additional *Hollow Cylindrical Muon Veto* with a height of $h = 10$ cm is installed. This corresponds to an efficiency-increase by roughly 0.2 % compared to the default NUCLEUS design. Again, the misalignment of the *Cryogenic Muon Veto* has no significant impact on the overall efficiency. The efficiency can be further increased by another ~ 0.15 % by increasing the height of the *Hollow Cylindrical Muon Veto* to $h = 30$ cm. In summary, the operation of the proposed additional *Hollow Cylindrical Muon Veto* component would increase the overall NUCLEUS muon veto efficiency from 99.20 % (efficiency value for the default geometrical arrangement) to 99.58 % (highest efficiency value achieved in the scope of this study).

Number of Stopping Muons

The rate of stopping muons ϕ_{stop_μ} is not noticeably affected by the additional installation of a component sitting on top of the *Top Muon Veto Panel*, due to the $\cos^2\Theta$-distributed directionality of the muon flux. The simulations predict that for an *Hollow Cylindrical Muon Veto* with $h = 10$ cm the rate of stopping muons ϕ_{stop_μ} is 45.8 Hz, with $h = 20$ cm ϕ_{stop_μ} is 45.9 Hz and with $h = 30$ cm ϕ_{stop_μ} is 46.3 Hz. In this sense, the overall number of stopping muons remains nearly constant - with ~ 6.8 % of all impinging muons. What changes significantly, however, is the number of stopping muons that are not detected by plastic scintillator volumes. For a *Hollow Cylindrical Muon Veto* of $h = 10$ cm operating in combination with the *Cryogenic Muon Veto* only ~ 2.1 % of all stopping muons are eluding detection (of which

Table 4.3.: *Efficiency values for an additional Hollow Cylindrical Muon Veto. The efficiency ε provides a measure of the number of muons that pass through the lead and are not detected by plastic scintillator volumes. The index "geometric" indicates that the efficiency calculation was based solely on the muon tracks, whereas the index "realistic" indicates that the efficiency calculation takes into account the energy deposition of the muons using the Bethe-Bloch formula. Applying a threshold on the track length allows furthermore to mimic a discrimination threshold. The installation of an additional Hollow Cylindrical Muon Veto increases the overall efficiency by roughly 0.38 %.*

	$\varepsilon_{geometric}$	$\varepsilon_{realistic}$ *(no threshold)*	$\varepsilon_{realistic}$ *(2.5 cm)*
Additional Hollow Cylindrical Muon Veto			
h = 10 cm *(z = 0 cm)*	99.73 %	99.60 %	99.43 %
h = 10 cm *(z = -2 cm)*	99.71 %	99.57 %	99.40 %
h = 10 cm *(z = -4 cm)*	99.68 %	99.54 %	99.36 %
h = 10 cm *(z = -6 cm)*	99.67 %	99.53 %	99.36 %
h = 20 cm *(z = 0 cm)*	99.77 %	99.68 %	99.54 %
h = 30 cm *(z = 0 cm)*	99.79 %	99.70 %	99.58 %

$\sim$60% are being stopped in lead and $\sim$35% are being stopped in polyethylene). This percentage of non-detected stopping muons corresponds to a flux of $\phi_{ND\_stop\_\mu} = 0.913\,\text{Hz}$. This number can be further reduced to $\sim 1.6\,\%$ for a height of the *Hollow Cylindrical Muon Veto* of $h = 20\,\text{cm}$ (corresponding to a flux of $\phi_{ND\_stop\_\mu} = 0.75\,\text{Hz}$) and to $\sim 1.5\,\%$ for a height of $h = 30\,\text{cm}$ (corresponding to a flux of $\phi_{ND\_stop\_\mu} = 0.68\,\text{Hz}$). The detailed results of the analysis of stopping muons are summarized in Table A.2 in Appendix A.

4.2.3. Simulated Count Rate of Cosmic Muons

For the NUCLEUS shielding arrangement, in which no *Cryogenic Muon Veto* is operating, the simulations predict a muon count rate of $\phi_{veto} = 673.1\,\text{Hz}$. The rate increases due to the operation of the *Cryogenic Muon Veto* to a value of $\phi_{veto} = 676.5\,\text{Hz}$, simply because the increased efficiency leads to an enhanced muon-tagging capability. Due to the $\cos^2\Theta$-distributed directionality of the muon flux, the additional installation of a component sitting on top of the *Top Muon Veto Panel* only has a minor effect on the overall muon count rate. When considering a *Hollow Cylindrical Muon Veto* with a height of $h = 10\,\text{cm}$, the count rate is found to be $\phi_{veto} = 678.1\,\text{Hz}$.

The previously, in [44] determined muon count rate of $(519 \pm 9)\,\text{Hz}$ for the NUCLEUS muon veto, which assumes a strongly simplified muon veto geometry and a muon tagging efficiency of 97 %, was therefore adjusted upwards by a factor of ~ 1.3.

4.3. Conclusions of the Geometrical Simulations

The simulations are clearly confirming the important role of the *Cryogenic Muon Veto* for the overall NUCLEUS muon veto performance, which turned out to be a key component towards achieving the targeted muon detection efficiency of $> 99\,\%$. The overall cosmic muon count rate of the NUCLEUS muon veto is estimated to $\sim 676\,\mathrm{Hz}$. The slight increase of the count rate by less than $3.5\,\mathrm{Hz}$, induced by the *Cryogenic Muon Veto*, can be explained by the increased efficiency and the reduced number of non-detected stopping muons. Another important conclusion is that the overall number of stopping muons is approximately the same in all arrangements. The dependence of the efficiency on the misalignment of the plastic scintillator disc is negligible, which allows flexibility in its positioning. The solution that is mechanically the easiest to implement, which is the one in which the *Cryogenic Muon Veto* is sitting on top of the mechanical support structure of the inner shielding (referring to a misalignment value of $z = $-4 cm), is accordingly the preferred solution (for further information see Section 5.1.1). The operation of the proposed *Hollow Cylindrical Muon Veto* would slightly increase the overall NUCLEUS muon veto efficiency to a value of $99.58\,\%$, which is the highest achievable efficiency value according to the presented study.

Finally, a different look at the results presented will be taken. For this purpose, the ratio of the rate of non-detected stopping muons ($\phi_{ND\_stop\_\mu}$) to the overall muon veto count rate (ϕ_{veto}) - which provides a vivid and useful measure of the particularly dangerous non-detected stopping muons - is printed in Table 4.4. From this it can be deduced that the installation of the *Cryogenic Muon Veto* reduces the number of non-detected stopping muons by a factor of ~ 2.1. The additional installation of the *Hollow Cylindrical Muon Veto* with a height $h = 10\,\mathrm{cm}$ lowers this number by another factor of ~ 1.38. When the height is now increased to $h = 30\,\mathrm{cm}$, the number of stopping muons further decreases by factor of ~ 1.34, which gives a total reduction by a factor of ~ 3.91. Thus, the development of the *Hollow Cylindrical Muon Veto* - proposed within the frame of this thesis - is a precious concept whose necessity will depend crucially on the impact of non-detected stopping muons on the NUCLEUS target detector operation, which remains to be studied in depth by Geant4 simulations. The previously presented findings on the impact of this component on the overall performance of the NUCLEUS muon veto, together with the ease of transferability and flexibility of the envisaged NUCLEUS muon veto detector technology would allow for a customized and straightforward realization of this additional component.

Table 4.4.: *Rate of the non-detected stopping muons ($\phi_{ND\_stop\_\mu}$) divided by the overall muon veto count rate (ϕ_{veto}). This ratio represents a measure of the particularly dangerous non-detected stopping muons, and allows a vivid comparison between the different geometrical arrangements. The installation of the Cryogenic Muon Veto reduces the number of stopping muons by a factor of ∼ 2.1. The installation of the Hollow Cylindrical Muon Veto with a height h = 10 cm reduces the number of stopping muons by an additional factor of ∼ 1.38. The increase of height of the Hollow Cylindrical Muon Veto to h = 30 cm reduces the number of stopping muons by an additional factor of ∼ 1.34.*

	$\phi_{ND\_stop\_\mu}$ / ϕ_{veto}	
No Cryogenic Muon Veto		
	0.391 %	
		÷2.1
Cryogenic Muon Veto		
z = 0 cm	0.185 %	
z = -2 cm	0.179 %	
z = -4 cm	0.174 %	
z = -6 cm	0.182 %	÷1.38
Additional Hollow Cylindrical Muon Veto		
h = 10 cm & *z = 0 cm*	0.134 %	
h = 10 cm & *z = -2 cm*	0.147 %	
h = 10 cm & *z = -4 cm*	0.145 %	
h = 10 cm & *z = -6 cm*	0.154 %	÷1.34
h = 20 cm & *z = 0 cm*	0.111 %	
h = 30 cm & *z = 0 cm*	0.100 %	

5. Experimental Investigation of the Low-Temperature Behavior of Organic Plastic Scintillators

Contents

5.1. Expected Low-Temperature Behavior of Organic Plastic Scintillators

5.1.1. Organic Plastic Scintillators

The various questions that arise concerning the behavior of organic plastic scintillators at low-temperatures have been grouped into two categories for the purpose of this thesis. These two categories, which will be investigated in the following both in a theoretical and an experimental approach, can be essentially summarized by the two questions posed hereafter: **Does the scintillation process still work at sub-Kelvin temperatures? Is it possible to cool down an organic plastic scintillator to sub-Kelvin temperatures?**

Organic Plastic Scintillation Process at Low-Temperatures

A first important conclusion and a promising indication of a confirmation to the first question raised above can be drawn from a review of the energy level diagram of an organic

scintillator molecule shown in Figure 3.2 in Section 3.3.1. The transition from the first excited singlet state S_1 to the ground state S_0, which is the principal scintillation process in organic plastic scintillators, corresponds to an energy difference of $\Delta E \sim 3\text{-}4\,eV$. The equation $E = k_B T$, where k_B denotes the Boltzmann constant and T the temperature, can be used as a scale factor for energy values in molecular-scale systems. According to this formula, an energy spacing between electronic states in organic scintillator molecules of 1 eV would correspond to temperatures of $\sim 11600\,K$. It is therefore assumed that the fluorescence process $S_1 \rightarrow S_0$ does not involve thermal processes. The scintillation process is therefore expected to work also at sub-Kelvin temperatures. However, the involvement of secondary processes, such as the phosphorescence process $T_i \rightarrow S_i \rightarrow S_0$ or the excitation of finestructure levels S_{ii} might alter the light yield depending on the temperature.

L. Peralta [83] studies the possible temperature dependence of the light yield of several organic plastic scintillators, including the polyvinyltoluene based plastic scintillator BC-404 and the polystyrene based scintillating fibers BCF-10 and BCF-60, all fabricated by Saint Gobain [84]. Confirming the specifications provided by the manufacturer, Peralta's work shows that the light-yield of the polyvinyltoluene based BC-4xx series is nearly constant over a temperature range from -60 $°C$ to +50 $°C$. Nevertheless, a non-vanishing negative temperature dependence of $(-0.26 \pm 0.03)\,\% / °C$ is found for the polystyrene based plastic scintillators BCF-10 and BCF-60. A physics interpretation of why the light output of plastic scintillators is increased at lower temperatures is pending in literature.

In this respect, organic liquid scintillators are described considerably more extensive. A. Sörensen et al. [85] investigate the temperature quenching specifically in LAB based liquid scintillators in a temperature range from -5 $°C$ to +50 $°C$. A negative temperature dependence of $(-0.29 \pm 0.01)\,\% / °C$ is determined, assuming linear behavior. The overall increase in scintillation light emitted by organic liquid scintillators with decreasing temperatures has been previously reported throughout literature [86–88] and is partly explicable by the existence of vibrational excitations, which are less excited at lower temperatures. When in this regard the energy level diagram of an organic scintillator molecule is recalled again, it can be observed that the typical energy spacing between the levels originating from vibrational excitations (S_{00}, S_{01}...) is around $\sim 0.15\,eV$ [49], corresponding to temperatures of 1740 K. Hence, it is large compared to average thermal energies, resulting in nearly all molecules being in the S_{00} state at room temperature. The effect of the vibrational states on the temperature dependence of the light yield is therefore expected to be minor for the temperature range of interest. Sörensen consequently attributes the temperature quenching effect primarily to the temperature dependence of triplet state de-excitations. Alternate de-excitation modes available to the excited triplet states that do not involve the emission of light, such as collisional processes, are expected to be suppressed at lower temperatures, resulting in an increased light yield.

Cool-Down Behavior of Organic Plastic Scintillators

The cool-down time of the NUCLEUS detector unit from room temperature to the desired temperature of $\mathcal{O}(10\,mK)$ can take up to several days. In order to ensure a seamless cool-down of the inner volume it is crucial to understand the time required to cool down critical (i.e. only weakly thermally conductive) components, such as the NUCLEUS *Cryogenic Muon Veto* to its final operating temperature of $\sim 900\,mK$. If these critical components exhibit a significantly longer thermalization time than the rest of the detector unit, the

entire cool-down of the NUCLEUS cryostat may be strongly affected and delayed. This time depends essentially on the *heat capacity* and the *thermal conductivity* of the organic plastic scintillator as well as the *thermal contact resistance* of the thermal coupling. In the case of the NUCLEUS *Cryogenic Muon Veto* the intended realization of the thermal coupling is explained in Figure 5.1, in which the envisaged mechanical support structure for the inner shielding can be seen. In this variant, the NUCLEUS *Cryogenic Muon Veto* is located underneath the MC plate and placed on top of a copper disc, which itself is thermally coupled to the Still plate, and thus features a temperature of $T_{Still} \sim 900\,\mathrm{mK}$. This copper disc, which will be mechanically held by a tube, will therefore serve both as thermal bath for the NUCLEUS *Cryogenic Muon Veto* as well as mechanical support for the inner passive shielding. The positioning of the plastic scintillator disc underneath the MC plate raises the question of a possible radiative heat transfer of the thermalized NUCLEUS *Cryogenic Muon Veto* to the cooler cryostat surrounding. Another relevant thermal property that has to be considered to avoid any mechanical stress is the *thermal expansion*.

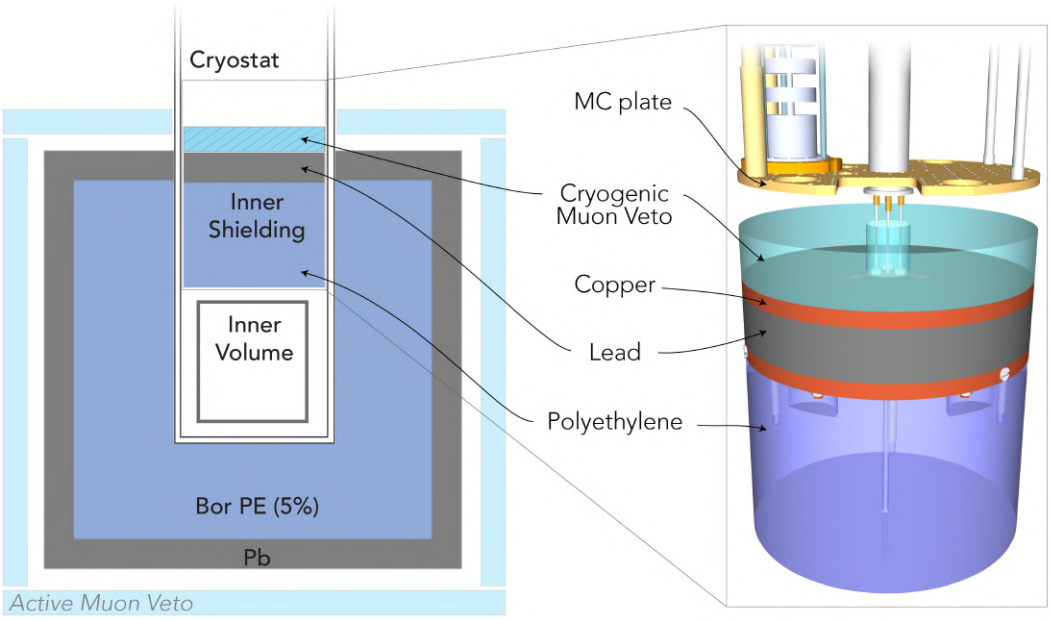

Figure 5.1.: *Schematic, cross-sectional view of the NUCLEUS experiment, with detailed zoom-in on the inner shielding. The inner active and passive shieldings will be installed underneath the MC plate, however they will be thermally coupled to the Still plate. The mechanical support structure holding the inner shielding will be fixed to the spring tube and will serve as thermal contact. The structure consists of two copper discs with a height of 1.5 cm, to which the polyethylene and the lead of the inner passive shielding will be fixed. The NUCLEUS Cryogenic Muon Veto will sit on top of the copper - the thermal coupling in this realization is only due to the contact pressure of the plastic scintillator disc. It is thermalized at ∼ 900 mK and has a distance of ∼ 4.5 cm to the cooler MC stage.*

W. Reese [89] investigates the several thermal properties of commercial samples of amorphous polystyrene between temperatures of 4.5 K and 1 K. The work by Reese states that the *thermal conductivity* and the *heat capacity* of polymers in this temperature range can be understood in terms of Klemens' theory [90]. The theory describes *thermal conductivity* by means of lattice waves in amorphous materials. The random arrangements of molecular units can be considered as point defects, which scatter phonons.

Heat Capacity Values of the *heat capacity* of polystyrene have been obtained by W. Reese in an experimental manner. The data are found to be reasonably consistent with a cubic temperature dependence, predicted by Klemens' theory. The volumetric *heat capacity* of a polystyrene sample is determined to be $C\,/\,T^3 = (735 \pm 50) \cdot 10^{-7}\,\mathrm{J}\,/\,(\mathrm{cm}^3 \cdot \mathrm{K}^4)$ [89]. Similar behavior of the *heat capacity* can in principle be assumed for other polymers. However, no values were found in literature for polyvinyltoluene. To evaluate the *heat capacity* phenomenologically, various excitations have to be considered. The complex chain structure within polymers allows for a variety of vibrational motions, resulting in a combination of various contributions to the *heat capacity* of longitudinal and transversal phonons. Therefore, in the case of polyvinyltoluene one important feature, namely the functional methyl group attached to the benzene-ring has to be taken into account. To visualize this characteristic, the structural formula of the two different polymers shown in Figure 3.3 should be recalled. This functional group branching out the benzene-ring of polyvinyltoluene alters the electronic and vibrational states, and can potentially induce additional rotational states, which might already be excited at thermal energies. This, in turn, would lead to an enhancement of the *heat capacity*, which could affect the cool-down time of the NUCLEUS *Cryogenic Muon Veto*.

Thermal Conductivity C. Huang et al. [91] make an attempt to quantify thermal transport mechanisms (i.e. the *thermal conductivity*) in polymers in terms of the polymers' morphology. In general, polymers have a very low thermal conductivity compared to the multiple other materials which are constituent parts of the NUCLEUS cryogenic infrastructure. In detail, the exact value of the *thermal conductivity* of a specific polymer depends considerably on its chain alignment (determining the periodicity of the polymer), on out-branching side chains (inducing additional vibrational levels) and on inter-chain couplings (i.e. inter-molecular H-bonds between adjacent chains). Subtle morphological differences on the molecular level can significantly alter the *thermal conductivity* of a polymer. Due to the temperature dependence of the number of phonons, also the *thermal conductivity* strongly depends on the temperature. In the case of polystyrene, G. Ventura [54] specifies $\kappa = 2 \cdot 10^{-4} \cdot T^{1.87}\,\mathrm{W}/(\,\mathrm{cm} \cdot \mathrm{K})$ for the temperature range from 0.4 K to 1 K. W. Reese's [89] experimental evaluation of the *thermal conductivity* confirms such a behavior, and yields values up to a temperature of 4.5 K.

Thermalization Time After the thermal properties of plastic scintillators have been investigated, the thermalization time of the NUCLEUS *Cryogenic Muon Veto* can now be studied. Fourier's law of heat conduction [92] states that the local heat flux density $\vec{q}$ equals the product of the thermal conductivity κ and the negative local temperature gradient:

$$\vec{q} = -\kappa \nabla T \tag{5.1}$$

Assuming one dimensional heat flow between two parallel outer surfaces A of a homogeneous body, which are separated by a distance L and exhibit a temperature difference of ΔT, the heat conduction across the body between those two surfaces can be written as follows:

$$\dot{Q}(T) = \frac{A \kappa \Delta T}{L} \tag{5.2}$$

The change in temperature of the body corresponding to a given heat conduction depends on the body's mass m and on the material's *heat capacity* c:

$$\dot{T} = -\frac{\dot{Q}}{c \cdot m} \tag{5.3}$$

For the intended realization of the thermal coupling of the *Cryogenic Muon Veto*, in which the cooling is solely due to the contact pressure on the copper disc, equation 5.3 can be solved to predict how long it will take to cool the upper, non-thermalized end of the plastic scintillator disc from the starting temperature T_0 to the desired temperature T_{PS}. The solution can be written as follows:

$$t = \frac{-ln(\frac{T_{PS}-T_{Still}}{T_0-T_{Still}}) \cdot c \cdot m \cdot L}{A \cdot \kappa} \tag{5.4}$$

An important variable, which has been completely disregarded in the previous considerations is the *thermal contact resistance* R_C. It is a measure of an interface's resistance to thermal flow, and accounts as such for physical conditions like the contact pressure, the surface roughness and the surface cleanliness. The *thermal contact resistance* leads to a temperature drop at the discontinuity and therefore strongly determines the ability to conduct heat between two bodies. In practice, attempts are made to reduce R_C by optimizing the thermal coupling (e.g. by adding pressure or a suitable grease to the interface). However, due to the complex atomic nature of the interface, R_C can barely be determined in a non-experimental manner [54]. Since a calculation of the thermalization time of the *Cryogenic Muon Veto* based on these basic considerations does therefore not seem to be reliably feasible, this problem is best subjected to a dedicated measurement.

Heat Transfer by Radiation Any body of surface A at temperature T (larger than absolute zero) emits an electromagnetic radiation due to the thermal motion of its particles. The total radiated power of such a body can be calculated via the Stefan-Boltzmann law [92] as follows:

$$\dot{Q} = \sigma \varepsilon A T^4 \tag{5.5}$$

In this equation, σ denotes the Stefan–Boltzmann constant and ε the emissivity of the body. Due to its electromagnetic nature, this process also takes place in vacuum, and can therefore lead to heat transfer between two separated components inside a cryogenic infrastructure such as the NUCLEUS cryostat. Figure 5.1 illustrates the position of the plastic scintillator disc of the NUCLEUS *Cryogenic Muon Veto* with $\sim 4.5\,\mathrm{cm}$ distance to the MC plate of the cryostat. This positioning of the plastic scintillator, which is thermalized at 900 mK and placed underneath the MC plate, which is considerably cooler at 10 mK, raises the question whether heat transfer between the two bodies and thus an influence of the temperature of the MC stage is to be expected. Approximating the MC plate and the top of the plastic scintillator disc as circular surfaces with $A = 700\,\mathrm{cm}^2$ the radiative power transfer can be calculated via:

$$\dot{Q} = \sigma A (T_{PS}^4 - T_{MC}^4) \frac{\varepsilon_{PS}\varepsilon_{MC}}{\varepsilon_{PS} + \varepsilon_{MC} - \varepsilon_{PS}\varepsilon_{MC}} \tag{5.6}$$

Assuming values for the emissivity of $\varepsilon_{MC} = 0.023$ for polished copper and $\varepsilon_{PS} = 0.97$ as conservative value for polymer based plastics [93] as well as temperatures of $T_{MC} = 10\,\mathrm{mK}$ for the MC plate and $T_{PS} = 900\,\mathrm{mK}$ for the fully thermalized plastic scintillator disc, the radiative heat transfer from the NUCLEUS *Cryogenic Muon Veto* to the MC plate can be calculated to $\dot{Q} = 3.373 \cdot 10^{-11}\,\mathrm{W}$. Compared to the cooling power of the MC plate at 10 mK of $\sim 19 \cdot 10^{-6}\,\mathrm{W}$ the radiative power originating from the NUCLEUS *Cryogenic Muon Veto* is completely negligible.

Thermal Expansion Coefficients A compilation of the *thermal expansion coefficients* of all materials that were regarded as interesting in the context of this work can be found

in the Appendix B. In this context, it is important to prevent possible mechanical stress arising when materials with significantly different *thermal expansion coefficients* are brought together or positioned without sufficient space for expansion. The *thermal expansion coefficient* of polyvinyltoluene is $78 \cdot 10^{-6} \,/\, K$ [94] and of polystyrene is $70 \cdot 10^{-6} \,/\, K$ [95]. While typical metals exhibit an integrated contraction of 0.2 - 0.4 % between 300 K and 4 K, typical plastics feature an integrated contraction of 1 - 2 % in the same temperature range [54]. In the case of polyvinyltoluene and polystyrene, the values for integrated contraction in the range 300 K to 900 mK can be estimated to ~ 2.3 % each, assuming temperature-independent *thermal expansion coefficients*. Without anticipating any details of the design (for further information see Section 6.1), it can already be pointed out that no mechanical stress is expected due to the similarity of the *thermal expansion coefficients* of the different materials belonging to the refrigerated part of the NUCLEUS *Cryogenic Muon Veto*. The acrylic cladding layer of the wavelength shifting fibers (for further information see the following Section 5.1.2) exhibits a *thermal expansion coefficient* of $68 \text{ - } 75 \cdot 10^{-6} \,/\, K$, while the clear optical epoxy resin, used to attach the fibers to the plastic scintillator, has a *thermal expansion coefficient* of $72 \cdot 10^{-6} \,/\, K$.

Conclusions

As a consequence of these insights from the literature study regarding the low-temperature behavior of organic plastic scintillators it was decided to experimentally investigate the thermal properties of two different plastic scintillators, based on two various base polymers. Additionally to the polyvinyltoluene based plastic scintillator EJ-204, fabricated by Eljen Technology [94], complementary tests were performed using the polystyrene based plastic scintillator UPS 923-A[1], fabricated by the Institute for Scintillation Materials of Ukraine [95]. Due to the complex nature of the thermal contact resistance and the sensitive dependence of the thermal conductivity and the heat capacity on the exact molecular structure of the specific polymer, it was decided that a parameter as important for the NUCLEUS cryogenic arrangement as the *thermalization time* of the NUCLEUS *Cryogenic Muon Veto* should be determined in a dedicated experimental manner. The aim is to ensure that the installation of a plastic scintillator based muon veto will not severely delay the cool-down of the NUCLEUS cryostat. Since, to the best of the author's knowledge, no experimental studies on the *scintillation mechanism of organic plastic scintillators at sub-Kelvin temperatures* have ever been reported in the literature to date, this was also subjected to experimental examination. The aim is to confirm the expected functionality of the scintillation process at sub-Kelvin temperatures. The prototype measurements presented below are therefore considered as fundamental and indispensable proof-of-concept for the frame of this thesis, and to be potentially of interest for a future systematic study of the temperature dependence of the organic plastic scintillation process, which goes beyond the scope of this thesis.

[1] The plastic scintillator UPS 923-A is the polystyrene based equivalent of the BC-4xx series. It is doped with 2 % PTP and 0.03 % POPOP and has a slightly lower light output than the polyvinyltoluene based counter-sample EJ-204. Due to the materials' suitability for the detection of charged particles, it is for instance being instrumented in the GERDA experiment as plastic scintillator muon veto centred over the neck of the cryostat [96].

5.1.2. Wavelength Shifting Fibers

For considerations regarding the low-temperature behavior of wavelength shifting fibers, it is important to recognize that such fibers are essentially organic plastic scintillators. The deliberations summarized in Section 5.1.1 can therefore also be transferred to the description of wavelength shifting fibers. In the case of the fibers BCF-91A by Saint Gobain [97], which are especially relevant in the frame of this work and which have been schematically shown in Figure 3.4, the scintillating core is composed of an polystyrene based plastic scintillator, and the surrounding cladding layer is made out of acrylic. The attenuation length of this fiber is found to be 3.8 m [98]. Given the thermal expansion coefficient of polystyrene and of acrylic plastic, no mechanical constraints are expected to arise due to thermal expansion. Moreover, the fibers have been previously tested and employed under cryogenic conditions, more precisely at liquid argon temperatures, as part of the liquid argon veto of the GERDA experiment [98, 99]. No literature has been found detailing the behavior of the fibers at even lower temperatures. Nevertheless, D. McKinsey et al. [100] provide interesting remarks in the context of a work about the development and characterization of detectors for the counting of low energy ionizing events in liquid helium using wavelength shifting light collection. The development of a wavelength shifting fiber based detector features the operation of 0.8 mm diameter Y11(250) fibers from Kuraray [101] at temperatures below 4.2 K. These fibers have - similar to the fibers BCF-91A - a double-layer structure consisting of a polystyrene core with a fluorescent agent. The cladding is made out of methacrylate. D. McKinsey et al. have found that the attenuation length of the Y11(250) (2.9m) is not temperature dependent.

5.2. Description of the Experimental Setups

In accordance with the conclusions drawn from the literature review presented in Section 5.1, a number of fundamental questions were identified, which will be further investigated in an experimental manner in the following sections. In a first step, the **thermalization behavior** of organic plastic scintillators was studied. Due to the limited availability of measurement time within the required cryogenic infrastructure this was only done for the more critical of the two samples, namely the polyvinyltoluene based plastic scintillator EJ-204. In a second step, the **evolution of the light yield** as well as of the **muon pulse shape**, depending on the low-temperature response of the scintillation mechanism, was studied for the polystyrene based plastic scintillator UPS 923-A. In order to verify those key physical aspects of the intended NUCLEUS *Cryogenic Muon Veto* detector concept, smaller-scale prototypes were assembled mimicking the envisaged final design. A schematic sketch along with a picture of those prototypes can be seen in Figure 5.2. They consist of small cylindrical samples of plastic scintillators with a height and a diameter of 42 mm each and have four of the wavelength shifting fibers BCF-91A glued into small grooves on the side. The applied adhesive is the single component cyanoacrylate adhesive Loctite 406 [102]. The fibers have a squared cross-sectional surface of 1 mm^2 each, a length of 90 cm and are bundled at the end via a connector towards the SiPM. Optical grade silicon grease was used for the coupling of these fibers to the active surface of the SiPMs. An important requirement on the prototypes was their compactness, allowing measurements to be performed in various cryogenic environments such as a liquid nitrogen storage dewar or the NUCLEUS cryostat.

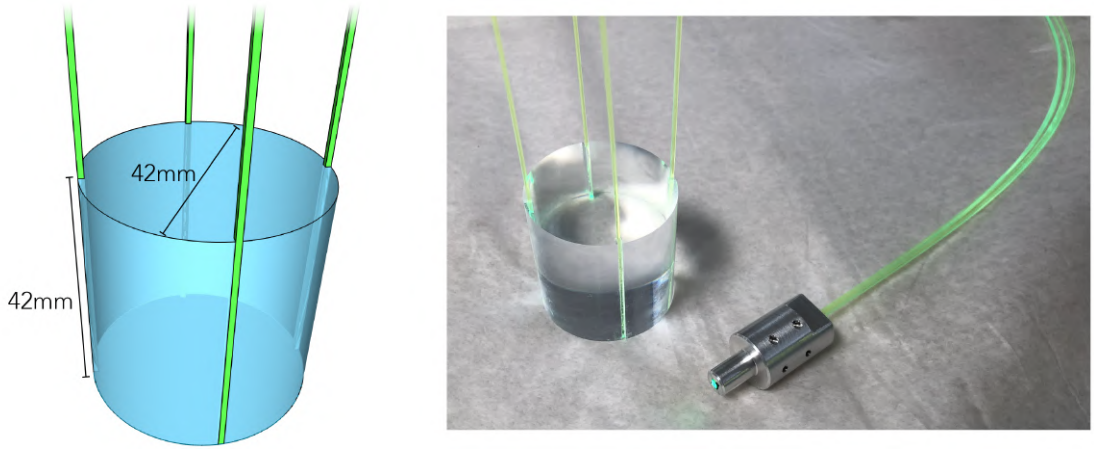

Figure 5.2.: *Schematic drawing (left) and picture (right) of the smaller-scale plastic scintillator prototypes of the NUCLEUS Cryogenic Muon Veto. For an experimental investigation of the low-temperature behavior and the evolution of the light yield of different organic plastic scintillators, namely one polyvinyltoluene and one polystyrene based, small cylindrical samples with wavelength shifting fibers glued into grooves on the side were assembled. The fibers were bundled via a connector, which serves as the coupling to the SiPM. Due to the compactness of these prototypes they can be operated within cryogenic storage dewars and sufficiently large cryostats.*

5.2.1. Plastic Scintillator Installation in Liquid Nitrogen Dewar

In a first step, the plastic scintillator prototypes were operated in a liquid nitrogen storage dewar located in a laboratory of the *Département de Physique Nucléaire* of the *Centre CEA de Saclay* in Paris-Saclay. The experimental setup used to cool the prototypes down to liquid nitrogen temperatures (77 K) is shown in Figure 5.3. It consists of a cryogenic storage dewar, containing ~ 30 vol% of liquid nitrogen. The level of liquid can be kept constant due to regular checks and additional sealing of the dewar with a plug. The plastic scintillator prototypes are encapsulated by a wire cage, which is fixed to a light-tight PVC tube and surrounded by expanded polystyrene. The wavelength shifting fibers are guided through the PVC tube and coupled to a SiPM. By operating the SiPM at constant room temperature, possible temperature-dependent effects of the SiPM and the plastic scintillator are not intermingled and can be attributed more conclusively. During operation the whole system was covered by opaque black fabric. The PVC tube with attached wire cage is held by a mechanical arm and can be gradually lowered into the storage dewar. With additional pre-cooling of the plastic scintillator prototype in a commercial freezer, very slow and gentle cooling can be achieved over a timespan of $\mathcal{O}(24\,\mathrm{h})$. Because of the non-vacuum environment inside the storage dewar it is already sufficient for an efficient cool-down to liquid nitrogen temperature to position the samples just above the surface of the liquid nitrogen. Thus, the plastic scintillator does not need to be directly exposed to the liquid. The temperature is monitored on top of the plastic scintillator cylinder with a calibrated silicon diode sensor.

The electronic data-acquisition system compiled for the plastic scintillator installation inside a liquid nitrogen dewar is schematically shown in Figure 5.4. As the time-constant of the plastic scintillator instrumented with WLS fiber-based light-guide system together with a SiPM-based read-out system is of the order of 100 ns, the data-acquisition system needs to be sufficiently fast. The instrumentation of a KETEK PE3325-WB SiPM necessitates

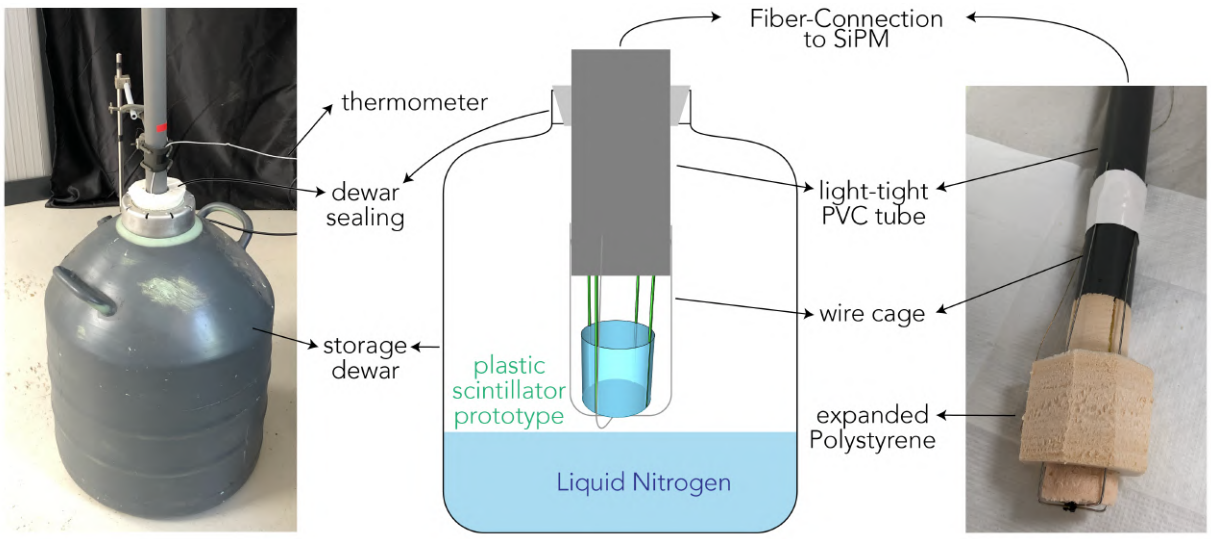

Figure 5.3.: *Schematic drawing of the experimental setup for measurements at liquid nitrogen temperatures (middle) and pictures of the storage dewar (left) and the PVC tube with attached wire cage encapsulating the plastic scintillator prototypes (right). The prototype unit can be gradually lowered into the storage dewar and like that slowly be cooled to liquid nitrogen temperatures. The light emitted upon an interaction of a muon with the plastic scintillator is guided via wavelength shifting fibers through the PVC tube and read by a SiPM at room temperature. The temperature on top of the plastic scintillator cylinder is monitored with a calibrated silicon diode sensor.*

the external signal amplification via a Fast Amplifier module. The unaltered SiPM signals have amplitudes of the order of 10 mV, and are therefore located at the lower edge of the dynamic range of the analog-to-digital converter (ADC). Early gain amplification is therefore important for maximising the signal-to-noise ratio. Furthermore, signal inversion is done via a Fan In - Fan Out module (FIFO). For analog-to-digital conversion of the signal the prototype module LPSC Grenoble was used. The flash-ADC module, which was initially developed for the STEREO experiment[2], is operating in a way that an integration gate with a length of up to 240 ns is applied to the signals. Like that, information about the total energy deposition inside the plastic scintillator panel can be retrieved. The module allows for external triggers, internal gain amplification and internal threshold settings.

[2]The STEREO experiment investigates possible neutrino oscillations from a nuclear reactor into light sterile neutrinos, applying neutrino detection in cell-segmented volumes of Gd-loaded liquid scintillator through the inverse β-decay process. The experiment is located at the Institut Laue-Langevin (ILL) in Grenoble, France [103].

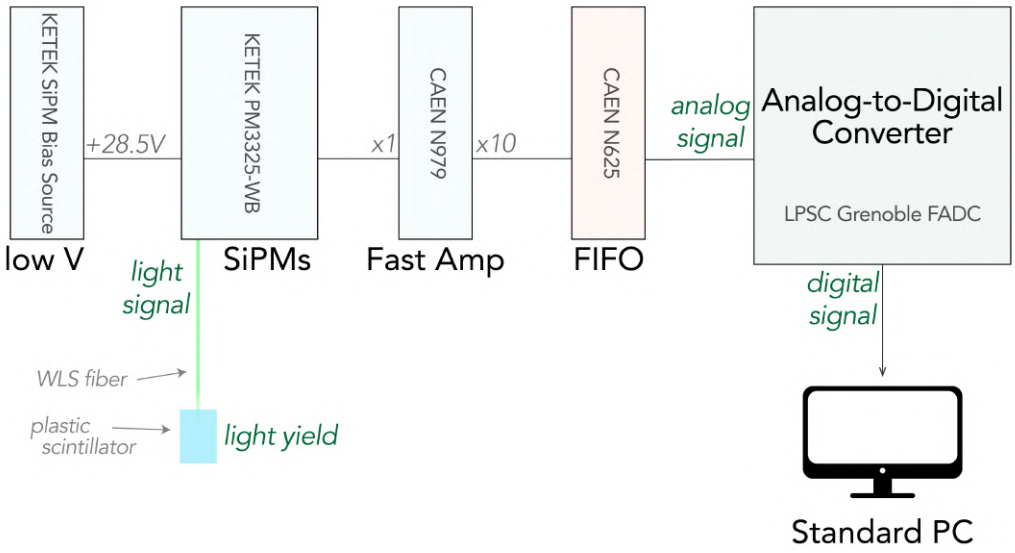

Figure 5.4.: *Wiring scheme of the data-acquisition system and the SiPM KETEK PE3325-WB, which was compiled for the installation of the plastic scintillator prototype inside a liquid nitrogen dewar. The operation of the SiPMs with a voltage of +28.5 V corresponds to an overvoltage of ∼4 V. The light signal of the prototype is converted into an analog signal by the SiPM. The analog signal is subsequently amplified by a Fast Amplifier, inverted by a Fan In - Fan Out and sent to the analog-to-digital converter, which in this case was the LPSC Grenoble flash-ADC. The digital signal (i.e. the value of an integration over an interval of 240 ns) is then provided for further analysis. The plastic scintillator is shown in blue and the WLS fibers in green.*

5.2.2. Plastic Scintillator Installation in NUCLEUS Cryostat

In a second step, the plastic scintillator prototypes were operated inside the NUCLEUS cryostat located in a laboratory of the *Chair for Experimental Astroparticle Physics* of the *Technical University of Munich*. The experimental setup used to cool the prototypes down to sub-Kelvin temperatures (∼ 900 mK) is shown in Figure 5.5. The different cooling stages and plates of the NUCLEUS cryostat have already been described in Section 2.3. In order to realistically replicate the intended thermal coupling of the final NUCLEUS *Cryogenic Muon Veto*, it was decided to operate the plastic scintillator prototypes within a customized copper holder, which can be screwed to the Still plate as a precisely fitting insert. Stainless steel clamps - both on the side and via copper bolts from above - secure the cylindrical plastic scintillator in place, but do not result in any additional cooling due to their low thermal conductivity. The thermal coupling is thus exclusively due to the contact pressure of the plastic scintillator sample onto the copper plate, slight additional pressure induced by the clamping and optimized by the insertion of vacuum grease to the plastic-copper interface. The wavelength shifting fibers are guided through the NUCLEUS cryostat and optically coupled to a SiPM fixed to the bottom of the 300 K plate. Operating the SiPM at a constant temperature of 300 K prevents the entanglement of the potential temperature-dependent effects of the SiPM and the plastic scintillator. The temperature can be monitored on top of the plastic scintillator cylinder with a calibrated resistance thermometer screwed into the copper block sitting on top of the plastic scintillator. Images of the prototype installed inside the NUCLEUS cryostat can be seen in Figure 5.6.

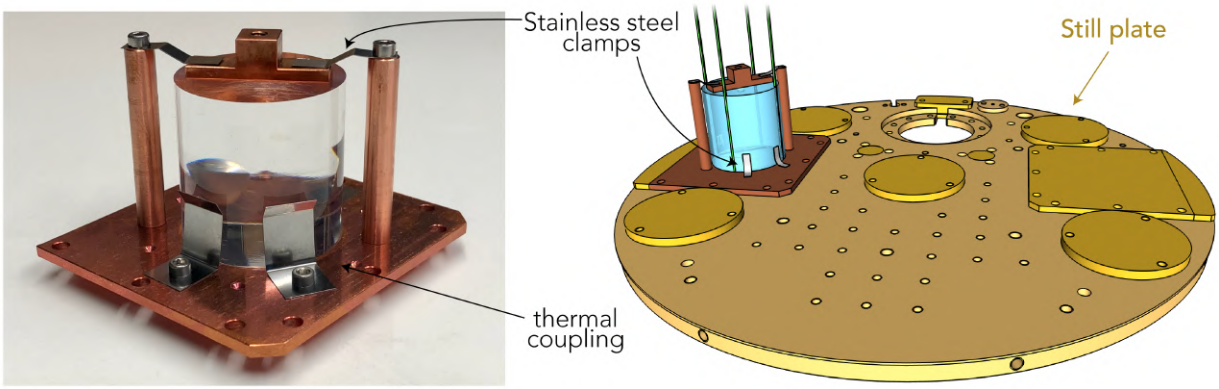

Figure 5.5.: *Picture (left) and schematic drawing (right) of the experimental setup for measurements at sub-Kelvin temperatures. The plastic scintillator prototypes are positioned and thermally coupled to a copper plate, which is screwed to the Still plate. In that way, the intended thermal coupling of the final design can be realistically replicated. The scintillation light of the plastic scintillator is guided via the wavelength shifting fibers to the top of the cryostat and read by a SiPM fixed to the bottom of the 300 K plate. The temperature on top of the plastic scintillator cylinder can be monitored with a calibrated resistance thermometer screwed into the copper block sitting on top.*

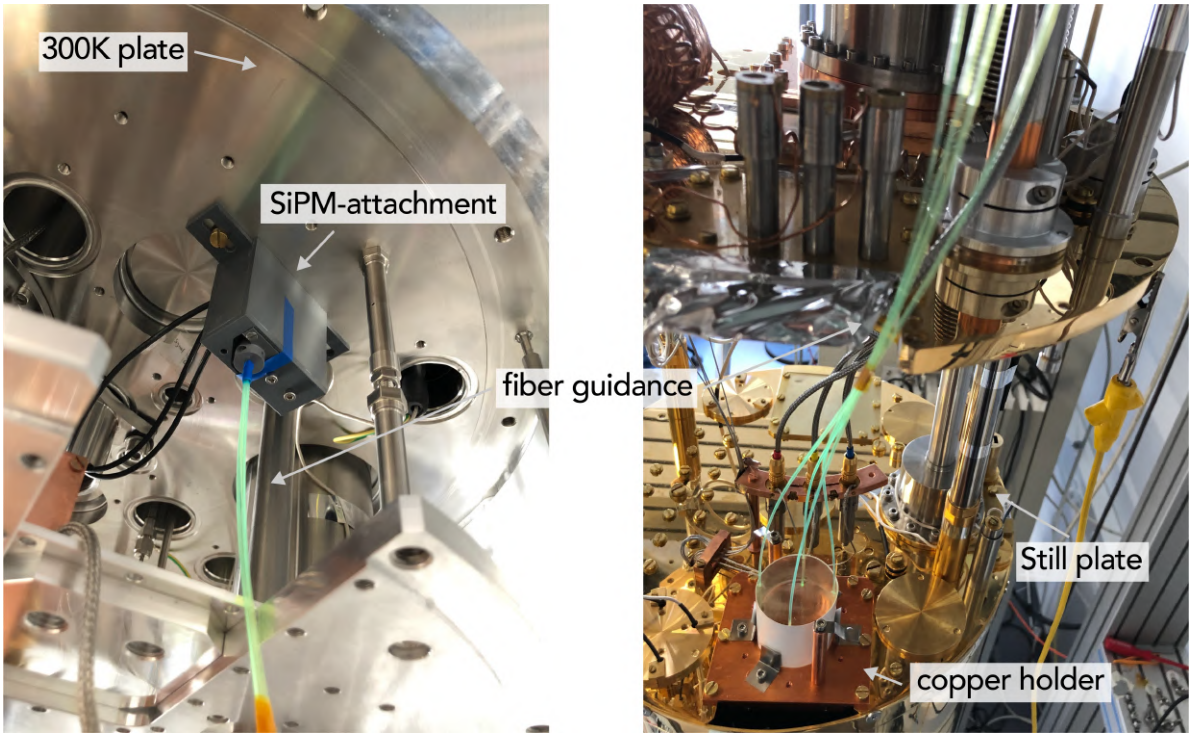

Figure 5.6.: *Installation of the plastic scintillator prototype in the NUCLEUS cryostat. The prototype is thermally coupled to the Still stage via a customized copper holder (right). The fibers are guided through the cryostat to the SiPM (left), which sits at the bottom of the 300 K plate. The temperature of the SiPM can therefore be kept constant.*

The electronic data-acquisition system compiled for the plastic scintillator installation inside the NUCLEUS cryostat is schematically shown in Figure 5.7. The instrumentation

of a pre-amplified and gain-stabilized KETEK PE3325-WB TIA TP SiPM module attached to the bottom of the 300 K plate allowed first commissioning of the intended final read-out system of the light signal (for further information see Section 6.1). This KETEK module features the same SiPM as instrumented in the experimental setup for measurements at liquid nitrogen temperatures, together with additional frond-end electronics. For analog-to-digital conversion of the signal a Rohde & Schwarz RTO 2004 Oscilloscope was used [104].

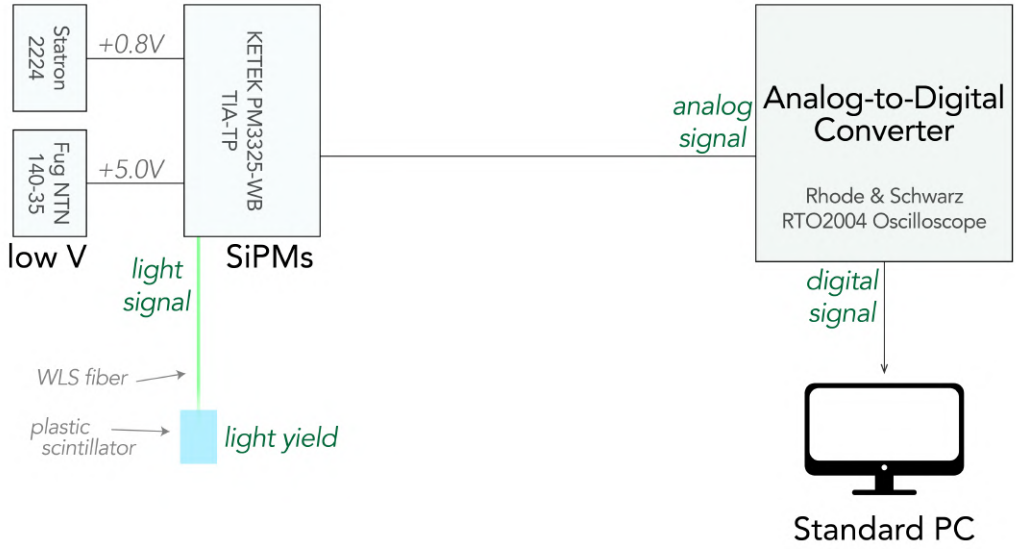

Figure 5.7.: *Wiring scheme of the data-acquisition system and the gain-stabilized SiPM KETEK PE3325-WB TIA TP, which was compiled for the installation of the plastic scintillator prototype inside the NUCLEUS cryostat. The SiPMs require two separate bias supplies - a main power supply input of 5 V and a gain control voltage, tunable between 0 V and 1 V. The light signal of the prototype is converted into an analog signal by the SiPM, pre-amplified and directly sent to the analog-to-digital converter, which in this case was a Rohde & Schwarz RTO 2004 Oscilloscope. The digital signal (i.e. the value of an integration over an interval of 240 ns) is then provided for further analysis. The plastic scintillator is shown in blue and the WLS fibers in green.*

5.3. Observations of the Experimental Investigation

5.3.1. Thermalization Time of the Polyvinyltoluene based Plastic Scintillator EJ-204

The thermalization behavior of organic plastic scintillators was investigated for a cylindrical sample of the polyvinyltoluene based plastic scintillator EJ-204, which was installed in the NUCLEUS cryostat as previously described. No WLS fibers were attached to the sample during this measurement. Both the temperature of the upper side of the cylindrical plastic scintillator (T_{PS}) as well as of the Still stage itself (T_{Still}), representing the thermal bath, were monitored. The time required for the Still stage to reach its base temperature can now be compared to the time required for the top of the cylinder to reach thermal equilibrium. In Figure 5.8 the two respective temperature curves are shown. Starting from

100 K, the Still stage (blue curve) reaches its base temperature $T_{Still} \approx 0.86\,\mathrm{K}$ within $\sim 27\,\mathrm{h}$. The pre-cooling of the Still stage is done via a pulse tube refrigerator, whose cooling power decreases with decreasing ΔT [54]. After $\sim 6\,\mathrm{h}$, the cooling power of the Still stage reaches the range of the emitted power of the plastic scintillator sample. The cooling rate of the Still stage therefore decreases considerably. After $\sim 25\,\mathrm{h}$, $^3\mathrm{He}/^4\mathrm{He}$ mixture is injected into the mixing chamber, external pressure is applied to the mixture and the final cooling to the base temperature of the cryostat (and thus also of the Still stage) is initiated. The upper side of the cylindrical plastic scintillator (red curve) fully thermalizes within $\sim 52\,\mathrm{h}$, with the time onset defined as the point in time in which $T_{Still} = 100\,\mathrm{K}$. This corresponds to a delay in thermalization time of the plastic scintillator with respect to the Still stage of $\sim 25\,\mathrm{h}$. Interestingly, the thermal equilibrium of the plastic scintillator is reached at a temperature of $T_{PS} \approx 1.19\,\mathrm{K}$, which is 0.33 K higher than that of the Still stage itself. This can also be seen in Figure 5.8, in the inset on the right. The temperature difference might be attributed to the installed resistance thermometer, which represents a heat leak due to its direct connection to higher lying stages.

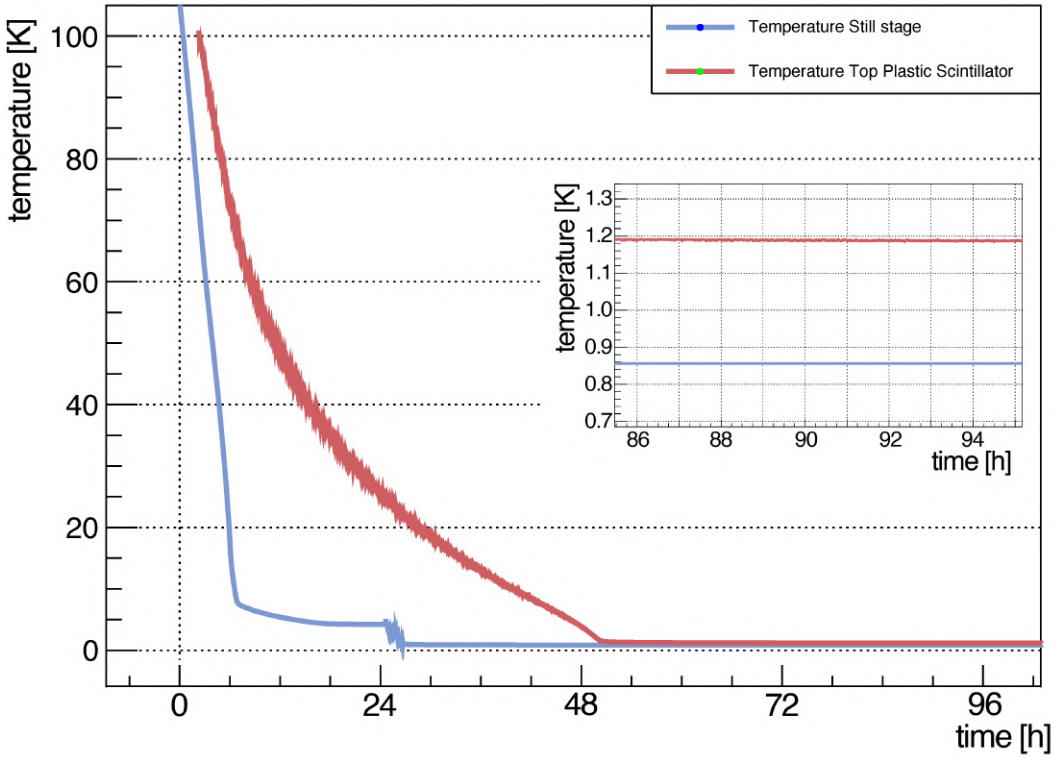

Figure 5.8.: *Temperature curves of the upper side of the cylindrical plastic scintillator (red) as well as of the Still stage itself (blue) during cool-down of the NUCLEUS cryostat. The time onset is defined when the Still stage reaches a temperature of $T_{Still} = 100\,K$. The Still stage reaches its base temperature of $T_{Still} \approx 0.86\,K$ within 27 h. After 6 h the cooling power of the Still stage reaches the range of the emitted power of the plastic scintillator, resulting in a significant decrease of cooling rate. After 25 h, mixing of ^3He and ^4He is initiated. The thermal equilibrium temperature of the plastic scintillator $T_{PS} \approx 1.19\,K$ is reached within 52 h. The insert shows the temperature difference between the Still stage and the thermalized plastic scintillator of $\Delta T = 0.33\,K$, which is likely due to a heat leak induced by the resistance thermometer, directly linking warmer stages.*

When applying these observations with a smaller-scale cylinder to a prediction of the thermalization behavior of the larger-scale NUCLEUS *Cryogenic Muon Veto*, equation 5.4 has to be recalled. Assuming reproducible thermal coupling and contact resistance in both cases, the difference in the thermalization time is manifested only with respect to the geometric properties. The remaining parameters of the equation can be assumed to be constant in both cases for this consideration, resulting in:

$$t = const \cdot \frac{m \cdot L}{A} \tag{5.7}$$

As the increase in mass m is to the same extent as the increase of the contact surface A when enlarging the radius of the cylindrical plastic scintillator to that of the larger-scale *Cryogenic Muon Veto*, the dependency of t is essentially on the height L of the cylinder. While the smaller-scale sample has a height of 42 mm, the NUCLEUS *Cryogenic Muon Veto* has a height of 50 mm, resulting in an increase of thermalization time of ∼19 %.

The findings can be transferred in an approximation to the polystyrene based plastic scintillator UPS 923-A, neglecting possible deviations in the heat capacity c and the thermal conductivity κ. As explained in Section 5.1.1, the polystyrene based plastic scintillator is expected to exhibit less critical cooling behavior than the polyvinyltoluene based one due to its simpler chemical structure. Although no temperature data were explicitly taken for the polystyrene based plastic scintillator UPS 923-A, conclusions can also be drawn indirectly from the cool-down of the respective prototype during the test with light read-out. When installed inside the NUCLEUS cryostat and cooled down to its operating temperature of ∼ 900 mK, no increase in the thermalization time of the Still stage occurred, which in turn could have been attributed to the emitted power of the plastic scintillator. This observation suggests that the thermalization time of the polystyrene based plastic scintillator UPS 923-A is comparable to that of the polyvinyltoluene based plastic scintillator EJ-204. In summary, this observation is completely reconcilable with the envisaged parameters of the NUCLEUS cryogenic infrastructure and confirms the feasibility of cooling down the NUCLEUS *Cryogenic Muon Veto* to its operating temperature on a reasonable time scale.

5.3.2. Scintillation Properties of the Polystyrene based Plastic Scintillator UPS-923A at Low-Temperatures

The light output of organic plastic scintillators was investigated for the muon veto prototype with the polystyrene based plastic scintillator UPS 923-A at liquid nitrogen and sub-Kelvin temperatures. Furthermore, the temperature-dependent change of the muon pulse shape was examined.

5.3.2.1. Muon Pulse Shape at 900 mK

A muon traversing the plastic scintillator induces the emission of around 10 photons by the plastic scintillator per keV energy deposition [94], depending on the specific chemical composition of the scintillator. These photons constitute the *light yield* of the plastic scintillator. A certain fraction of these generated photons (referred to as *light signal*) is collected by the WLS fibers and directed towards the SiPM. The photons are generating charge carriers in the active area of the SiPM and are amplified, resulting in an *analog signal*. The

digitization by an ADC eventually results in a digitized pulse of a certain amplitude and length, referred to as *digital signal*. Hence, the digital signal only indirectly reflects the light yield of the plastic scintillator itself. The naming of the signal at the different stages of the read-out process is indicated in the Figures 5.4 and 5.7. Two of these pulses with comparable amplitudes are exemplary shown in Figure 5.9, captured at room temperature (293 K) and at Still temperature (900 mK). In both measurements, the setup was installed inside the NUCLEUS cryostat under the same conditions. During the measurement at room temperature, however, the cryostat and in particular the pulse tube were switched off. During the measurement at Still temperature, the cryogenic system was fully operational. The peak values of the two selected pulses can be determined to be 119 mV and 115 mV, respectively. In the given example, the pulse decay time of the scintillator, which is defined as the time after which the pulse has returned to $1/e$ of its peak value increases from $t_{decay,\,293K} = 47$ ns at room temperature to $t_{decay,\,900mK} = 64$ ns at Still temperature.

The average values of the pulse decay time at room temperature and at Still temperature are determined to be $\bar{t}_{decay,\,293K} = (46.0 \pm 0.4)$ ns and $\bar{t}_{decay,\,900mK} = (60.7 \pm 3.4)$ ns, respectively. These were retrieved from a sample of 10 pulses with various amplitudes, several of which are shown in Appendix D.1. The pulse decay time therefore is observed to increase by $\sim 32\,\%$ when the plastic scintillator is operated at 900 mK compared to operation at room temperature. The average values of the pulse rise time are determined to be $\bar{t}_{rise,\,293K} = (30.1 \pm 1.0)$ ns and $\bar{t}_{rise,\,900mK} = (30.1 \pm 1.7)$ ns and thus agree in both measurements within the uncertainty. They are governed by the timing of the front-end electronics of the SiPM.

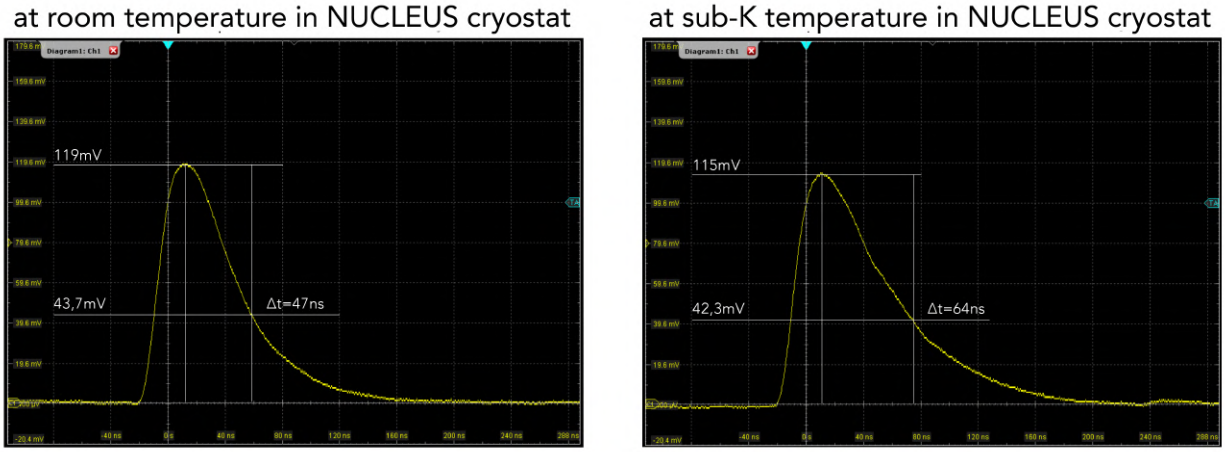

Figure 5.9.: *Exemplary muon pulses at room temperature 293 K (left) and at Still temperature 900 mK (right). The peak values of the two selected pulses can be determined to be 119 mV and 115 mV, respectively. The pulse decay time of the scintillator increases from $t_{decay,\,293K} = 47$ ns at room temperature to $t_{decay,\,900mK} = 64$ ns at Still temperature. Averaged for a number of pulses, it can be observed that the pulse decay time is enhanced by $\sim 32\,\%$ at sub-Kelvin temperature.*

5.3.2.2. Light Signal at 77 K and at 900 mK

The charge contained by each of the pulses, retrieved from the integration of the pulse over a certain interval, corresponds to the light signal of the muon veto prototype. If, in addition,

the prior light collection and light guidance process is taken into consideration and assumed to be constant, the charge represents an indirect measure of the scintillation light emitted by the plastic scintillator upon the passage of a muon (i.e. the light yield) and thus of the muons energy deposition. From the muon charge spectrum, information on the overall light output of the prototype can therefore be retrieved and compared for different measurements. In Figure 5.10, muon spectra which were taken with the muon veto prototype installed in the two compiled setups described above are presented. In Figure 5.10 (a) the spectrum at liquid nitrogen temperature (77 K) is shown and in Figure 5.10 (b) the spectrum at Still temperature (900 mK) is shown. Measurements at room temperature were taken as reference. Despite the different scaling of the charge axes (abscissas) arising from the use of two different data-acquisition systems, a comparison between the measurements can be obtained using these reference spectra. These were taken in each of the two setups under the same conditions as the corresponding measurements at low-temperatures. In the chosen visualization the spectra are all normalized to the acquisition time. Each spectrum features a pedestal together with a region for low energetic events (i.e. ambient gammas). The position and shape of the lower edge of this peak are determined by threshold effects and have no physical origin. At higher charges a plateau followed by a turning point corresponding to muon events becomes visible. This will be referred to as *muon peak*. The position and the characteristics of the muon peak are dictated by the light signal of the muon veto prototype. It is assumed that the turning point of the peak in the vicinity of the maximum can be approximated with a Gaussian-like shape. A local Gaussian-fit $f(x)$ shown in equation 5.8 provides the mean μ of the muon peak and the standard deviation σ, allowing to quantitatively compare the spectra taken at different temperatures. The resolution of the muon peak is defined as the ratio of the standard deviation σ to the mean μ and is a useful quantity to obtain information about the shape of the peak. The fitted muon peaks together with the corresponding fit parameters can be found in Appendix D.2.

$$f(x) = [constant] \cdot e^{-\frac{1}{2}\cdot\left(\frac{(x-\mu)}{\sigma}\right)^2} \tag{5.8}$$

The light signal of the muon veto prototype at liquid nitrogen temperature is the same with respect to the light signal at room temperature. The mean values of the muon peak can be determined to $\mu_{(a),\,293K} = (5.772 \pm 0.066) \cdot 10^3\, FADC\, a.u.$ at room temperature and $\mu_{(a),\,77K} = (5.787 \pm 0.042) \cdot 10^3\, FADC\, a.u.$ at liquid nitrogen temperature. The position of the muon peak is therefore the same for both measurements within the uncertainty. The resolution of the muon peak at room temperature can be calculated to $(\sigma\,/\,\mu)_{(a),\,293K} = (0.28 \pm 0.01)$ and at liquid nitrogen temperature to $(\sigma\,/\,\mu)_{(a),\,77K} = (0.30 \pm 0.01)$, agreeing within the uncertainty.

Interestingly, the light signal at sub-Kelvin temperatures is observed to increase significantly with respect to room temperature and to liquid nitrogen temperature. The mean values of the muon peak can be determined to $\mu_{(b),\,293K} = (3.602 \pm 0.300) \cdot 10^2\, Oscilloscope\, a.u.$ at room temperature and $\mu_{(b),\,900mK} = (5.265 \pm 0.333) \cdot 10^2\, Oscilloscope\, a.u.$ at Still temperature. The position of the muon peak is observed to shift by a factor of ~ 1.46 to higher values, indicating an enhanced light signal, consistent with the prolonged muon pulses. The resolution of the muon peak at room temperature can be calculated to $(\sigma\,/\,\mu)_{(b),\,293K} = (0.25 \pm 0.08)$ and at Still temperature to $(\sigma\,/\,\mu)_{(b),\,900mK} = (0.27 \pm 0.05)$ and is therefore observed to be temperature independent. The constancy of the resolution $\sigma\,/\,\mu$ indicates that the shape of the peak is not deformed.

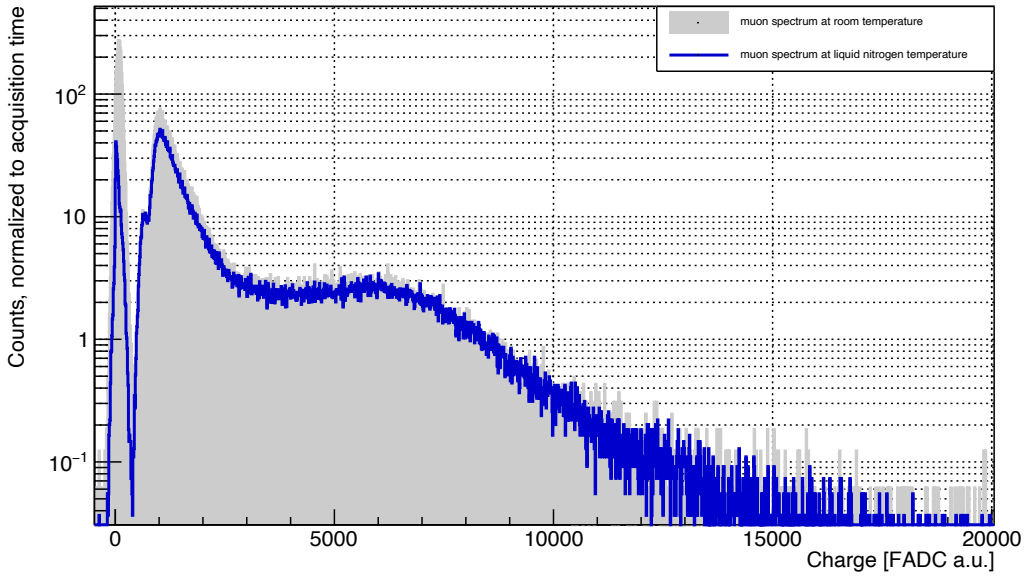

(a) Muon spectrum at room temperature 293 K (grey) and at liquid nitrogen temperature 77 K (blue).

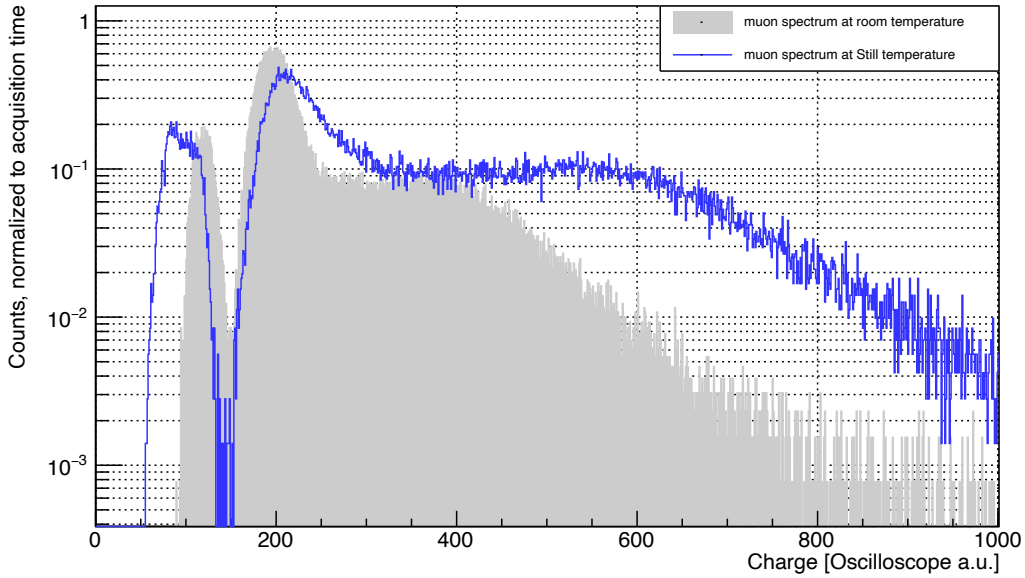

(b) Muon spectrum at room temperature 293 K (grey) and at Still temperature 900 mK (blue).

Figure 5.10.: *Muon spectra of the polystyrene based plastic scintillator UPS923-A at liquid nitrogen temperature 77 K (a) and at Still temperature 900 mK (b). The reference spectra at room temperature are shown in grey. Each spectrum features a pedestal together with a peak for low energetic events (i.e. ambient gammas). At higher charges a plateau followed by a turning point corresponding to muon events becomes visible. Different scaling of the charge axes (abscissas) results from the use of two different data acquisition systems. The position of the muon peak at sub-Kelvin temperatures is observed to shift by a factor of* ~ 1.46 *to higher values with respect to the measurement at room temperature, hinting towards an enhanced light output of the muon veto prototype at sub-Kelvin temperatures.*

5.4. Discussion of the Observations of the Experimental Investigation

The observations described above constitute, to the best of the author's knowledge, the first reported measurements of organic plastic scintillators at sub-Kelvin temperatures. Their detailed discussion is therefore imperative. A key question is whether the observed increase of digital signal output is because more scintillation light is produced by the plastic scintillator (i.e. the light yield is increased) or because more of the scintillation light is collected and detected (i.e. the increase can hardly be attributed to an individual component, but rather to the system as a whole).

The setups described in Section 5.2 have the advantage that any temperature-related dependencies of the SiPM can be excluded for the interpretation of these observations. Thus, it is assumed that all temperature dependencies should be present prior to the conversion of the light signal to the analog signal. Nevertheless, the muon veto prototype detector (with the polystyrene based plastic scintillator, four WLS fibers and additional reflective foil) includes a variety of components that could be (partly) responsible for the increase of light signal. The literature review in Section 5.1 has shown conclusively that a negative temperature dependence of organic scintillators has already been observed and described numerous times. When attempting a physics interpretation, the observed change in muon pulse shape can be of assistance in this respect. The observed increase in pulse decay time of $\sim 32\,\%$ might point towards a temperature dependence of triplet state de-excitations. These processes are delayed and are therefore expected to be responsible for the shape of the muon pulse tail. Another possible scenario explaining the observations consists in an increase of the attenuation length of the plastic scintillator. This would lead to an increase of the flux of collected photons. Furthermore, assuming multiple reflections of the photons within the plastic scintillator prior to their collection, the generated photons would be collected over a longer period of time and thus result in an increase of pulse decay time.

Nevertheless, no conclusive interpretation of the light yield temperature dependence of organic plastic scintillators can be drawn based on the observations presented. Further measurements are necessary for a more profound conceptual understanding. In this regard, the measurements are planned to be repeated with a well understood FADC in order to further examine the discrepancies in the pedestal between the two spectra in Figure 5.10 (b). In order to describe the evolution of the temperature dependence of the light yield, additional temperatures would need to be investigated. In addition to the measurements at 77 K (where the light signal of the muon veto prototype still agrees with that at room temperature) and 900 mK (where the light signal of the muon veto prototype is enhanced by 46 % with respect to that at room temperature), the NUCLEUS cryostat could also be thermalized in between at 50 K and at 4 K. In order to disentangle possible superimposed temperature effects of the individual components, it is essential to examine individually their response to low-temperatures. Eventually, the described setup provides an elegant way to systematically study the temperature dependence of the light yield of different organic plastic scintillators.

In conclusion, the experimental investigation of the low-temperature behavior of organic plastic scintillators has clearly verified the key physical aspects of the intended NUCLEUS *Cryogenic Muon Veto* detector concept. It has been demonstrated that organic plastic scintillators can be cooled to sub-Kelvin temperatures on a time scale compatible with the

parameters of the NUCLEUS cryogenic infrastructure. The functionality of the scintillation process of organic plastic scintillators at sub-Kelvin temperatures has been confirmed. For this purpose, a setup to study the interesting phenomenology of organic plastic scintillators at sub-Kelvin temperatures has been established, allowing future investigations of the temperature dependence of the light yield. In addition, the final detector concept was successfully commissioned in the framework of the presented measurements. Both the seamless operation of the SiPM on the bottom of the 300 K plate as well as the viable guidance of the WLS fiber through the NUCLEUS cryostat mark milestones in the development of the NUCLEUS *Cryogenic Muon Veto*. The respective details are presented in the following Chapter 6.

6. Development of the NUCLEUS Cryogenic Muon Veto

Contents

6.1. Description of the Design of the NUCLEUS Cryogenic Muon Veto

The underlying idea of the NUCLEUS *Cryogenic Muon Veto* together with the groundwork and the theoretical foundations for its development have been previously introduced in Section 3.1. It consists of the innovative concept of an organic plastic scintillator based muon veto, operating inside the NUCLEUS cryostat underneath the mixing chamber at sub-Kelvin temperatures. It has been designed to fully comply with the general constraints and requirements on the overall NUCLEUS muon veto detailed in Section 2.4.2.

The NUCLEUS *Cryogenic Muon Veto* is composed of a disc with a total diameter of 297 mm and a height of 50 mm, made out of the polystyrene based plastic scintillator UPS 923-A. The emitted scintillation light is caught by in total nine light-guiding fibers BCF-91A with a cross-sectional area of 1 mm x 1 mm each and guided towards the top of the cryostat. A SiPM KETEK PE3325-WB-TIA-TP is installed inside the cryostat at the bottom of the 300 K plate reading out the light signal.

The design of the NUCLEUS *Cryogenic Muon Veto* was fully conceived within the frame of this thesis and was shaped by considerations regarding the integration of the whole system with the cryogenic infrastructure of NUCLEUS. The results of the efficiency study presented in Chapter 4, in which various positions of the plastic scintillator disc were examined, as

well as the insights from the investigation of the properties and characteristics of organic plastic scintillators at low-temperatures presented in Chapter 5 formed the basis for the development. Both approaches had yielded important conclusions and results that were incorporated into the design and development process, and will be crosslinked respectively.

6.1.1. Design of Plastic Scintillator Disc UPS923-A

In order to maximize the collection efficiency of the scintillation light by the wavelength shifting fibers and to simultaneously prevent any detachment of the fibers, their affixation to the plastic scintillator needs to be thoroughly assured. Due to spatial constraints inside the cryostat dictated by the distance of 11 cm between the mixing chamber of the NUCLEUS cryostat and the upper edge of the mechanical support structure of the passive shielding, the design needs to be kept as compact as possible.

A solution that features several bended grooves inside the cylindrical plastic scintillator which guide the fibers through the plastic was therefore realized. It is shown schematically in Figure 6.1. The fibers guided in these grooves are foreseen to run on the bottom of the disc and are then directed in a curved way to the top, leaving the plastic scintillator at the edge of the top side. The curved fiber guidance in the interior of the plastic scintillator leads to an enlargement of the contact area between fiber and plastic and thus to an enhancement of the light collection efficiency. The length of each of the straight grooves on the bottom of the disc (96.25 mm) together with the length of the bend (79.96 mm) adds up to a total groove length of 173.21 mm, whereas each of the nine wavelength shifting fibers is attached to the plastic with three of its sides. These two segments of the grooves are shown in Figure 6.2 in more detail. The realization of the fiber curvature in the inside of the plastic scintillator furthermore saves space and gives stability to the fibers. The selected fibers BCF-91A have a cross-sectional area of 1.0 mm x 1.0 mm and were cut to a length of 1.5 m. The radius of curvature of the groove of 49 mm corresponds to the minimum permitted radius of curvature of the fiber without significant light losses occurring [97]. The cross-section of the grooves is with 1.2 mm x 1.2 mm slightly larger than that of the fibers, to allow adhesive to be inserted.

The disc's outer diameter of 297 mm was chosen to match the diameter of the mechanical support structure and thermal bath, i.e. the copper disc shown in Figure 6.4. The height of 50 mm, matching the height of the plastic scintillator panels composing the *Outer Muon Veto*, is a compromise between minimizing the required thermalization time (see Section 5.3.1) and maximizing the discrimination power between muon and electron signals (see Section 6.3.2). The inner hole with a diameter of 45 mm is required for the feed-through of the detector support structure. The overall mass of the plastic scintillator disc can be determined to be $\sim$3.6 kg.

The decision to instrument the polystyrene based plastic scintillator UPS 923-A instead of the previously for the *Outer Muon Veto* established polyvinyltoluene based plastic scintillator BC-408 mainly rests upon the successful demonstration of the functionality of the scintillation process at sub-Kelvin temperatures in Chapter 5, specifically for the polystyrene based plastic scintillator UPS 923-A. The light yield of UPS 923-A is with 60 % of anthracene [95] only slightly lower than that of BC-408 with 64 % of anthracene [84]. Besides, the decision was also based on economic reasons.

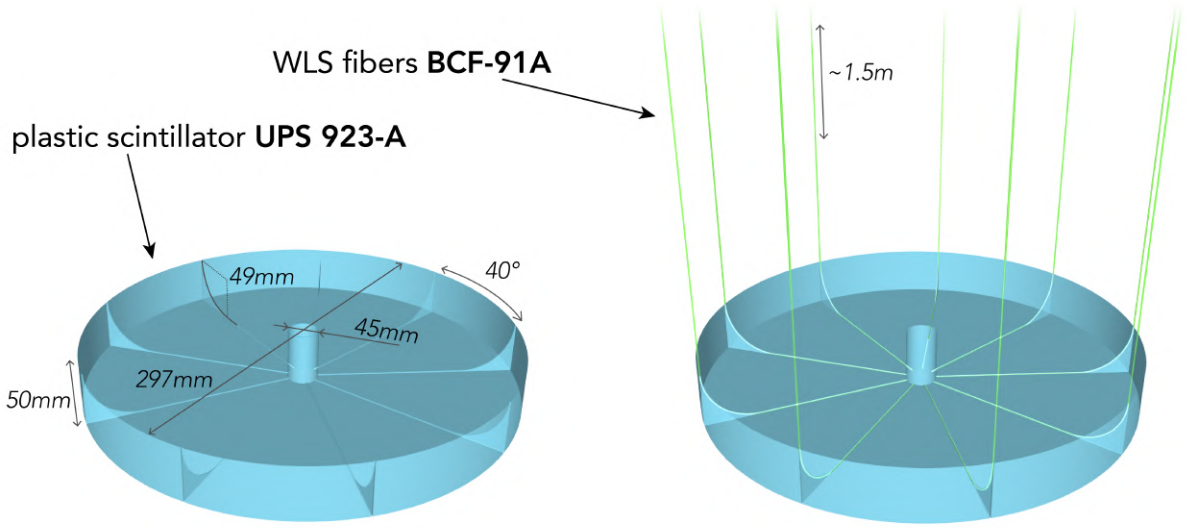

Figure 6.1.: *Design overview of the plastic scintillator disc of the Cryogenic Muon Veto without (left) and with (right) WLS fibers attached. The intended design of the plastic scintillator UPS 923-A features a cylindrical shape with a diameter of 297 mm and a height of 50 mm. The inner hole, required for the feed-through of the detector support structure, has a diameter of 45 mm. A total of nine bended grooves are foreseen for the attachment of the WLS fibers BCF-91A, each of which is machined into the plastic at every angle of 40°. The fibers are fixed to the grooves with adhesive and have a length of ∼ 1.5 m each.*

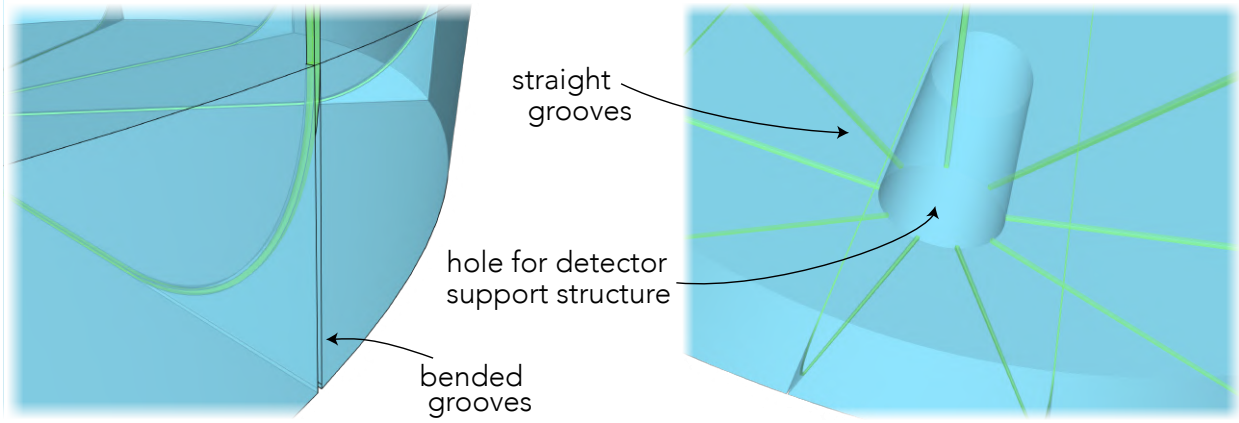

Figure 6.2.: *Zoom-in on the bended part of the fiber grooves (left) and the straight part (right). The WLS fibers are foreseen to be guided in these grooves on the bottom of the disc and then directed in a curved way to the top, leaving the plastic scintillator at the edge of the top side. The length of the straight groove on the bottom of the disc is 96.25 mm and the length of the bend is 79.96 mm, adding up to a total groove length of 173.21 mm. Each fiber has one open end towards the hole for the feed-through of the detector support structure.*

6.1.2. Positioning of the SiPM inside the NUCLEUS Cryostat

The SiPM of the *Cryogenic Muon Veto* is attached to the bottom of the 300 K plate and can thus be operated at constant room temperature. A literature study on the low-temperature behavior of SiPMs (which is presented in Appendix C) showed that the operation of SiPMs at temperatures below ~ 80 K is subject to numerous uncertainties and is therefore not to be favored in the context of the given cryogenic infrastructure. For instance, the exponential increase of the quenching resistor in the temperature range from 290 K to 80 K [105] - leading to a significantly longer signal decay time and hence to pile-up - seems to be a critical factor that would require in-depth investigation.

The feasibility of the SiPM positioning in the upper part of the NUCLEUS cryostat and the associated guidance of the WLS fibers through the cryostat vessels have been successfully demonstrated in the frame of the experimental setup for the prototype measurements, described in Section 5.5. A picture of the SiPM attached to the 300 K plate with the coupled fibers can be seen in Figure 5.6. A PVC-casing encapsulating the SiPM has been designed for the attachment to the 300 K plate. It is schematically shown in Figure 6.3. The casing can be fixed flexibly to the 300K plate, and includes a rectangular opening on the side for signal and bias cable feed-through. A custom-fit connector bundling the WLS fibers can be mounted on the active surface of the SiPM.

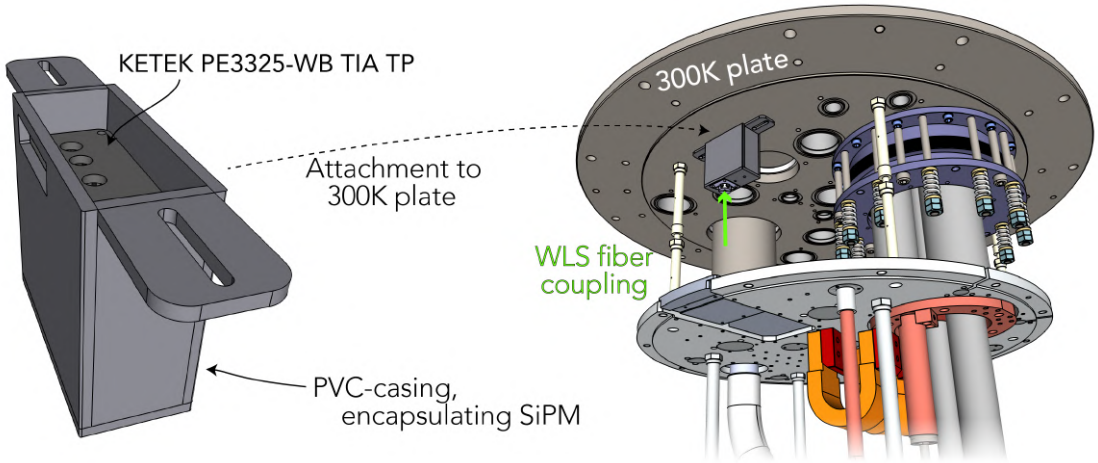

Figure 6.3.: *The KETEK SiPM module PE3325-WB TIA TP of the Cryogenic Muon Veto is attached to the bottom of the 300 K plate. For this purpose, a PVC-casing encapsulating the SiPM module has been designed. This positioning, which allows for operation of the SiPM at constant room temperature, has been successfully demonstrated in the frame of the experimental setup for the prototype measurements, described in Section 5.5. The PVC-casing includes an opening on the side for signal and bias cable feed-through and foresees the optical coupling of the WLS fibers to the active surface of the SiPM via a custom-fit connector.*

The selected KETEK SiPM module PE3325-WB TIA TP [73] is characterized by two main features which were decisive for its choice. On the one hand, the module enables pre-amplification of the initial analog SiPM signal via a transimpedance amplifier. Such an early signal amplification is essential to mitigate the introduction of noise from lengthy signal cables. Due to the large distance required between the cryostat and the data-acquisition system in the VNS of $\mathcal{O}(1\,\mathrm{m})$, this pre-amplification is ideally implemented within the front-

end electronics of the SiPM. On the other hand, the featured gain-stabilization of the module allows to alleviate the influence of potential temperature fluctuations of $\mathcal{O}(1\,\mathrm{K})$ of the 300 K plate during cryostat operation on the SiPM. The slight temperature dependence of the SiPMs' gain (which for the KETEK PE3325-WB is specified to $\sim 0.3\,\%/\mathrm{K}$ at an overvoltage of $V_{OV} = 5\,\mathrm{V}$) can automatically be compensated through an integrated gain stabilization. The chosen KETEK modules feature a small analog temperature sensor, which compensates the change of the breakdown voltage of the SiPM ($\sim 22\,\mathrm{mV/K}$). The constant overvoltage thus leads to a constant gain. The SiPMs are operated with a power supply input of +5 V, and a tunable bias voltage control in the range from 0 V to +1 V.

6.1.3. Installation of the Plastic Scintillator Disc inside the NUCLEUS Cryostat

The mechanical setup for the installation of the *Cryogenic Muon Veto* inside the NUCLEUS cryostat underneath the mixing chamber plate has not been conceived within the scope of this work, but by R. Cerulli et al. at INFN Roma. A recent overview can be found in [106]. The copper disc shown schematically in Figure 6.4 serves both as support structure and thermal bath for the plastic scintillator disc of the NUCLEUS *Cryogenic Muon Veto*. It is part of the overall mechanical support structure for the inner (active and passive) shielding, which has been previously introduced and described in Figure 5.1. Three tie rods made out of kevlar connect the copper disc with the spring tube of the NUCLEUS cryostat. An additional thermal link to the Still plate, presumably in the form of a copper wire, is mounted for the thermalization of the copper disc at $T_{Still} \sim 900\,\mathrm{mK}$.

The production and commissioning of this mechanical support structure for the inner shielding, and thus also the final installation and operation of the *Cryogenic Muon Veto* inside the NUCLEUS cryostat, is the next step yet to come.

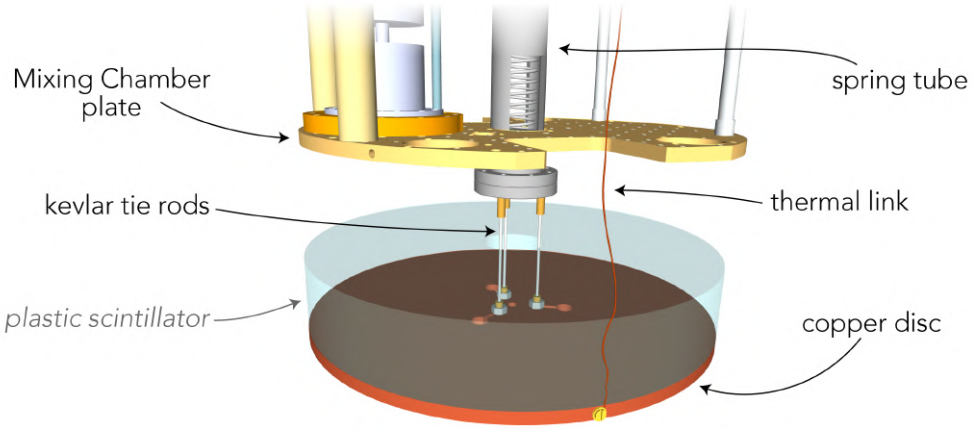

Figure 6.4.: *Installation of the Cryogenic Muon Veto inside the NUCLEUS cryostat underneath the mixing chamber plate. A copper disc, part of the overall mechanical support structure for the inner shielding, is connected via three kevlar tie rods to the spring tube. It serves both as support structure and thermal bath for the plastic scintillator disc (displayed transparently for better view of the copper disc) of the NUCLEUS Cryogenic Muon Veto. A copper wire thermally links the copper disc with the Still plate.*

6.2. Production of the NUCLEUS Cryogenic Muon Veto

The production of the NUCLEUS *Cryogenic Muon Veto* was carried out in the facilities of the *Technical University of Munich*. The individual components were purchased from the manufacturers and, if required, machined by the mechanical workshop of the *Chair for Experimental Astroparticle Physics*. Components, which are not commercially available, were also commissioned to the workshop for production. The individual steps of the detector assembly, which are detailed in the Appendix E, were performed by the author of this thesis. Pictures of the final plastic scintillator disc UPS 923-A can be seen in Figure 6.5. On the left, the disc is shown after machining by the workshop, featuring nine bended grooves and a hole for the feed-through of the detector support structure. On the right, the disc is shown after gluing the WLS fibers BCF-91A. The applied adhesive is the two component clear epoxy resin BC-600 [107].

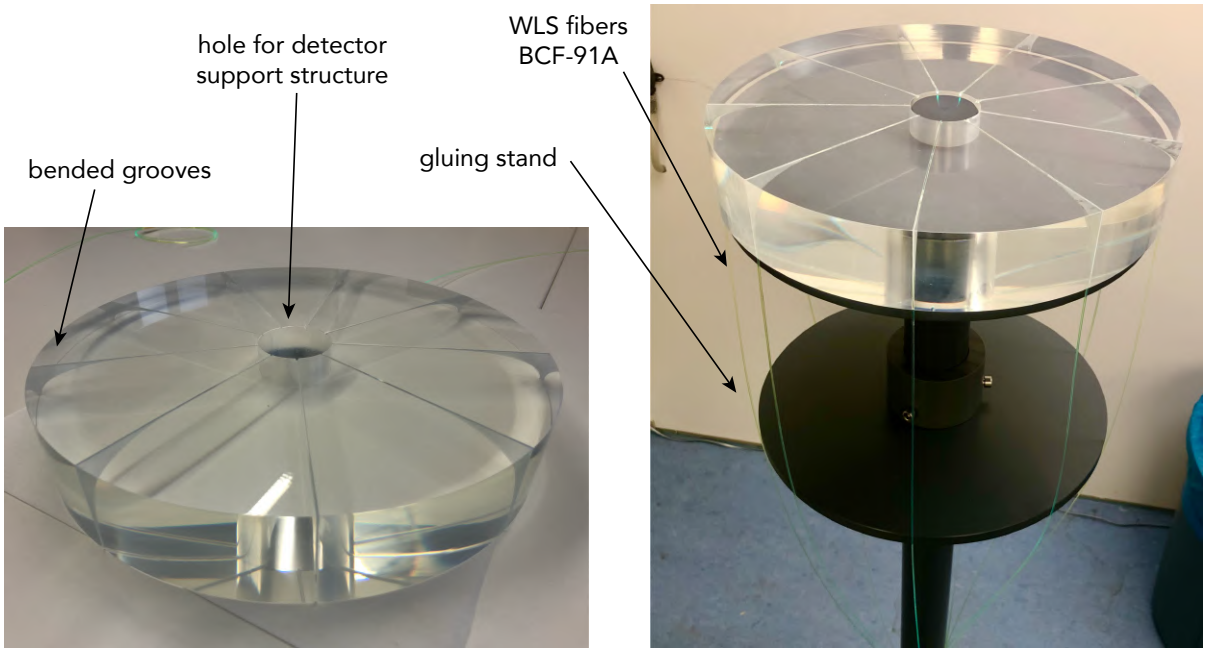

Figure 6.5.: *Pictures of the final plastic scintillator disc UPS 923-A after machining by the workshop (left) and after the attachment of the WLS fibers BCF-91A (right). The disc features nine bended grooves, into which the fibers are glued with the two component clear epoxy resin BC-600. For the gluing process, a purpose-built gluing stand was utilized. In both pictures, the disc is lying upside down.*

6.3. Measurements with the NUCLEUS Cryogenic Muon Veto at Room Temperature

6.3.1. Description of the Experimental Setup

For the first commissioning of NUCLEUS *Cryogenic Muon Veto*, the plastic scintillator detector developed throughout this thesis was operated at room temperature in the underground-laboratory of the *Technical University of Munich*. The experimental setup used for this purpose is shown in Figure 6.6. The assembled plastic scintillator disc with attached WLS fibers, together with the SiPM is mounted inside a light-tight darkbox. Two additional muon veto plastic scintillator panels read-out by photomultiplier tubes are installed underneath and on top of the darkbox allowing for coincidence measurements. The reflectivity of the surfaces adjacent to the plastic scintillator anticipated in the cryostat are considerably affecting the collection efficiency of the scintillation light. In order to realistically recreate these surrounding surfaces, also for the measurements at room temperature, the disc is placed on top of a sheet of copper, mimicking the copper disc shown in Figure 6.4. In addition, the top and side surfaces of the plastic scintillator are covered with highly reflective polyester foil (for further information see Appendix E.4). The use of this foil is also intended for the final operation of the *Cryogenic Muon Veto* inside the NUCLEUS cryostat.

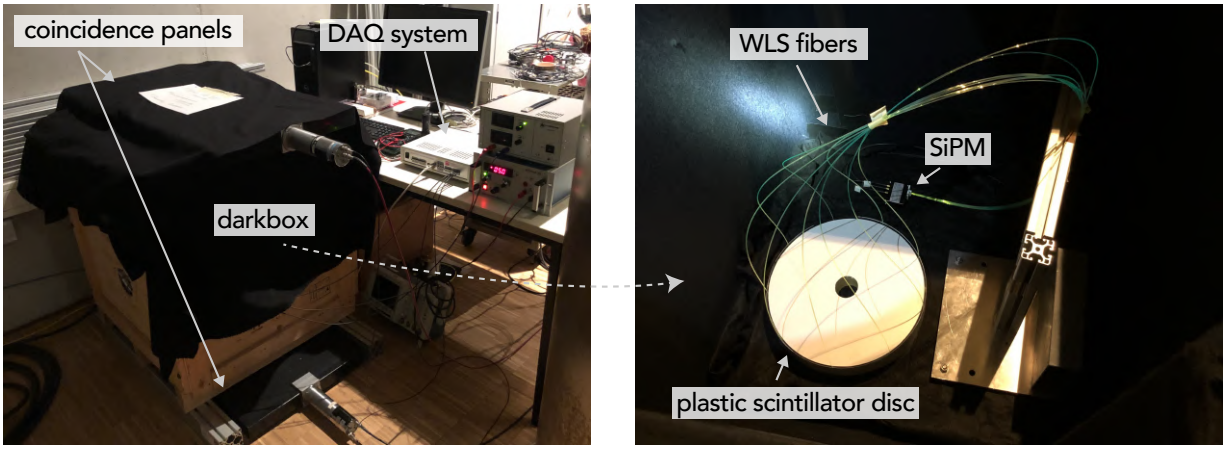

Figure 6.6.: *Picture of the experimental setup (left) for the commissioning of the NUCLEUS Cryogenic Muon Veto at room temperatures. The assembled plastic scintillator disc with attached WLS fibers is mounted inside a light-tight darkbox together with the SiPM (right). The plastic scintillator sits upon a copper sheet and is covered by highly reflective polyester foil, in order to realistically recreate the reflectivity of the surfaces adjacent to the plastic scintillator inside the NUCLEUS cryostat. To allow coincidence measurements, two additional muon veto plastic scintillator panels were installed below and above the darkbox.*

The electronic data-acquisition system compiled for the first commissioning of the assembled plastic scintillator disc at room temperature is schematically shown in Figure 6.7. A pre-amplified and gain-stabilized KETEK PE3325-WB TIA TP SiPM module was used to read-out the light signal. For analog-to-digital conversion of the signal a STRUCK SIS3316 flash-ADC was used [108], which is the module foreseen for the final muon signal conversion

during the operation of the NUCLEUS experiment. At this point it should be particularly emphasized that in the course of the measurements presented below, the final detector concept of the NUCLEUS *Cryogenic Muon Veto* has been successfully operated in its entirety for the first time. The resulting light signal of the assembled plastic scintillator disc was converted by the final SiPM (i.e. a KETEK PE3325-WB-TIA-TP) into an analog signal, which was digitized by the final flash-ADC (i.e. a STRUCK SIS3316).

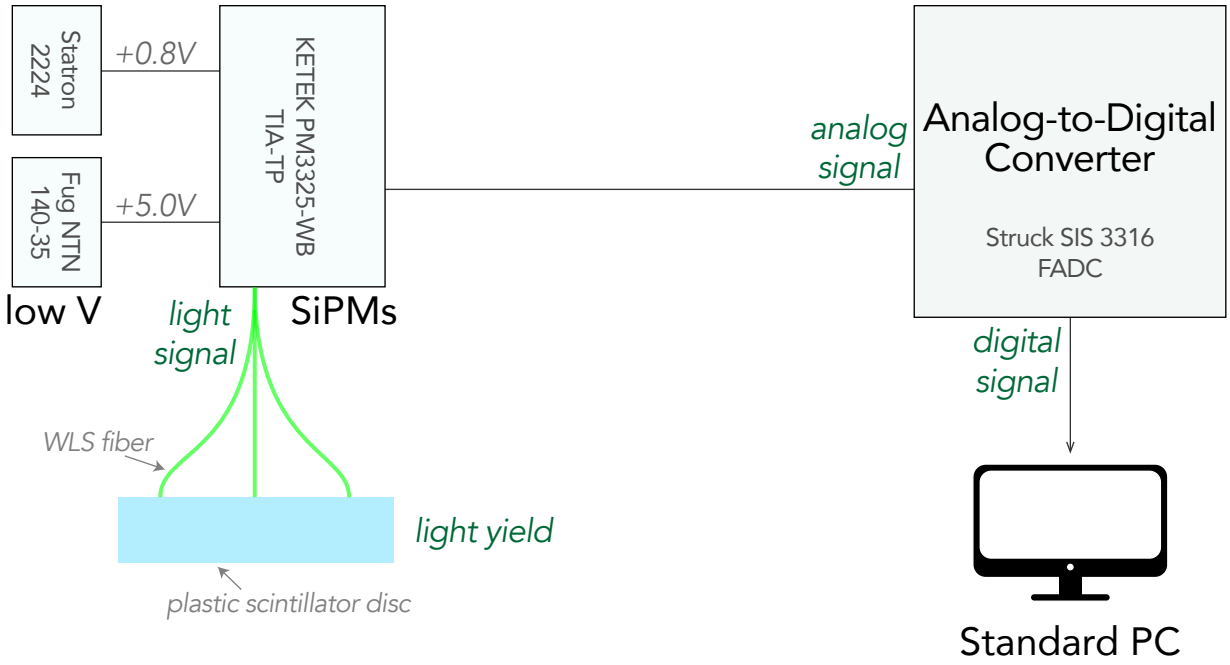

Figure 6.7.: *Wiring scheme of the data-acquisition system and the gain-stabilized SiPM KETEK PE3325-WB TIA TP, which was compiled for the first commissioning of the assembled plastic scintillator disc at room temperature. The SiPMs require two separate bias supplies - a main power supply input of 5 V and a gain control voltage, tunable between 0 V and 1 V. The light signal of the plastic scintillator disc is converted into an analog signal by the SiPM, pre-amplified and directly sent to the analog-to-digital converter, which in this case was the final flash-ADC of the NUCLEUS muon veto, i.e. a STRUCK SIS3316. The digital signal is then provided for further analysis. The plastic scintillator is shown in blue and the WLS fibers in green. With this arrangement, the final detector concept of the NUCLEUS Cryogenic Muon Veto has been successfully operated in its entirety for the first time.*

6.3.2. Results of the Measurements

Muon Spectrum

In Figure 6.8, two muon charge spectra which were taken with the plastic scintillator disc operating at room temperature inside a darkbox are presented. In the chosen visualization the spectra are normalized to the acquisition time. The scaling of the charge axis (abscissa) is characteristic of the STRUCK SIS3316 flash-ADC and is therefore given in arbitrary units. Two different spectra are shown in the plot, which were obtained by applying

different coincidence criteria to the read-out of the plastic scintillator disc. The coincidence search explained schematically in Figure 6.9 is based on the fact that muons are high enough in energy to penetrate multiple plastic scintillator panels. Gammas, on the contrary, are stopped by a single panel and thus cannot produce coincident events. A three-fold coincidence criterion applied to the plastic scintillator disc implies that the disc is only read out when both external panels are triggered in addition to the disc. From such a criterion, a restriction to solely muon events is the consequence. The resulting spectrum is shown in red in Figure 6.8 and a corresponding muon track is shown schematically in orange in Figure 6.9. A two-fold coincidence criterion applied to the plastic scintillator disc implies that the disc is always read out when at least both external panels are triggered. Whenever the triggering muons do not happen to pass through the disc, randomly captured background events are the consequence. The resulting spectrum is shown in grey in Figure 6.8 and a corresponding muon track is shown schematically in blue in Figure 6.9. The spectrum features a region for low energetic background events (i.e. ambient gammas). As previously explained in Section 5.3.2.2, the position and shape of the lower edge of this peak are due to threshold effects. The muon peak located at higher charges stands out from the background more distinctly compared to the measurements with the smaller-scale prototype shown in Figure 5.10. The reason for this can be attributed to the reduced dimensions (primarily the smaller height) of the prototype.

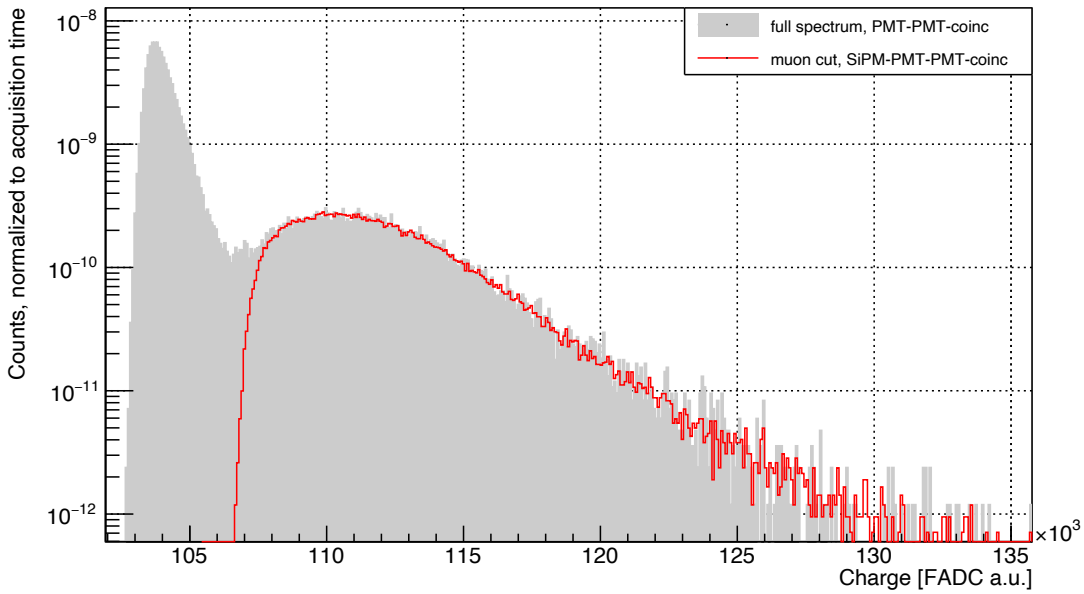

Figure 6.8.: *Muon spectra of the plastic scintillator disc operating at room temperature inside a darkbox. Two spectra with different coincidence criteria applied are shown. The spectrum in grey corresponds to a two-fold coincidence between the two external plastic scintillator panels (PMT-PMT coincidence) and features a region for low energetic events (i.e. ambient gammas). The lower edge of this peak is shaped by threshold effects. At higher charges, a peak corresponding to muon events becomes visible. The spectrum shown in red corresponds to a three-fold coincidence between the two external plastic scintillator panels and the disc (SiPM-PMT-PMT coincidence) and is restricted exclusively to these muon events. The presented spectra represent the first commissioning of the NUCLEUS Cryogenic Muon Veto at room temperature.*

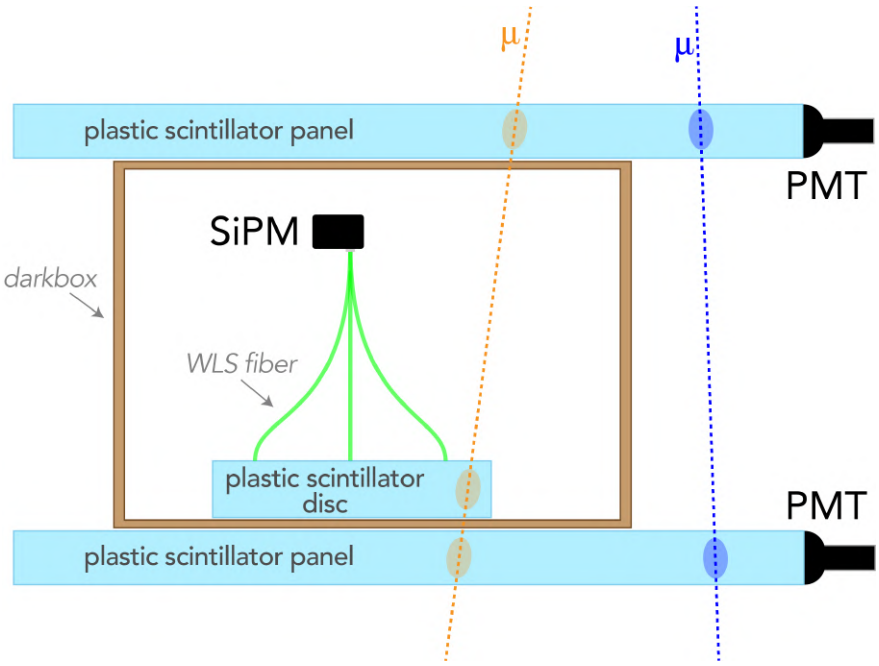

Figure 6.9.: *Schematic visualization of the coincidence search. The plastic scintillator disc is installed inside a light-tight darkbox, shown in brown. Two additional muon veto plastic scintillator panels are installed below and above the darkbox and allow for coincidence measurements. These panels are instrumented with photomultiplier tubes (PMT). Depending on the spectrum of interest, different coincidences were applied in the context of the presented measurements. A three-fold coincidence (muon track in orange) between the two panels and the disc allows a restriction to muon events only. A two-fold coincidence (muon track in blue) between the two panels allows to read both muon events and randomly captured background events.*

Identification of the Muons

In order to unambiguously identify the muons ascertained to the events in the three-fold coincidence spectrum (red) in Figure 6.8, they can be juxtaposed with the coincident muons registered by one of the plastic scintillator panels. Since these panels are constituent parts of a well-established muon veto, which is currently being re-commissioned as part of the work of L. Klinkenberg, such a comparison can be considered as reliable. For this purpose, a scatter plot between the two-fold coincidence spectrum of the plastic scintillator panel (indicated with *PMT*) and the three-fold coincidence spectrum of the plastic scintillator disc (indicated with *SiPM*) is shown in Figure 6.10. For simplified visibility of the underlying scattering structure, the corresponding muon spectra are plotted as projections on the respective sides. A region of overlap clearly emerges in the scatterplot. Assuming that the events registered by the panel can be uniquely identified as muons, this identification can be extended by means of the three-fold coincidence condition to the events registered by the plastic scintillator disc of the NUCLEUS *Cryogenic Muon Veto*.

The the two-fold coincidence rate registered by the plastic scintillator panels is 7.48 Hz, whereas the three-fold coincidence rate registered by the plastic scintillator disc can be determined to be 1.49 Hz. These two values are compatible, taking into account the geometry-related angle distribution of the muons and the difference between the dimensions of the disc and the panel. A thesis by R. Burkhardt [109], in which the muon flux within the

underground-laboratory of the *Technical University of Munich* was measured, provides comparable values for a similar two-fold coincidence setup with two plastic scintillator panels.

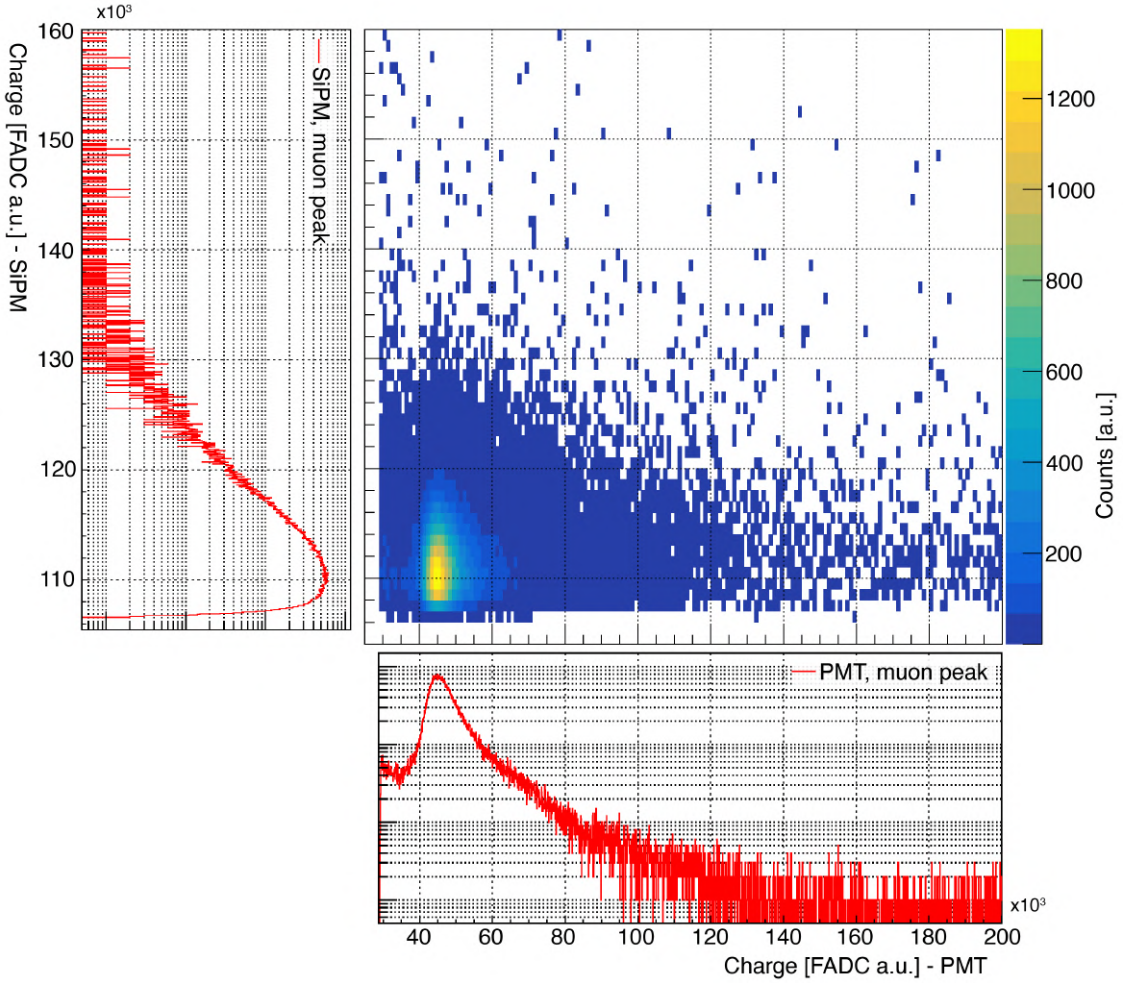

Figure 6.10.: *Scatter plot between the two-fold coincidence spectrum of the plastic scintillator panel (indicated with PMT) and the three-fold coincidence spectrum of the plastic scintillator disc (indicated with SiPM). The corresponding muon spectra are plotted as projections on the respective sides. The spectrum of the plastic scintillator disc (SiPM) is the same as shown in Figure 6.8 in detail. The spectrum of the plastic scintillator panel (PMT) was taken with a panel of a well-established muon veto. By applying the criterion of the required three-fold coincidence, the region of overlap clearly emerging in the scatterplot allows for unambiguous identification of the muons in the spectrum taken with the plastic scintillator disc of the NUCLEUS Cryogenic Muon Veto.*

Peak to Valley Ratio

To roughly evaluate the discrimination capability of the NUCLEUS *Cryogenic Muon Veto* between muons and gammas, a relative comparison with one of the established muon veto panels can be carried out. As previously described in Section 2.4.2, this discrimination capability is crucial to minimize false veto signals induced by gammas and at the same time maximize the muon detection efficiency. For a quantification of this parameter, the *Peak to Valley Ratio* is of use, which relates the maximum of the muon peak to the minimum of the

valley between muon and low energetic events. The framework for determining the *Peak to Valley Ratio* was implemented by L. Klinkenberg.

The values of the maximum of the peak and the minimum of the valley were determined via fits of the corresponding ranges. The muon peak was fitted using a Landau-fit. The reason for the choice of a Landau fit is due to the fact that the Bethe-Bloch formula predicts a Landau-distributed spectrum upon the passage of muons through matter [110]. Unlike in Section 5.3.2.2, the muon spectra taken with the larger-scale plastic scintillator disc features a peak sufficiently distinct to derive its actual shape. The valley was fitted, due to lack of prior knowledge, with a fourth-degree polynomial, yielding a fit accuracy which was considered to be sufficient for the purpose of this rough evaluation.

Figure 6.11 shows the spectra featuring a muon peak together with the low energetic gamma events, both taken with the plastic scintillator panel (left) and the plastic scintillator disc (right). The applied Landau-fit of the muon peak is shown in black and the fit of the valley with a fourth-degree polynomial is shown in red. The *Peak to Valley Ratio* of the plastic scintillator panel can be calculated to $(P\,/\,V)_{panel} = (2.114 \pm 0.289)$ and of the plastic scintillator disc to $(P\,/\,V)_{disc} = (2.147 \pm 0.362)$. The *Peak to Valley Ratio* of the disc is therefore consistent with that of the panel, indicating that the discrimination capability of the two systems is comparable.

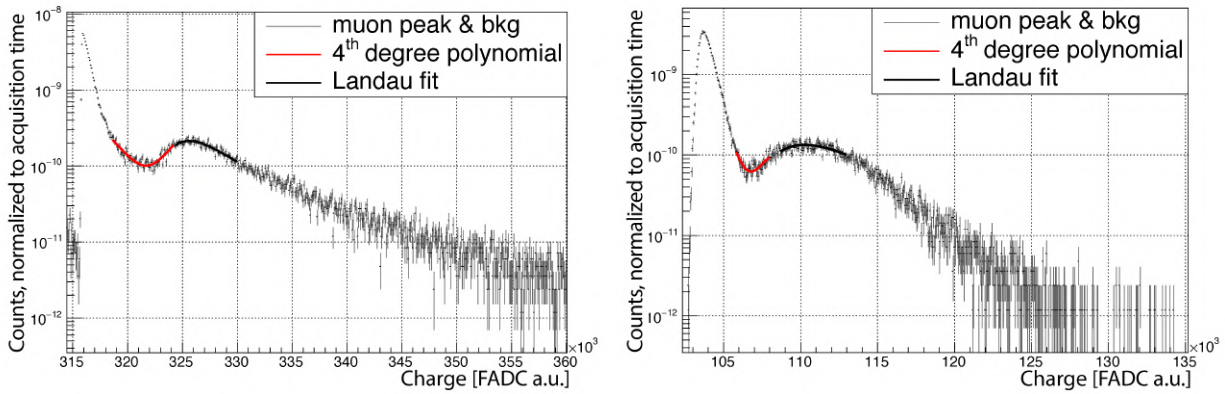

Spectrum with Plastic Scintillator Panel *Spectrum with Plastic Scintillator Disc*

Figure 6.11.: *Determination of the Peak to Valley Ratio of the muon charge spectra taken with the plastic scintillator panel (left) and the plastic scintillator disc (right). Both spectra feature a peak for low energetic events, a muon peak and an intermediate valley. The ratio of the minimum of this valley to the maximum of the muon peak is a measure for the discrimination capability of the respective muon detector. The required values were determined via fits of the corresponding ranges. The muon peak was fitted using a Landau-fit and the valley using a fourth-degree polynomial. The Peak to Valley Ratio of the plastic scintillator panel can be calculated to* $(P\,/\,V)_{panel} = (2.114 \pm 0.289)$ *and of the plastic scintillator disc to* $(P\,/\,V)_{disc} = (2.147 \pm 0.362)$*. The discrimination ability of the two systems is therefore expected to be comparable.*

6.3.3. Discussion of the Results of the Measurements

The overall detector concept of the NUCLEUS *Cryogenic Muon Veto* has been commissioned and validated for the first time during the above-presented measurements with the plastic scintillator disc at room temperature. Within the course of these measurements, muon events could be unambiguously identified. Moreover, the discrimination capability of the NUCLEUS *Cryogenic Muon Veto* between muons and gammas was found to be comparable to that of a well-established muon veto. The viability of operating the plastic scintillator detector developed throughout this thesis as an efficient and reliable muon veto within the NUCLEUS experiment has thus been demonstrated. The first operation of the *Cryogenic Muon Veto* in coincidence with the *Outer Muon Veto* is planned for the blank assembly of the NUCLEUS experiment to be conducted in Munich in the course of the coming year [111].

7. Conclusion and Outlook

The coherent elastic neutrino-nucleus scattering (CEνNS) is a type of neutrino coupling that has been cleanly predicted by the Standard Model since the 1970s, but came into the focus of dedicated experimental investigation only recently. It is a threshold-less neutral-current interaction in which an antineutrino scatters off a nucleus elastically. Thus, CEνNS offers the unique possibility to probe the Standard Model at very low energies, promising not only the completion of the picture of the fundamental neutrino couplings predicted, but also to expand our knowledge about fundamental neutrino properties. Nuclear fission reactors constitute one of the main experimental sites in the search for this type of interaction, emitting reactor antineutrinos with an average energy as low as 1.5 MeV and a resulting flux as high as $8 \cdot 10^{20}\,\bar{\nu}_e/(\mathrm{s{\cdot}cm^2})$.

The NUCLEUS collaboration is developing a new-generation experiment to probe CEνNS, exploiting gram-scale ultra-low threshold cryogenic detectors. For the installation of the NUCLEUS experiment, a compact 24 $\mathrm{m^2}$ room situated in the basement of a five-story office building on the area of the Chooz nuclear power plant is being prepared. The commercial power plant features two N4-type pressurized water reactors, each running at a nominal thermal power of 4.25 GW_{th}. One of the challenges, however, that goes along with the installation of a neutrino experiment at a shallow experimental site close to nuclear reactors are the above-ground background conditions. Operating at an overburden of only $\mathcal{O}$(1 m.w.e.), muon-induced events are expected to be the dominant source of background. In the case of NUCLEUS, this challenge shall be tackled with a highly efficient muon veto with a muon detection efficiency of more than 99 %, consisting of a compact cube assembly of 24 plastic scintillator panels.

Nevertheless, this design does not achieve complete coverage of all the $4\,\pi$ steradians of solid angle around the NUCLEUS target detector. Inevitably, a large unshielded area remains in the upper side of the experiment, where the cryostat containing the NUCLEUS detector and its support structure will be inserted. Due to the characteristic angular $\cos^2\theta$ distribution of atmospheric muons, the coverage of this area is expected to be particularly important towards achieving the envisaged muon detection efficiency. The urgency of a technical solution to tag these muons passing through this critical area is apparent. The proposal to build an additional, umbrella-like active muon veto covering this unshielded area together with the NUCLEUS cryostat from above is not preferable, due to the spatial constraints of the experimental site and in order to not further increase the detector dead time. For this reason, a novel and innovative concept, consisting of a plastic scintillator based disc-shape active muon veto operating inside the NUCLEUS cryostat at sub-Kelvin temperatures, has been investigated and developed within the frame of the presented thesis.

Due to the lack of experimental studies of the scintillation mechanism of organic plastic scintillators at low-temperatures in literature, a fundamental proof-of-concept was indispensable in order to confirm the general feasibility of this approach. This led, to the best of the authors' knowledge, to the first reported measurements of organic plastic scintillators at sub-Kelvin temperatures. These measurements not only demonstrated that organic plastic scintillators can be cooled to sub-Kelvin temperatures on a time scale compatible with the

parameters of the NUCLEUS cryogenic infrastructure, but also confirmed the functionality of the principal scintillation process of organic plastic scintillators at sub-Kelvin temperatures.

Based on these results, it was then possible to proceed with the design and the assembly of the so called NUCLEUS *Cryogenic Muon Veto*. This was done according to the detector concept of the NUCLEUS *Outer Muon Veto*, which was already established at that time. The R&D process of the NUCLEUS *Cryogenic Muon Veto* was primarily determined by considerations regarding the integration of the plastic scintillator disc, equipped with wavelength shifting fibers and a silicon photomultiplier, with the cryogenic infrastructure of NUCLEUS. It is foreseen to install a disc of the polystyrene based plastic scintillator UPS 923-A with an outer diameter of 297 mm and a height of 5 mm underneath the mixing chamber plate of the NUCLEUS cryostat, sitting on top of a mechanical support structure thermalized at ~ 900 mK. In total, nine wavelength shifting fibers running in bended grooves through the interior of the plastic scintillator are used to guide the scintillation light through the cryostat vessels towards the SiPM. The pre-amplified and gain-stabilized SiPM will be mounted on the bottom of the 300 K plate, thus operating at constant room temperature.

Two crucial milestones of the R&D process conducted throughout this work consist in the commissioning of various components of the NUCLEUS *Cryogenic Muon Veto*, which altogether allowed the validation of the detector concept as a whole.

- In a first step, several key detector components of the NUCLEUS *Cryogenic Muon Veto* were installed and operated successfully inside the cryostat. Even though only a smaller-scale plastic scintillator was used, the feasibility of the SiPM mounting in the inside of the cryostat and the associated fiber guidance was demonstrated. This clearly showed that the operation of an organic plastic scintillator based muon veto inside a running dry dilution refrigerator is feasible.
- In a second step, the larger-scale plastic scintillator disc with fibers attached was commissioned at room temperature. This measurement, in which the final data-acquisition system (i.e. a KETEK PE3325-WB TIA TP and a STRUCK SIS3316) has been operating as an ensemble, validated the chosen detector design. The recorded muon charge spectrum allows a clear identification of the muon events and features sufficient discrimination capability between muons and gammas.

The successful validation of the detector concept of the NUCLEUS *Cryogenic Muon Veto* is essential for the performance of the overall NUCLEUS muon veto, and thus for the NUCLEUS experiment. The efficiency study performed within the frame of this thesis assigned the NUCLEUS *Cryogenic Muon Veto* a key role towards achieving the targeted muon detection efficiency of $> 99\,\%$. Furthermore, the increase in the cosmic muon count rate from 673.1 Hz to 676.5 Hz upon installation of the NUCLEUS *Cryogenic Muon Veto* is negligible. Thus, no major impact on the detector dead time is to be expected. Another important result of the efficiency study concerns the non-detected stopping muons within the passive shielding. These muons are especially harmful to the NUCLEUS operation, since they can potentially induce secondary particles, representing background events originating in the direct vicinity of the NUCLEUS target detector. The NUCLEUS *Cryogenic Muon Veto* was found to suppress the number of non-detected stopping muons by a factor of ~ 2.1. If Geant4 muon simulations would indicate that the installation of the NUCLEUS *Cryogenic Muon Veto* does still not sufficiently mitigate the influence of the non-detected stopping muons, a supplementary component has been proposed within the scope of this work. It is a *Hollow Cylindrical Muon Veto* designed in a way to minimize the impact of

the unavoidable gap, where the vessels of the NUCLEUS cryostat enter the shielding. With this component, the number of non-detected stopping muons could be reduced by another factor of ~ 1.38.

The groundwork for a straightforward installation and operation of the *Cryogenic Muon Veto* inside the NUCLEUS cryostat has therefore been laid within the frame of the presented thesis. However, the final installation of the detector inside the cryostat is still pending. For this purpose, the mechanical support structure for the inner shielding, that is currently still under development, is foreseen to be used. In the meantime, a detailed characterization of the NUCLEUS *Cryogenic Muon Veto* at room temperature is scheduled. The first deployment of the *Cryogenic Muon Veto* in coincidence with the *Outer Muon Veto* is planned for the blank assembly and commissioning of the NUCLEUS experiment, which will be carried out in Munich during the coming year.

As an interesting side-result, this work opens the path for a new line of research to investigate the temperature dependence of plastic scintillators. Within the context of the measurements of organic plastic scintillators at sub-Kelvin temperatures, the decay time of the muon pulses was observed to increase by $\sim 32\,\%$ and the light signal of the muon veto prototype was found to be enhanced by $\sim 46\,\%$ with respect to that at room temperature. These observations hint towards a negative temperature dependence of the light yield of the polystyrene based plastic scintillator UPS 923-A, whose conclusive interpretation falls beyond the scope of this work. Further measurements will be performed for their detailed understanding. With the established setup to study the phenomenology of organic plastic scintillators at sub-Kelvin temperatures, an accurate and systematic characterization of the temperature dependence of the plastics' scintillation light yield in the range from 50 K down to 0.8 K will be possible in the future.

A. Geometrical Simulations of the NUCLEUS Muon Veto

Components	Volumes	Shape	Dimension
Side Muon Veto Panel, left	plastic scintillator panel	cuboidal	dx_side = 5 cm dy_side = 28.25 cm dz_side = 96.0 cm
	plastic scintillator panel	cuboidal	dx_side = 5 cm dy_side = 28.25 cm dz_side = 96.0 cm
	plastic scintillator panel	cuboidal	dx_side = 5 cm dy_side = 28.25 cm dz_side = 96.0 cm
	plastic scintillator panel	cuboidal	dx_side = 5 cm dy_side = 28.25 cm dz_side = 96.0 cm
Side Muon Veto Panel, right	plastic scintillator panel	cuboidal	dx_side = 5 cm dy_side = 28.25 cm dz_side = 96.0 cm
	plastic scintillator panel	cuboidal	dx_side = 5 cm dy_side = 28.25 cm dz_side = 96.0 cm
	plastic scintillator panel	cuboidal	dx_side = 5 cm dy_side = 28.25 cm dz_side = 96.0 cm
	plastic scintillator panel	cuboidal	dx_side = 5 cm dy_side = 28.25 cm dz_side = 96.0 cm
Bottom Muon Veto Panel	plastic scintillator panel	trapezoidal rectangular edge	dx1_bott_1 = 12.90 cm dx2_bott_1 = 13.55 cm dy_bott = 125 cm dz_bott = 5 cm
	plastic scintillator panel	trapezoidal	dx1_bott_2 = 30.28 cm dx2_bott_2 = 28.96 cm dy_bott = 125 cm dz_bott = 5 cm
	plastic scintillator panel	trapezoidal	dx1_bott_2 = 28.96 cm dx2_bott_2 = 30.28 cm dy_bott = 125 cm dz_bott = 5 cm
	plastic scintillator panel	trapezoidal rectangular edge	dx1_bott_1 = 13.55 cm dx2_bott_1 = 12.90 cm dy_bott = 125 cm dz_bott = 5 cm

(continues on next page)

Components	Volumes	Shape	Dimension
Top Muon Veto Panel	plastic scintillator panel	trapezoidal rectangular edge	dx1_top_1 = 24.90 cm dx2_top_1 = 25.55 cm dy_top = 125 cm dz_top = 5.0 cm
	plastic scintillator panel	trapezoidal with hole	dx1_top_2 = 30.28 cm dx2_top_2 = 28.96 cm dy_top = 125 cm dz_top = 5.0 cm r_max_hole = 43.0 cm
	plastic scintillator panel	trapezoidal with hole	dx1_top_2 = 28.96 cm dx2_top_2 = 30.28 cm dy_top = 125 cm dz_top = 5.0 cm r_max_hole = 43.0 cm
	plastic scintillator panel	trapezoidal rectangular edge	dx1_top_1 = 25.55 cm dx2_top_1 = 24.90 cm dy_top = 125 cm dz_top = 5.0 cm
Front Muon Veto Panel	plastic scintillator panel	cuboidal	dx_front = 120.0 cm dy_front = 5.0 cm dz_front = 24.125 cm
	plastic scintillator panel	cuboidal	dx_front = 120.0 cm dy_front = 5.0cm dz_front = 24.125 cm
	plastic scintillator panel	cuboidal	dx_front = 120.0 cm dy_front = 5.0 cm dz_front = 24.125 cm
	plastic scintillator panel	cuboidal	dx_front = 120.0 cm dy_front = 5.0 cm dz_front = 24.125 cm
Rear Muon Veto Panel	plastic scintillator panel	cuboidal	dx_rear = 120.0 cm dy_rear = 5.0 cm dz_rear = 24,125 cm
	plastic scintillator panel	cuboidal	dx_rear = 120.0 cm dy_rear = 5.0 cm dz_rear = 24.125 cm
	plastic scintillator panel	cuboidal	dx_rear = 120.0 cm dy_rear = 5.0 cm dz_rear = 24,125 cm
	plastic scintillator panel	cuboidal	dx_rear = 120.0 cm dy_rear = 5.0 cm dz_rear = 24.125 cm

(continues on next page)

Components	Volumes	Shape	Dimension
Inner Active Shielding	plastic scintillator disc	cylinder	r_max = 15.0 cm dz_disc = 5.0 cm
Passive Shielding	lead cube	hollow cube with hole	dx_lead = 93.5 cm dy_lead = 93.0 cm dz_lead = 86.0 cm thickness_lead = 5.0 cm r_max_hole = 43.0 cm
	polyethylene cube	hollow cube with hole	dx_pe = 83.5cm dy_pe = 83.0 cm dz_pe = 76.0 cm dx_thickness = 20.25 cm dy_thickness = 20.0 cm dz_thickness = 16.5 cm r_max_hole = 43.0 cm
Inner Passive Shielding	lead disc	cylinder	r_max = 15.0 cm dz_disc = 5.0 cm
	polyethylene disc	cylinder	r_max = 15.0 cm dz_disc = 16.5 cm

Table A.1.: *List of NUCLEUS shielding components, implemented using TGeometry for the muon track simulations. The single NUCLEUS components are composed of several volumes, which all exhibit a defined shape and specific dimensions.*

	ϕ_{veto}	ϕ_{stop_μ}	$\phi_{stop\_\mu\_PS}$	$\phi_{stop\_\mu\_Pb}$	$\phi_{stop\_\mu\_PE}$	$\phi_{ND\_stop\_\mu}$	$\phi_{ND\_stop\_\mu\_PS}$	$\phi_{ND\_stop\_\mu\_Pb}$	$\phi_{ND\_stop\_\mu\_PE}$
No Cryogenic Muon Veto									
	673.1	45.8	3.4	30.0	12.4	2.68	0.071	1.47	1.14
Cryogenic Muon Veto									
z = 0 cm	676.5	46.0	3.5	30.2	12.3	1.25	0.0386	0.757	0.459
z = -2 cm	676.5	45.7	3.5	29.9	12.2	1.21	0.0359	0.726	0.452
z = -4 cm	677.1	45.5	3.4	29.9	12.2	1.18	0.051	0.728	0.399
z = -6 cm	676.1	45.9	3.4	30.2	12.3	1.23	0.0359	0.746	0.444
Additional Hollow Cylindrical Muon Veto									
h = 10 cm *(z = 0 cm)*	678.1	45.8	3.4	30.3	12.2	0.913	0.0317	0.536	0.346
h = 10 cm *(z = -2 cm)*	676.9	45.8	3.5	30.1	12.1	0.997	0.0393	0.602	0.356
h = 10 cm *(z = -4 cm)*	677.3	46.1	3.5	30.3	12.3	0.981	0.0366	0.595	0.35
h = 10 cm *(z = -6 cm)*	676.8	46.1	3.4	30.4	12.3	1.04	0.0393	0.622	0.378
h = 20 cm *(z = 0 cm)*	677.8	45.9	3.4	30.5	12.1	0.755	0.0255	0.437	0.292
h = 30 cm *(z = 0 cm)*	679.3	46.3	3.5	30.6	12.3	0.681	0.0193	0.399	0.263

Table A.2.: *Simulated muon fluxes through the NUCLEUS experiment, together with the number of stopping muons. The values in the table are based on the energy deposition of the muons inside the plastic scintillator volumes with applied track-length threshold of 2.5cm and are given in units of muons / seconds. The chosen abbreviations of the listed parameters refer to the following physical quantities: $\phi_{fictitious}$ denotes the muon flux through the fictitious volume, ϕ_{veto} the muon flux through plastic scintillator volumes, ϕ_{stop_μ} the flux of muons stopping inside the experimental arrangement and $\phi_{ND\_stop\_\mu}$ the flux of muons, which stop inside the experimental arrangement and are not detected by any plastic scintillator volume. The indices PS, Pb and PE specify in which of the materials the muons stop.*

B. Thermal Expansion Coefficients

Materials	Thermal Expansion Coefficients
Silicon Photomultiplier	
Silicon	$2.6 \cdot 10^{-6} \, / \, K$
Fused Silica	$0.55 \cdot 10^{-6} \, / \, K$
Acrylic Plastic	$68 \text{-} 75 \cdot 10^{-6} \, / \, K$
Copper	$16.0 \text{-} 16.6 \cdot 10^{-6} \, / \, K$
Wavelength Shifting Fiber	
Polystyrene	$70 \cdot 10^{-6} \, / \, K$
Acrylic Plastic	$68 \text{-} 75 \cdot 10^{-6} \, / \, K$
Plastic Scintillator	
Polyvinyltoluene	$78 \cdot 10^{-6} \, / \, K$
Polystyrene	$70 \cdot 10^{-6} \, / \, K$
Optical Cement BC-600	$72 \cdot 10^{-6} \, / \, K$

Table B.1.: *Thermal Expansion Coefficients of various Components of the NUCLEUS Cryogenic Infrastructure. All values are taken from [112] and the respective data sheets.*

C. Expected Low-Temperature Behavior of Silicon Photomultipliers

The performance of the various SiPM characteristics discussed in Section 3.3.2 will be examined below for low-temperatures, based on a literature review. A special focus is thereby put on the KETEK PM3325-WB SiPM series [73] that is particularly relevant for this work.

Gain The slight temperature dependence of the SiPMs gain, resulting from the temperature dependence of the photo-diode's capacitance C, can be compensated by adjusting the overvoltage V_{OV}. KETEK indicates for the PM3325-WB SiPM a gain variation of $\sim 0.3\,\%/\mathrm{K}$ at an overvoltage of $V_{OV} = 5\,\mathrm{V}$. In practice, this dependence is often automatically compensated by the SiPMs through an integrated gain stabilisation. KETEK, for instance, offers modules (PE3325-WB TIA TP [73]) with a small analog temperature sensor, which compensates the change of the breakdown voltage of the SiPM ($\sim 22\,\mathrm{mV/K}$). The constant overvoltage thus leads to a constant gain.

Pulse shape In order to address the change of the single-photon pulse shape of SiPMs exposed to low-temperatures, the single-photon pulse shape at room temperature, which is shown in the Figure 3.8, shall be recalled. For the considerations at this point it is crucial to recognise the correspondence of the slow signal recovery component to the recharge of the photo diode through the quenching resistor. E. Engelmann [105] studies the behavior of KETEK PM3325-WB SiPMs at liquid argon temperatures. He finds an exponential temperature dependence of the quenching resistor, which in case of KETEK SiPMs is fabricated out of polysilicon. In the range from 290 K to 80 K the resistance is measured to increase by a factor of 12.80 ± 0.14 from $(0.38 \pm 0.03)\,\mathrm{M\Omega}$ to $(5.39 \pm 0.04)\,\mathrm{M\Omega}$. An increase in the value of the quenching resistor, however, is accompanied by a change in the pulse shape. J. Csáthy et al. [113] study the properties of SiPMs in a cryogenic environment (at liquid argon temperatures) and report a significant increase of the decay time of the slow recovery component. Furthermore, they observe the pulse at low-temperature to start with a sharp peak and to feature an amplitude that is 4 to 5 times smaller than at room temperature. From this important finding it is concluded that the total charge contained in a one pixel pulse for a fixed overvoltage is the same at liquid argon temperature and at room temperature. As a consequence, the use of charge sensitive ADCs would provide sufficient information about the energy of the pulses.

Breakdown voltage The gain mechanism in the constituent APDs of SiPMs is the impact ionization of Silicon atoms in the avalanche section of the depletion region. As seen in Section 3.3.2, charge carriers gain energy from the electric field and subsequently ionize Silicon atoms in a collision. Thus, the created electron-hole pairs can trigger an avalanche of charge carriers by impact ionization. The mobility of the charge carriers, however, decreases with decreasing temperature and their scattering off the crystal lattice therefore becomes less likely [75]. The lower the temperature, the lower is the rate of non-ionizing collisions and, as a result, the higher is the average energy of the accelerated charge carriers. Hence, the probability of impact ionization not only depends on the strength of the electric field, but also on the temperature. Nevertheless, the impact of the higher ionization rates at

low-temperatures can be adjusted by decreasing the reverse bias. The breakdown voltage is therefore expected to be a function of the temperature.

Dark counts The dark count rate of a SiPM depends not only on the size of its active area and the applied overvoltage, but also sensitively on the temperature. The number of thermally generated electrons, which are produced in different quantum mechanical processes (for additional information see [75,105]) decreases significantly with decreasing temperature. As a result, a SiPM which is being operated at low-temperatures generates considerably less noise.

After-pulse rate For the afterpulsing probability E. Engelmann [105] finds a linear increase with decreasing temperature in the range from 290 K down to 180 K. This behavior can be explained by the temperature dependence of the quenching resistor and the variation of the release time of the trapped charge carriers. In this temperature range, the change of release time of the trapped charge carriers with temperature is larger than the change of decay time τ_{decay} of the signal recovery component. For this reason the occurrence of the afterpulses is shifted to larger delay times, increasing the probability of inducing non-negligible afterpulse due to the increased amount of charge per afterpulse. In the range from 180 K to 80 K the afterpulsing probability is expected to slightly decrease again, as due to an inversed behavior of the change of release time of the trapped charge carriers and the change of decay time τ_{decay} of the signal recovery component, the occurrence of the afterpulses is being shifted to shorter delay times. Engelmann however finds out that for the KETEK PM3325-WB SiPMs a net increase in afterpulsing probability of about 20% is to be expected when cooling the SiPM down from room temperature to liquid argon temperature.

Optical crosstalk The dependence of the optical crosstalk probability on the temperature for a fixed overvoltage V_{OV} will be mostly determined by the dependence of the photo-diode's capacitance with the temperature. This effect, however, is expected to be negligible. Engelmann [105] confirms this theoretical consideration and finds for the KETEK PM3325-WB SiPM an averaged constant optical crosstalk probability of $(19.7 \pm 1.3)\,\%$ for the temperature range 300 K to 150 K at an overvoltage of 4 V.

Conclusions

As a consequence of these insights from the literature study regarding the low-temperature behavior of Silicon Photomultipliers it was concluded that - because many of the SiPM parameters are critically affected by low-temperatures - the overall performance of the SiPMs is expected to deteriorate. Even though the use of SiPMs at liquid argon temperatures has previously been described many times in the literature, the operation of SiPMs at sub-Kelvin temperatures has so far been subject to countless uncertainties. For instance, the exponential increase of the quenching resistor in the temperature range from 290 K to 80 K - leading to a significantly longer signal decay time and hence to pile-up - seems to be a critical factor that would require in-depth investigation. In the frame of the NUCLEUS *Cryogenic Muon Veto* it was therefore decided to position the SiPM on the lower side of the 300K plate inside the NUCLEUS cryostat. This ensures the flawless operation of the SiPM at room temperature and is effortlessly possible due to the high flexibility of the wavelength shifting fibers. Since the considerations regarding the low-temperature behavior of SiPMs are thus not of immediate relevance to this work, the corresponding chapter is being presented in the Appendix.

D. Scintillation Properties of the Polystyrene based Plastic Scintillator UPS-923A at Low-Temperatures

D.1. Muon Pulse Shape

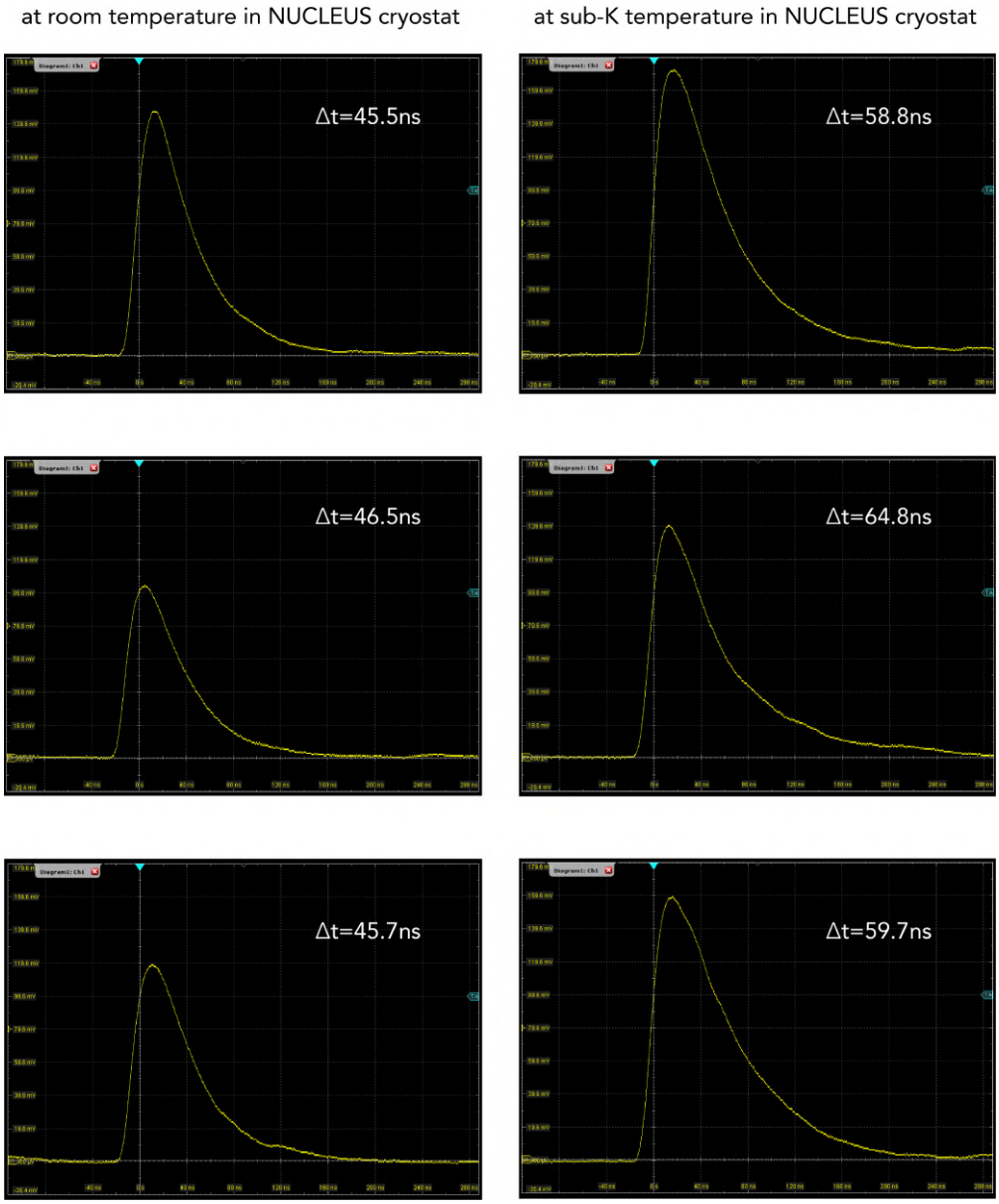

Figure D.1.: *Selection of muon pulses at room temperature and at Still temperature.*

D.2. Fitted Muon Spectra

Plastic Scintillator Installation in LN Dewar,
Muon Spectrum at 293K

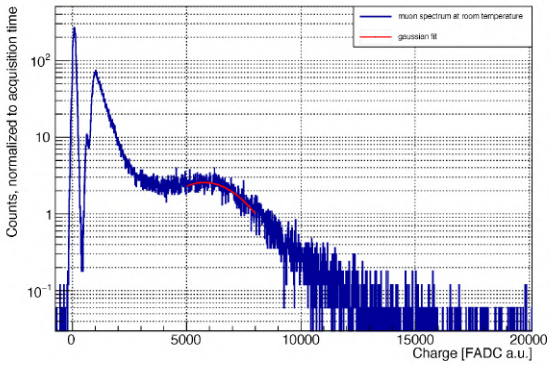

FIT PARAMETER

NO.	NAME	VALUE	ERROR
1	Constant	2.56699e+00	3.38366e-02
2	Mean	5.77174e+03	6.61863e+01
3	Sigma	1.62797e+03	7.18758e+01

Plastic Scintillator Installation in LN Dewar,
Muon Spectrum at 77K

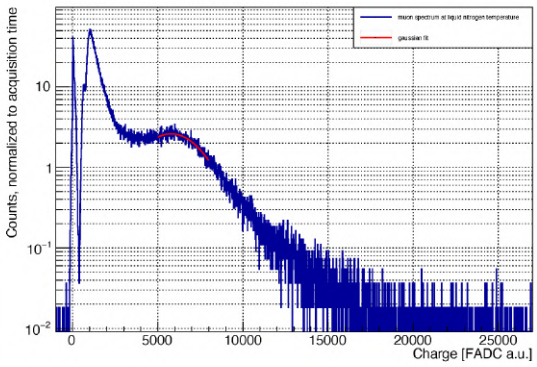

FIT PARAMETER

NO.	NAME	VALUE	ERROR
1	Constant	2.61224e+00	1.86947e-02
2	Mean	5.78739e+03	4.16346e+01
3	Sigma	1.78426e+03	4.92406e+01

Plastic Scintillator Installation in NUCLEUS Cryostat,
Muon Spectrum at 293K

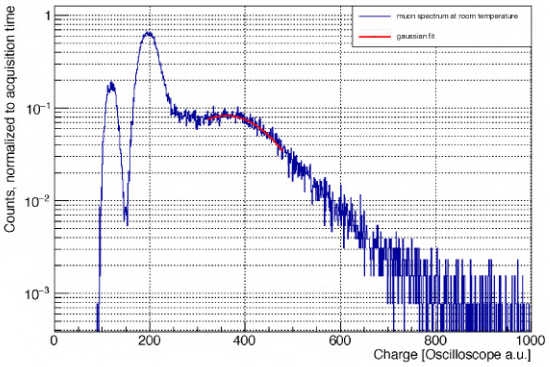

FIT PARAMETER

NO.	NAME	VALUE	ERROR
1	Constant	8.28105e-02	8.90804e-03
2	Mean	3.60204e+02	3.00176e+01
3	Sigma	8.95902e+01	2.96998e+01

Plastic Scintillator Installation in NUCLEUS Cryostat,
Muon Spectrum at 900mK

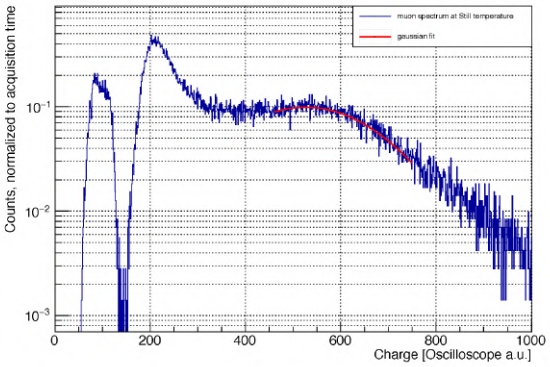

FIT PARAMETER

NO.	NAME	VALUE	ERROR
1	Constant	9.89843e-02	8.11928e-03
2	Mean	5.26507e+02	3.32881e+01
3	Sigma	1.42176e+02	2.75538e+01

Figure D.2.: *Locally fitted muon peaks and corresponding fit parameters.*

E. Production of the NUCLEUS Cryogenic Muon Veto

E.1. Feasibility Verification of the Cutting of the Grooves

The design of the plastic scintillator disc presented in Section 6.1.1 features nine bended grooves in the interior of the plastic. These could not be produced by the manufacturer itself, but were incorporated by the mechanical workshop of the *Chair for Experimental Astroparticle Physics*. Prior to the machining of the final disc, several test cuts were made in advance to verify the feasibility and to establish a seamless process.

E.2. Investigation of Adhesive-Performance

For the gluing of the fibers to the smaller-scale prototypes, the single component cyanoacrylate adhesive Loctite 406 [102] was used. Its suitability for cryogenic applications was verified beforehand. After some time, visible deteriorations of the plastic at the glue points became apparent. Saint Gobain thereupon confirmed that single component cyanoacrylate adhesives contain solvents which attack polyvinyltoluene. For this reason, the more suitable two component clear epoxy resin BC-600 [107] was applied for the assembly of the NUCLEUS *Cryogenic Muon Veto*.

Furthermore, a small plastic scintillator sample with a glued-in fiber was subjected to a cool-down in the cryostat. This was to verify that the grooves with glued-in fiber do not run the risk of breaking or degrading due to mechanical stress. An image of the small sample with a single fiber attached to the groove can be seen in Figure E.1.

Figure E.1.: *Image of the small sample with a single fiber attached to the groove. The cool-down of this sample in the cryostat served to verify that the grooves with glued-in fiber do not run the risk of breaking or degrading due to mechanical stress.*

E.3. Disc-Assembly

After the machining of the grooves and selection of the adhesive, the fibers were glued in a two step procedure. First, the straight part of the groove was glued. After curing, the bended part of the groove was glued. For the second step of the gluing process, a purpose-built gluing stand made out of PVC was utilized, in which the disc can be placed upside down. In this arrangement, the fibers can be pulled with slight downward pressure and cure with precise fit. The gluing stand is shown schematically in Figure E.2 and can also be seen in Figure 6.5.

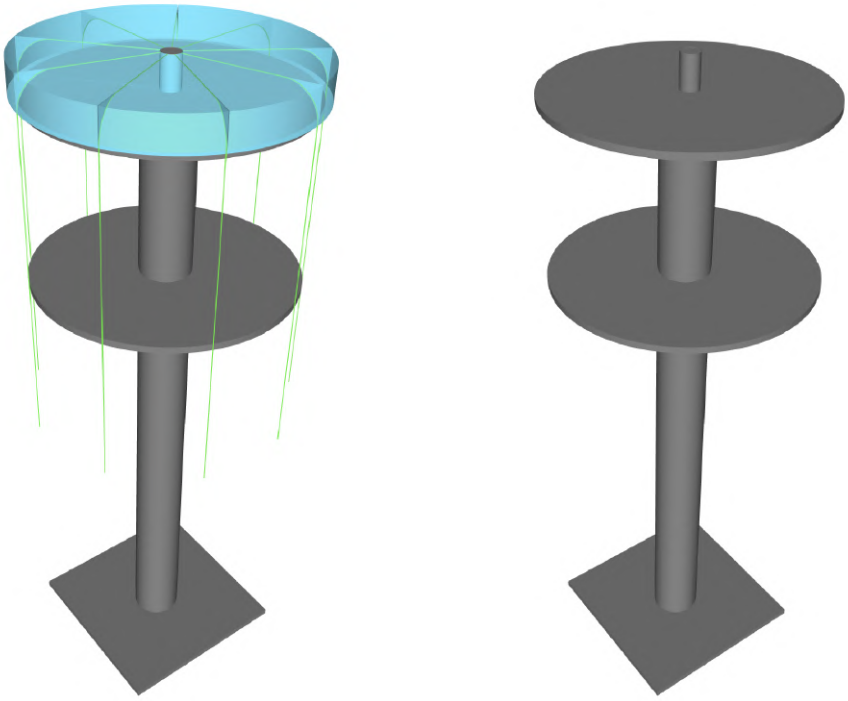

Figure E.2.: *Schematic drawing of the purpose-built gluing stand, which was used to glue the fibers into the bended part of the grooves. The disc can be placed upside down and the fibers can be pulled with slight downward pressure and cure with precise fit.*

E.4. Reflective Foil Wrapping

In Section 6.3.1, the attachment of reflective foil for the measurements with the disc at room temperature has already been addressed. The foil used is the highly reflective polyester foil Lumirror E6SR with a thickness of 188 μm fabricated by Toray [114]. This foil is specified in literature [115] with a reflection coefficient of 0.98 at a wavelength of 440 nm. Aluminum foil, on the other hand, exhibits a reflection coefficient of only 0.78 at the same wavelength. In this context, Figure E.3 shows muon spectra recorded with a small cylindrical sample of plastic scintillator with a height and a diameter of 42 mm (similar to the samples described in Section 5.2). In this measurement, the SiPM was optically coupled directly to the plastic. In the measurement corresponding to the red spectrum shown on the left, the plastic scintillator

was wrapped in aluminum foil. In the measurement corresponding to the green spectrum shown on the right, the plastic scintillator was wrapped in polyester foil. The light signal is increased by a factor of ~ 7 and the muon peak emerges more accentuated upon wrapping of the plastic scintillator with highly reflective foil. In order to maximize the light collection efficiency of the NUCLEUS *Cryogenic Muon Veto*, the use of highly reflective foil is therefore indispensable.

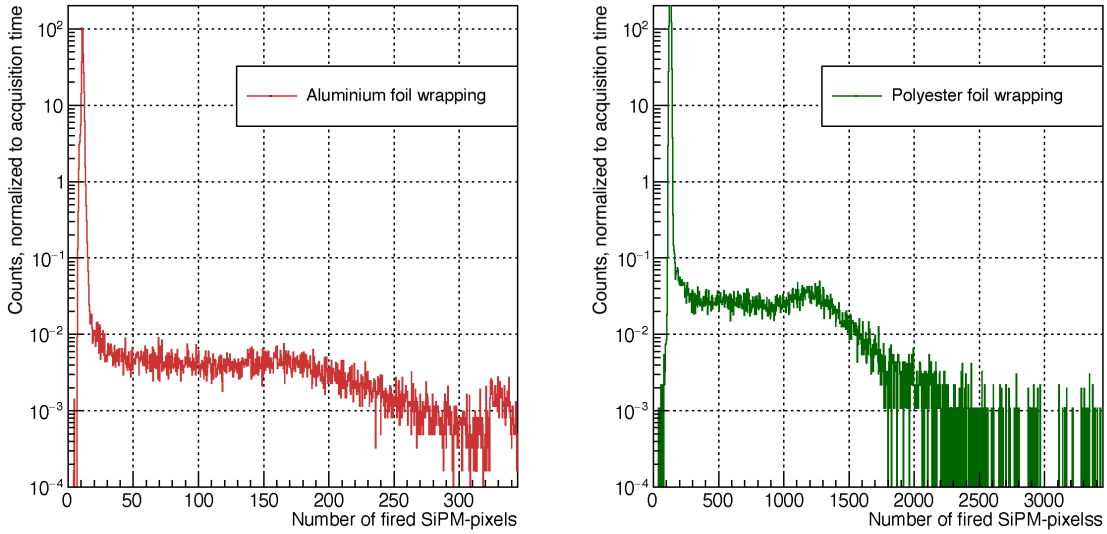

Figure E.3.: *Muon spectra recorded with a small cylindrical sample of plastic scintillator, once wrapped in aluminum foil (left) and once in polyester foil (right). The light signal is increased by a factor of ~ 7 and the muon peak emerges more accentuated upon wrapping of the plastic scintillator with highly reflective foil.*

Bibliography

[1] R. L. Mößbauer, *History of neutrino physics: Pauli's letters*, in *Proceedings of the Fourth SFB-375 Ringberg Workshop "Neutrino Astrophysics*, 3–5 (1998)

[2] F. L. Wilson, *Fermi's theory of beta decay*, American Journal of Physics **36**, 1150 (1968)

[3] H. Bethe, et al., *The neutrino*, Nature **133**, 689 (1934)

[4] C. Cowan, et al., *McGuire, and AD, Detection of the free neutrino: a confirmation*, Science **124**, 103 (1956)

[5] *Nobel Prize in Physics 1995. Awarded to Martin L. Perl and Frederick Reines.*, available at https://www.nobelprize.org/prizes/physics/1995/summary/ (2021 (19.01.2021))

[6] *Nobel Prize in Physics 2015. Awarded to Takaaki Kajita and Arthur B. McDonald.*, available at https://www.nobelprize.org/prizes/physics/2015/summary/ (2021 (19.01.2021))

[7] B. Pontekorvo, *Mesonium and antimesonium*, US Atomic Energy Commission, Technical Information Service Extension (1957)

[8] B. Pontecorvo, *Neutrino experiments and the problem of conservation of leptonic charge*, Sov. Phys. JETP **26**, 165 (1968)

[9] Q. R. Ahmad, et al., *Direct evidence for neutrino flavor transformation from neutral-current interactions in the Sudbury Neutrino Observatory*, Physical review letters **89**, 011301 (2002)

[10] R. N. Mohapatra, et al., *Neutrino mass and new physics*, Annu. Rev. Nucl. Part. Sci. **56**, 569 (2006)

[11] L. M. Krauss, *Low-energy neutrino detection and precision tests of the standard model*, Physics Letters B **269**, 407 (1991)

[12] C. Giunti, et al., *Fundamentals of neutrino physics and astrophysics*, Oxford University Press (2007)

[13] V. Kopeikin, *Flux and spectrum of reactor antineutrinos*, Physics of Atomic Nuclei **75**, 143 (2012)

[14] J. A. Formaggio, et al., *From eV to EeV: Neutrino cross sections across energy scales*, Reviews of Modern Physics **84**, 1307 (2012)

[15] F. Reines, et al., *A proposed experiment to detect the free neutrino*, Physical Review **90**, 492 (1953)

[16] P. Vogel, et al., *Neutrino oscillation studies with reactors*, Nature communications **6**, 1 (2015)

[17] D. A. Dwyer, *The neutrino mixing angle θ13: Reactor and accelerator experiments*, Physics of the Dark Universe **4**, 31 (2014)

[18] M. Apollonio, et al., *Search for neutrino oscillations on a long base-line at the CHOOZ nuclear power station*, The European Physical Journal C-Particles and Fields **27**, 331 (2003)

[19] L.-J. Wen, et al., *Reactor neutrino experiments: present and future*, Annual Review of Nuclear and Particle Science **67** (2017)

[20] M. Apollonio, et al., *Limits on neutrino oscillations from the CHOOZ experiment*, Physics Letters B **466**, 415 (1999)

[21] Y. Abe, et al., *Improved measurements of the neutrino mixing angle θ 13 with the Double Chooz detector*, Journal of High Energy Physics **2014**, 86 (2014)

[22] F. An, et al., *Observation of electron-antineutrino disappearance at Daya Bay*, Physical Review Letters **108**, 171803 (2012)

[23] K. Eguchi, et al., *First results from KamLAND: evidence for reactor antineutrino disappearance*, Physical Review Letters **90**, 021802 (2003)

[24] J. K. Ahn, et al., *Observation of reactor electron antineutrinos disappearance in the RENO experiment*, Physical Review Letters **108**, 191802 (2012)

[25] F. An, et al., *Neutrino physics with JUNO*, Journal of Physics G: Nuclear and Particle Physics **43**, 030401 (2016)

[26] M. Bowen, et al., *Reactor neutrino applications and coherent elastic neutrino nucleus scattering*, Physical Review D **102**, 053008 (2020)

[27] F. Hasert, et al., *Observation of neutrino-like interactions without muon or electron in the Gargamelle neutrino experiment*, Nuclear Physics B **73**, 1 (1974)

[28] D. Z. Freedman, *Coherent effects of a weak neutral current*, Phys. Rev. D **9**, 1389 (1974)

[29] M. Lindner, et al., *Coherent neutrino-nucleus scattering and new neutrino interactions*, Journal of High Energy Physics **2017**, 97 (2017)

[30] D. Akimov, et al., *Observation of coherent elastic neutrino-nucleus scattering*, Science **357**, 1123 (2017)

[31] A. Oralbaev, et al., *The inverse beta decay: a study of cross section*, in *Journal of Physics: Conference Series*, volume 675, 012003, IOP Publishing (2016)

[32] A. Drukier, et al., *Principles and applications of a neutral-current detector for neutrino physics and astronomy*, Physical Review D **30**, 2295 (1984)

[33] P. Vogel, et al., *Neutrino electromagnetic form factors*, Physical Review D **39**, 3378 (1989)

[34] T. Kosmas, et al., *Probing light sterile neutrino signatures at reactor and Spallation Neutron Source neutrino experiments*, Physical Review D **96**, 063013 (2017)

[35] J. Billard, et al., *Implication of neutrino backgrounds on the reach of next generation dark matter direct detection experiments*, Physical Review D **89**, 023524 (2014)

[36] K. Scholberg, *Prospects for measuring coherent neutrino-nucleus elastic scattering at a stopped-pion neutrino source*, Physical Review D **73**, 033005 (2006)

[37] D. Akimov, et al., *First Detection of Coherent Elastic Neutrino-Nucleus Scattering on Argon*, arXiv preprint arXiv:2003.10630 (2020)

[38] C. Buck, et al., *A novel experiment for coherent elastic neutrino nucleus scattering: CONUS*, in *Journal of Physics: Conference Series*, volume 1342, 012094, IOP Publishing (2020)

[39] J. Billard, et al., *Coherent neutrino scattering with low temperature bolometers at Chooz reactor complex*, Journal of Physics G: Nuclear and Particle Physics **44**, 105101 (2017)

[40] H. Bonet, et al., *Large-size sub-keV sensitive germanium detectors for the CONUS experiment*, arXiv preprint arXiv:2010.11241 (2020)

[41] S. Kerman, et al., *Coherency in neutrino-nucleus elastic scattering*, Physical Review D **93**, 113006 (2016)

[42] A. Aguilar-Arevalo, et al., *Exploring low-energy neutrino physics with the Coherent Neutrino Nucleus Interaction Experiment*, Physical Review D **100**, 092005 (2019)

[43] G. Agnolet, et al., *Background studies for the MINER coherent neutrino scattering reactor experiment*, Nuclear Instruments and Methods in Physics Research Section A: Accelerators, Spectrometers, Detectors and Associated Equipment **853**, 53 (2017)

[44] G. Angloher, et al., *Exploring CEνNS with NUCLEUS at the Chooz nuclear power plant: NUCLEUS Collaboration.*, European Physical Journal C–Particles & Fields **79** (2019)

[45] R. Strauss, et al., *The ν-cleus experiment: a gram-scale fiducial-volume cryogenic detector for the first detection of coherent neutrino-nucleus scattering*, The European Physical Journal C **77**, 506 (2017)

[46] A. Abdelhameed, et al., *First results from the CRESST-III low-mass dark matter program*, Physical Review D **100**, 102002 (2019)

[47] V. Kopeikin, et al., *Reactor as a source of antineutrinos: Thermal fission energy*, Physics of Atomic Nuclei **67**, 1892 (2004)

[48] G. Boireau, et al., *Online monitoring of the Osiris reactor with the Nucifer neutrino detector*, Physical Review D **93**, 112006 (2016)

[49] G. F. Knoll, *Radiation detection and measurement*, John Wiley & Sons (2010)

[50] A. Erb, et al., *Growth of high-purity scintillating CaWO 4 single crystals for the low-temperature direct dark matter search experiments CRESST-II and EURECA*, CrystEngComm **15**, 2301 (2013)

[51] G. Heusser, *Low-radioactivity background techniques*, Annual Review of Nuclear and Particle Science **45**, 543 (1995)

[52] H. Argo, et al., *Absorption of μ- Mesons in C 12*, Physical Review **114**, 626 (1959)

[53] *Bluefors. LD 400 ^{3}He/^{4}He Dilution Refrigerator.*, available at `https://bluefors.com` (2021 (08.03.2021))

[54] G. Ventura, et al., *The art of cryogenics: low-temperature experimental techniques*, Elsevier (2010)

[55] J. Rothe, et al., *NUCLEUS: Exploring Coherent Neutrino-Nucleus Scattering with Cryogenic Detectors*, Journal of Low Temperature Physics 1–8 (2019)

[56] M. Vivier, *Optimization Studies for the Mechanical Setup*, virtual NUCLEUS Collaboration Meeting (2021)

[57] C. Patrignani, et al., *Review of particle physics, 2016-2017*, Chin. Phys. C **40**, 100001 (2016)

[58] R. Rogly, et al., *NUCLEUS Muon Veto. Technical Note.*, Centre CEA de Saclay

[59] V. Wagner, et al., *Development of a Compact Muon Veto for the NUCLEUS experiment* (2021), article in preparation

[60] M. Chiosso, et al., *Compass-II*, Physics of Particles and Nuclei **44**, 882 (2013)

[61] P. Jörg, *The COMPASS-II Experiment*, in *Exploring the Size of the Proton*, 45–59, Springer (2018)

[62] F. Gautheron, et al., *Compass-II proposal*, Technical report (2010)

[63] A. Jabłoński, *Über den Mechanismus der Photolumineszenz von Farbstoffphosphoren*, Zeitschrift für Physik **94**, 38 (1935)

[64] D. Horrocks, *Applications of liquid scintillation counting*, Elsevier (2012)

[65] S. Moser, et al., *Principles and practice of plastic scintillator design*, Radiation Physics and Chemistry **41**, 31 (1993)

[66] W. R. Leo, *Techniques for nuclear and particle physics experiments: a how-to approach*, Springer Science & Business Media (2012)

[67] *Saint Gobain Wavelength Shifting Fibers*, available at `https://www.crystals.saint-gobain.com/products/scintillating-fiber` (2020 (29.08.2020))

[68] S. Hunklinger, *Festkörperphysik*, Oldenbourg Verlag (2009)

[69] S. M. Sze, et al., *Physics of Semiconductor Devices*, John Wiley & Sons (2006)

[70] F. Herman, *The electronic energy band structure of silicon and germanium*, Proceedings of the IRE **43**, 1703 (1955)

[71] *Ioffe Institute. New Semiconductor Materials. Characteristics and Properties*, available at `http://www.ioffe.ru/SVA/` (1998-2001)

[72] S. N. Ahmed, *Physics and engineering of radiation detection*, Academic Press (2007)

[73] *KETEK Silicon Photomultipliers*, available at `https://www.ketek.net` (2020 (05.10.2020))

[74] *SensL. An Introduction to the Silicon Photomultiplier.*, available at `https://www.sensl.com/downloads/ds/TN%20-%20Intro%20to%20SPM%20Tech.pdf` (2020 (07.12.2020))

[75] *Hamamatsu. How does temperature affect the performance of an SiPM?*, available at `https://hub.hamamatsu.com/us/en/technical-note/sipm-temperature-performance/index.html` (2020 (07.12.2020))

[76] *ROOT. Data Analysis Framework.*, available at https://root.cern.ch (2021 (21.01.2021))

[77] *TGeometry Package.*, available at https://root.cern.ch/root/html534/guides/users-guide/Geometry.html (2021 (21.01.2021))

[78] S. Haino, et al., *Measurements of primary and atmospheric cosmic-ray spectra with the BESS-TeV spectrometer*, Physics Letters B **594**, 35 (2004)

[79] P. Shukla, et al., *Energy and angular distributions of atmospheric muons at the Earth*, International Journal of Modern Physics A **33**, 1850175 (2018)

[80] C. Patrignani, et al., *Review of particle physics, 2016-2017*, Chin. Phys. C **40**, 100001 (2016)

[81] *Particle Data Group. Atomic and Nuclear Properties.*, available at https://pdg.lbl.gov/2016/AtomicNuclearProperties/ (2021 (12.03.2021))

[82] *Engineering ToolBox. Densities of Materials.*, available at https://www.engineeringtoolbox.com/density-materials-d_1652.html (2021 (12.03.2021))

[83] L. Peralta, *Temperature dependence of plastic scintillators*, Nuclear Instruments and Methods in Physics Research Section A: Accelerators, Spectrometers, Detectors and Associated Equipment **883**, 20 (2018)

[84] *Saint Gobain. Plastic Scintillator BC-4xx.*, available at https://www.crystals.saint-gobain.com/products/ (2020 (13.10.2020))

[85] A. Sörensen, et al., *Temperature quenching in LAB based liquid scintillator*, The European Physical Journal C **78**, 1 (2018)

[86] H. Seliger, et al., *Temperature effects in gas-free liquid scintillators*, IRE Transactions on Nuclear Science **3**, 62 (1956)

[87] X. Dong-Mei, et al., *Temperature dependence of the light yield of the LAB-based and mesitylene-based liquid scintillators*, Chinese Physics C **38**, 116001 (2014)

[88] Y. Homma, et al., *Some effects of temperature on fluorescence for pure toluene and liquid scintillator*, Journal of radioanalytical and nuclear chemistry **95**, 281 (1985)

[89] W. Reese, *Low-Temperature Thermal Conductivity of Amorphous Polymers: Polystyrene and Polymethylmethacrylate*, Journal of Applied Physics **37**, 864 (1966)

[90] P. Klemens, *Theory of the thermal conductivity of amorphous solids*, in *Thermal Conductivity 18*, 307–314, Springer (1985)

[91] C. Huang, et al., *Thermal conductivity of polymers and polymer nanocomposites*, Materials Science and Engineering: R: Reports **132**, 1 (2018)

[92] T. L. Bergman, et al., *Fundamentals of heat and mass transfer*, John Wiley & Sons (2011)

[93] *Engineering ToolBox. Coefficients of Emissivity.*, available at https://www.engineeringtoolbox.com/emissivity-coefficients-d_447.html (2020 (26.11.2020))

[94] *Eljen Technilogy. Plastic Scintillator EJ-204.*, available at https://eljentechnology.com/products/plastic-scintillators (2020 (13.10.2020))

[95] *Institute for Scintillation Materials of NAS. Plastic Scintillator UPS 923-A.*, available at http://isma.kharkov.ua/en (2020 (10.11.2020))

[96] K. Freund, et al., *The performance of the Muon Veto of the GERDA experiment*, The European Physical Journal C **76**, 298 (2016)

[97] *Saint Gobain. Wavelength-Shifting Fibers BCF-91A.*, available at https://www.crystals.saint-gobain.com/products/scintillating-fiber (2020 (29.12.2020))

[98] J. J. Csáthy, et al., *Optical fiber read-out for liquid argon scintillation light*, arXiv preprint arXiv:1606.04254 (2016)

[99] P. Krause, *The New Liquid Argon Veto of GERDA*, Master thesis, Technical University of Munich (2019)

[100] D. McKinsey, et al., *Detecting ionizing radiation in liquid helium using wavelength shifting light collection*, Nuclear Instruments and Methods in Physics Research Section A: Accelerators, Spectrometers, Detectors and Associated Equipment **516**, 475 (2004)

[101] *Kuraray. Wavelength-Shifting Fibers Y-11.*, available at https://www.kuraray.com/products/psf (2020 (29.12.2020))

[102] *Henkel Loctite. Low Viscosity Adhesive Product 406.*, available at https://datasheet.octopart.com/406-Loctite-datasheet-509952.pdf (2021 (05.01.2021))

[103] L. Manzanillas, *STEREO: Search for sterile neutrinos at the ILL*, arXiv preprint arXiv:1702.02498 (2017)

[104] *Rohde & Schwarz. RTO2004 Oscilloscope*, available at https://www.rohde-schwarz.com/de/produkt/rto-produkt-startseite_63493-10790.html (2021 (15.03.2021))

[105] E. Engelmann, *Extensive Studies of Afterpulsing of Silicon Photomultipliers Down to Liquid Argon Temperatures*, Master thesis, Technical University of Munich (2014)

[106] R. Cerulli, *Cold Passive Shield Overview*, virtual NUCLEUS Collaboration Meeting (2021)

[107] *Saint Gobain. Optical Cement BC-600.*, available at https://www.impexron.de/show_catalogue_pdf/161503/1 (2021 (04.04.2021))

[108] *Struck. SIS 3316 FADC*, available at https://www.struck.de/sis3316-2014-03-20.pdf (2021 (03.04.2021))

[109] R. Burkhardt, *Abschätzung der Abschirmwirkung des Garchinger Untergrundlabors (UGL) durch die Messung des Myonen-Flusses inner- und außerhalb des UGLs*, Bachelor thesis, Technical University of Munich (2012)

[110] L. D. Landau, *On the energy loss of fast particles by ionization*, J. Phys. **8**, 201 (1944)

[111] V. Wagner, *Blank Assembly*, virtual NUCLEUS Collaboration Meeting (2021)

[112] *Engineering ToolBox. Coefficients of Linear Thermal Expansion.*, available at https:

//www.engineeringtoolbox.com/linear-expansion-coefficients-d_95.html (2020 (13.11.2020))

[113] J. J. Csáthy, et al., *Development of an anti-Compton veto for HPGe detectors operated in liquid argon using silicon photo-multipliers*, Nuclear Instruments and Methods in Physics Research Section A: Accelerators, Spectrometers, Detectors and Associated Equipment **654**, 225 (2011)

[114] *Toray. Lumirror E6SR*, available at https://www.toray.com/products/films/fil_0010.html (2021 (12.04.2021))

[115] M. Janecek, *Reflectivity spectra for commonly used reflectors*, IEEE Transactions on Nuclear Science **59**, 490 (2012)


nucleus
EXPERIMENT